Development of a Gamma Ray Telescope for Online Synovial Dosimetry In Boron Neutron Capture Synovectomy

by

Hongyu Jiang

M.E. Engineering Physics (1999)
Tsinghua University

B.S. Engineering Physics (1994)
Tsinghua University

Submitted to the Department of Nuclear Engineering
in Partial Fulfillment of the Requirements for the Degree of
Doctor of Philosophy in Nuclear Engineering

At the

Massachusetts Institute of Technology

June 2003

Signature of Author……...

Department of Nuclear Engineering
May 25,2003

Certified by……...
Jacquelyn C. Yanch
Professor of Nuclear Engineering and
Whitaker College of Health Sciences and Technology
Thesis Supervisor

Read by…….
Ruth E. Shefer
President, Newton Scientific, Inc.
Thesis Reader

Accepted by……...
Jeffrey A. Coderre
Chairman, Department Committee on Graduate Students

Development of a Gamma Ray Telescope for Online Synovial Dosimetry

In Boron Neutron Capture Synovectomy

by

Hongyu Jiang

Submitted to the Department of Nuclear Engineering
In May, 2003 in Partial Fulfillment of the
Requirements for the Degree of Doctor of Philosophy in
Nuclear Engineering

Abstract

Boron Neutron Capture Synovectomy (BNCS) is a novel application of the $^{10}B(n,\alpha)$ reaction for potential treatment of rheumatoid arthritis. During BNCS clinical trials, real-time knowledge of boron dose delivered to the synovium is necessary so that the remaining irradiation time can be determined. A 478 keV photon is emitted following 94% of boron neutron capture reactions, and detection of 478 keV photons emitted from the synovium provides a potential approach for online monitoring of the accumulated synovial boron dose. This thesis explores the feasibility of developing a telescope system for online determination of synovial boron dose for accelerator-based BNCS. The Monte Carlo code MCNP was used to design the telescope system. The neutron and photon background distributions in the radiation vault at the Laboratory for Accelerator Beam Applications (LABA) at MIT were explored via Monte Carlo simulations, and an optimum position for the photon detector was determined. Collimator and detector shields were designed, and significant reduction of neutron flux and background count at the detector location was observed. Sufficient boron photon counts from the synovium were predicted, and the feasibility of using a NaI detector instead of an HPGe detector was also confirmed. Next, a telescope system was built in the radiation vault at LABA. A background peak overlapping the energy region of 478 keV photons was observed in the measured spectrum by a 10.2 cm × 10.2 cm NaI(Tl) detector. Origin and direction of background particles entering the detector were explored, and further background reduction was achieved. The composition of the background peak was also analyzed. Experimental characterization of the telescope system was performed. It was confirmed that boron photons from the synovium could be detected in the presence of background counts. The count saturation became significant when the boron concentration was over 10,000 ppm, as predicted by simulations. Experimental results were compared with simulation results, and the overall agreement was within 10–20%. Reconstruction approaches for determination of the synovial boron dose based on the measured boron photon count and additional information such as anatomic configuration of the joint and boron compound distribution were generated.

Thesis Supervisor: Jacquelyn C. Yanch
Title: Professor of Nuclear Engineering and Whitaker College of Health Sciences and Technology

Acknowledgements

I would like to thank Prof. Yanch for her direction, support, and patience. I had a very pleasant time working with her. Four years ago, I came to this country from a remote land, with very little preparation for a new life. I was so lucky to be under the supervision of Prof. Yanch. Thanks to her, I had always felt comfortable and confident in my work and life. I learned too much from her, and I remembered everything she did to help me improve my English. My appreciation to her cannot be simply described in words.

I give my thanks to Ruth and Bob for answering my questions and solving my problems about the accelerator. I could not have finished my experiments without their help. A special thank to Ruth for her kindness to serve as the thesis reader.

I would also like to thank Dr. Lanza for being on my Ph.D. committee, and for giving me cool ideas on my thesis. He is such a kind and knowledgeable person. It was always fun to talk with him.

Thanks to Prof. Coderre. It was wonderful experience to work with him on the course 22.09/22.104.

I give my thanks to Rong for spending so much time in helping me finish my experiments during weekends and for her special contribution to my thesis. I owe her too much.

I'd like to thank Rong, Ray, and Michael for being my operator. I would also like to extend my thanks to former members of LABA, David, Joanne, Brandon, and Susan for helping me and teaching me how to operate the accelerator. A special thank is given to Xuping. It had been always pleasant and valuable to have discussions with her.

I would like to thank Dusadee, although she was not a "formal" member of LABA. I was so lucky to have a chance to know a person with such a great personality.

My parents deserve special thanks. They had never posed any pressure on me, and they had been always ready to try their best to help me. Thanks to them, I could do what I wanted. I also owe too much to them.

Lastly, I give my thanks to Rachel for all her kindness and help. She made my life much easier.

Table of Contents

List of Figures

List of Tables

Chapter 1 Introduction

Boron Neutron Capture Synovectomy (BNCS), now under investigation at MIT's Laboratory for Accelerator Beam Applications (LABA), is potentially a novel modality for treating rheumatoid arthritis. Rheumatoid arthritis is a systemic disease characterized by inflammation of the synovium. It can be treated with drugs and by surgical removal of the synovial membrane (surgical synovectomy). Radiation synovectomy by intra-articular injection of beta-emitting nuclides has been extensively used in other countries, but it has not been approved in the United States because of concerns regarding leakage of the nuclide from the joint. Similar to BNCT (Boron Neutron Capture Therapy), BNCS includes two consecutive steps. First, a stable ^{10}B labeled compound is injected into the synovial fluid. Next, after the compound has sufficiently accumulated in the inflamed synovium, the joint is irradiated with a low-energy neutron beam. As the energy of the heavy charged particles emitted after ^{10}B neutron capture is deposited locally to regions loaded with boron, the synovium is ablated and the symptoms of rheumatoid arthritis are thereby relieved.

During BNCS clinical trials, real-time knowledge about the boron dose delivered to the synovium is necessary so that the remaining irradiation time can be determined. However, online determination of the synovial boron dose is a very difficult problem. An approach for prompt measurement of the boron concentration in brain tumors has been proposed in Petten, the Netherlands, which adopted a scheme of photon detection with a telescope configuration. The goal of this thesis work is to design and build a gamma ray telescope system for online estimation of the synovial boron dose in BNCS. Compared to the system in Petten, new designs are required at LABA because of the differences between BNCT and BNCS.

Chapter 2 gives the overall background introduction to BNCS and the basic principles of online boron dose determination. A telescope system, which has already been set up and tested in Petten, the Netherlands, will be described, and differences in the overall approach when used for BNCS will be discussed.

Chapter 3 focuses on the investigation of background radiation in the therapy room. Monte Carlo simulations have been performed to explore the spatial distribution of neutrons and photons during joint irradiation. The purpose is to find the approximate position for the photon detector, the central component of the telescope system. Ideally, the detector will be positioned at a location with the lowest neutron and photon backgrounds to reduce the requirements for detector shielding.

Chapter 4 describes the simulations conducted to study the feasibility of the telescope system for BNCS. The collimator and detector shield are added to the system. The performance of the telescope system under various conditions is compared. The possibility of using a NaI (sodium iodine) detector

instead of an HPGe (high purity germanium) detector is discussed. The optimal position of the photon detector is chosen, based on the quantitative analysis of several figures of merit.

Chapter 5 depicts the details of assembling a real telescope system in the BNCS radiation vault at MIT LABA. An introduction to the experimental system is given. Special issues such as synovium phantom preparation and system alignment are covered. The detected photon spectrum by a NaI detector is displayed. Special attention is paid to the background analysis to further reduce the background count rate. The performance of the system after various improvements is presented and discussed.

Chapter 6 gives a more thorough exploration of the background boron peak. The purpose of this chapter is to search for the approximate composition of the background peak. The separate count contributions from several potential sources are roughly determined with the help of experiments and Monte Carlo simulations.

Chapter 7 introduces the experiments performed to characterize the system. Whether or not the boron photons from the synovium can be detected in the presence of background counts is confirmed. Results from simulations and experiments are compared to verify whether the Monte Carlo method is a predictive tool in developing the telescope system. The self-shielding effect is emphasized through the comparison of four different configurations of the synovium phantom.

Chapter 8 probes the reconstruction approaches to determine the synovial boron dose, based on the measured boron photon count and additional information.

Chapter 9 summarizes the development of this telescope system, and gives recommendations for future work.

Chapter 2 Background

2.1 Boron Neutron Capture Synovectomy (BNCS)

Rheumatoid arthritis is a systemic disease characterized by inflammation of the synovium, the membrane lining the inner joint capsule of articulating joints[1,2]. The cause of this disease is still unclear. In normal joints, the synovium is very thin (the thickness of several cells). However, in joints with rheumatoid arthritis, after proliferation of the synovial cells, the synovium increases in thickness to several millimeters, and the amount of synovial fluid in the joint cavity increases as well.

Rheumatoid arthritis is treated with anti-inflammatory drugs, and, when these drugs fail, surgical removal of the synovial membrane is performed. Radiation synovectomy is an alternative to surgery. In other countries, radiation treatment with beta radioisotopes has been widely adopted. During treatment, a beta-emitting radioisotope is injected into the synovial fluid, and the kinetic energy carried by the beta particles is deposited in the synovium, killing the cells. However, in the United States, the technique has not been approved for routine clinical use because of the worry about the potential risk of isotope leakage from the joint[3].

At MIT LABA, a potential novel modality for arthritis treatment with radiation is under investigation[4-6]. Instead of injecting radioisotopes, a ^{10}B-containing, non-radioactive compound is injected into the synovial fluid. After sufficient boron has accumulated in the synovium, the joint is irradiated with a low-energy neutron beam. Boron neutron capture reactions ($^{10}B(n,\alpha)^{7}Li$) will occur in the boron-loaded synovium. If enough reactions occur, the kinetic energy released with the two heavy charged particles (α and ^{7}Li) will kill the synovial cells.

A schematic of the LABA accelerator[7] and radiation vault at LABA used in the development of several aspects of BNCS is presented in Figure 2.1. The BNCS neutron beam[8] is generated with a tandem accelerator. The BNCS beam tube, a beryllium target and the associated neutron moderator and reflector are located inside the radiation vault. Many nuclear reactions can be used for neutron beam production in BNCS. The nuclear reaction used in this thesis is $^{9}Be(d,n)$, and the kinetic energy of incident deuterons is 1.5 MeV. More details about the neutron beam will be introduced in the next chapter.

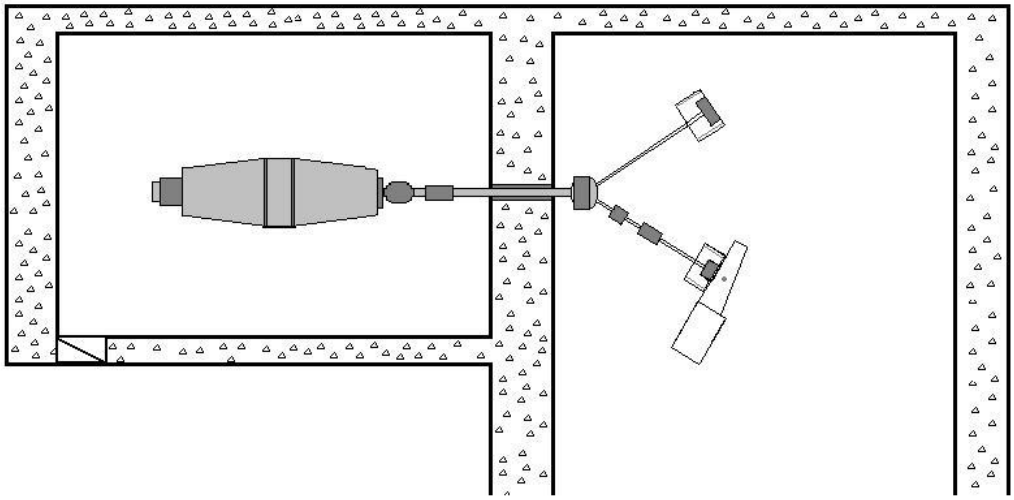

Figure 2.1 Schematic of the LABA accelerator and the radiation vault.

2.2 Boron dose determination

An issue in BNCS is the determination of the synovial boron dose. Because of the similarities between BNCT[9,10] and BNCS, it could be helpful to recall the procedures in BNCT. In BNCT, before neutron irradiation, patients are given a boron-containing compound. The compound enters into the blood, and is conveyed to the target tissue. An assumption of equal boron concentrations in blood and in healthy brain tissue is made, so the boron concentration in the brain tissue is available through analysis of blood samples before, during, and after the treatment. The boron dose can then be deduced from information regarding boron concentration. On the other hand, in BNCS, the boron compound is injected directly into the synovial fluid[4], and hence the assay of blood samples is not useful in determining the boron concentration in the synovium or in determining the synovial dose. Thus, it is crucial to develop a new approach to determine the synovial dose during irradiation. In particular, an online approach for monitoring the synovial boron dose or dose rate in the synovium during the clinical treatment will be greatly desirable, since it allows more accurate dose delivery.

A method proposed for online boron concentration determination is based on the detection of the 478 keV photons emitted following neutron absorption in ^{10}B[11-13]. The expression of boron neutron capture is

$$n + {}^{10}B \rightarrow \alpha + {}^{7}Li^{*} \qquad Q = 2.310 \text{ MeV} \quad \text{(branching ratio: 94\%)}$$

$${}^{7}Li^{*} \rightarrow {}^{7}Li + \gamma \text{ (478keV)}$$

$$\rightarrow \alpha + {}^{7}Li \qquad Q = 2.792 \text{ MeV} \quad \text{(branching ratio: 7\%).}$$

Ninety-four percent of the produced ^{7}Li nuclei are at their first excited state, and a 478 keV photon is released as the $^{7}Li^{*}$ nucleus decays to its ground state. Because of the Doppler effect (the half-life of the first exited state of $^{7}Li^{*}$ is so short that the photon is emitted before the nucleus stops in the medium), the energy of the emitted photons ranges through an interval of 15 keV (470 to 485 keV). Throughout this dissertation, this "478 keV photon" is sometimes referred to as the "boron photon", but actually, it is released from lithium nuclei.

For boron dose determination, what is actually required is knowledge regarding the number of boron neutron captures, not the boron concentration. The average kinetic energy deposited in each $^{10}B(n,\alpha)^{7}Li$ reaction is 94%×2.310 MeV+6%×2.792 MeV = 2.339 MeV. Therefore, if the number of boron neutron captures is provided, the total energy deposited via α and ^{7}Li nuclei is known. Then, the absorbed boron dose is obtained by dividing the energy by the mass of the boron-loaded target tissue. Detection of the 478keV photons offers a possible way for online measurement of the number of $^{10}B(n,\alpha)^{7}Li$ reactions. By knowing the fraction of emitted boron photons actually detected, an estimate of synovial boron dose becomes possible.

A brief overview of the procedure for synovial boron dose determination is as follows: after the patient is in position, and ^{10}B injection and post-administration accumulation in the synovium are accomplished, the joint with rheumatoid arthritis is irradiated with a neutron beam produced via an accelerator reaction; neutrons are captured in the boron in the synovium, and 478 keV boron photons are emitted isotropically. A very small fraction of the boron photons from the synovium will arrive at the detector and ultimately be detected; with the aid of additional information such as solid angle of the detector to the synovium, photon attenuation in the joint, and full detection efficiency of the detector, the number of $^{10}B(n,\alpha)$ reactions occurred in the synovium will be determined using appropriate reconstruction algorithms and then the absorbed boron dose will be determined.

2.2.1 Telescope system at Petten

A technique based on a telescope configuration for boron concentration determination in BNCT has been designed and installed at the High Flux Reactor (HFR) in Petten, the Netherlands. The primary components of this telescope system are shown in Figure 2.2[11]. The telescope system includes a high purity germanium (HPGe) photon detector, a collimator, and a detector shield. The photon detector is located relatively far away from the head phantom (> 200 cm; this is the origin of the name "telescope") to avoid interfering with the therapy process and to avoid the intensive background radiation around the target tissue. The function of the collimator, which is made of tungsten and lead, is critical. The viewing region of the photon detector is confined to a narrow spatial region in the phantom by the hole in the

collimator to achieve a better spatial resolution and to reduce the background photon count. The photon detector is positioned above the ceiling of the therapy room. The ceiling, which serves as a suitable detector shield for both neutrons and photons, is composed of a layer of boron-loaded polyethylene and a layer of lead and steel. Since the detector is outside the therapy room, there is no need for additional detector shielding. The photon spectrum detected with the HPGe detector is also shown in Figure 2.2. The broadened boron peak is clearly visible, and on the right of it, a sharp 511 keV annihilation peak is apparent as well. To distinguish the boron peak from the annihilation peak, an HPGe semiconductor detector was selected since the energy resolution of scintillation detectors is generally not sufficient.

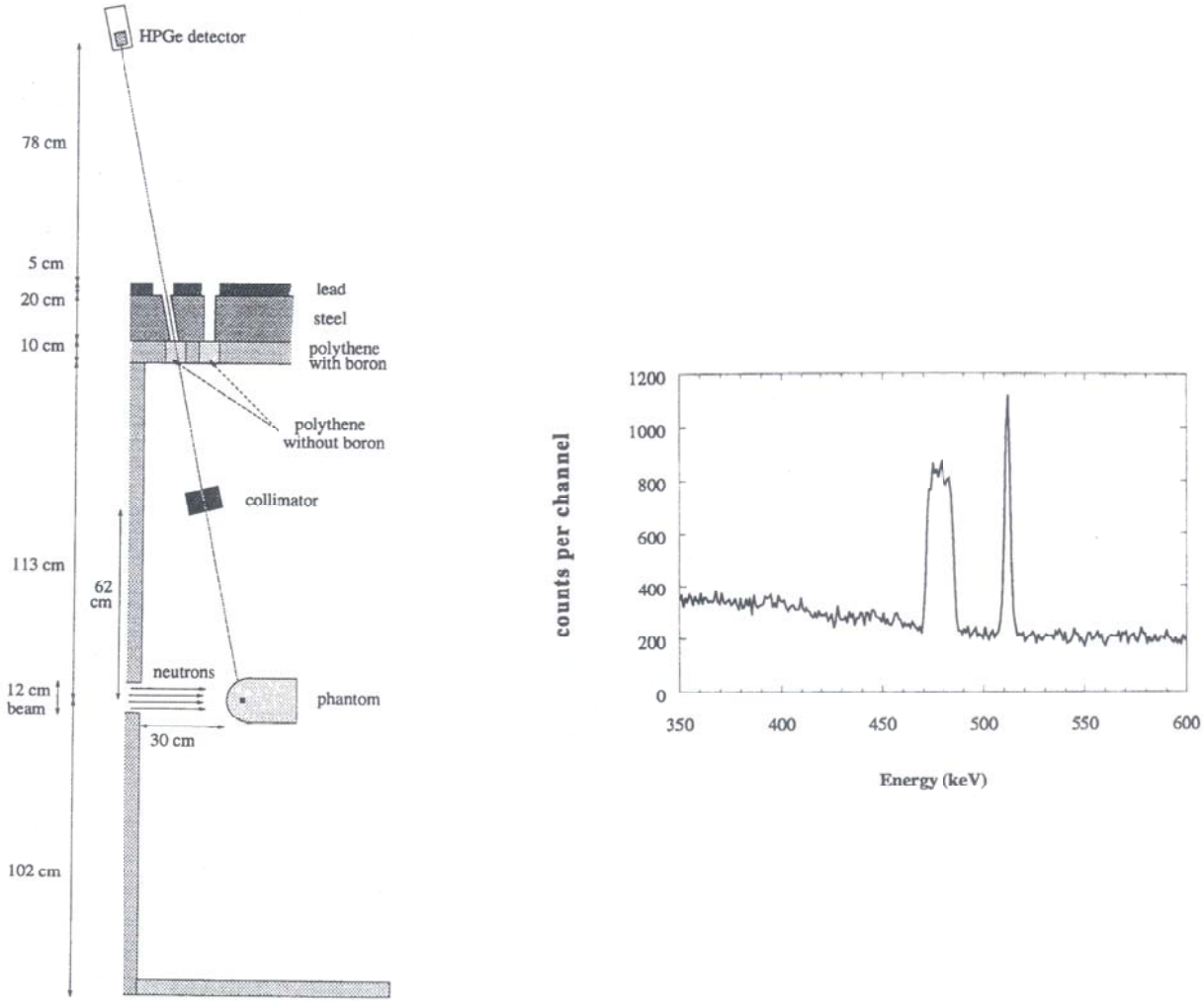

(a) (b)

Figure 2.2 (a) Schematic of the telescope system at HFR in Petten, which includes an HPGe detector, a collimator and the ceiling serving as the detector shield; (b) the detected photon spectrum by the HPGe detector.

2.2.2 Differences between BNCS and BNCT

Our ultimate goal is to design and implement a telescope system for online monitoring of the synovial boron dose during BNCS treatments. While the system at Petten provides an excellent starting point, there are several differences between BNCT and BNCS; these differences make redesign of a telescope system specifically useful for BNCS necessary.

First of all, the tumor ^{10}B uptake in BNCT is usually at the level of several to several tens of ppm (parts per million), whereas the synovial boron concentration in BNCS is expected to be several thousands of ppm[6]. Potentially, many more boron photons will be emitted from the synovium in BNCS, and the count rate of boron photons will be much higher than that at Petten. The advantages of a higher count rate include a better signal to noise ratio and a shorter detection time to achieve a statistically reliable count. In addition, the use of NaI(Tl) detectors[14] may become possible.

In BNCT, a very clean epithermal neutron beam is necessary. The boron concentration is low, and so is the boron dose rate. If the neutron beam is contaminated with fast neutrons, the healthy tissue dose from fast neutrons can be significant. However, in BNCS a neutron beam mixed with fast neutrons is acceptable[6]. The boron concentration is high, and the irradiation time is expected to be short. Therefore, the healthy tissue dose from fast neutrons and incident photons is small. (Quantitative results will be provided in the next chapter).

The third difference comes from the depth and the shape of the target tissue. The depth of synovium is about 0.4 to 1.3 cm from the skin, in contrast with up to 7 to 10 cm for a deep-seated brain tumor. The size of joints (such as the knee or finger) may be quite variable, so the gamma ray telescope for BNCS has to be adaptable to joints of a wide range of sizes.

2.2.3 Potential differences between the telescopes at Petten and at LABA

The first difference from the system at Petten is that the telescope at LABA will be initially located inside the therapy room. The ceiling and surrounding walls of the radiation vault at LABA are made of ordinary concrete, and other than their thickness (3 - 4 feet), they are not specially designed for neutron and photon shielding. In addition, the shortest distance from the synovium to a detector position outside the vault is over 300 cm. Since the boron photon count rate decreases rapidly as the distance from the synovium increases, such a long distance may cause insufficient boron photon count rate. On the other hand, the possibility of locating the detector outside the room will also be explored. The feasibility of using concrete as the neutron and photon shielding material will be studied in simulations.

The second difference is the possibility of using a NaI detector at LABA. To completely separate the 478 keV peak and the 511 keV peak, the energy resolution of a photon detector has to be lower than 4%

(here the width of a photon peak is represented with the FWTM: full width at tenth-maximum), which is impractical for a NaI detector. However, for the telescope at LABA, the boron photon count rate is expected to be much higher than that of 511 keV photons, and so distinguishing the 511 keV peak from the 478 keV peak may not be necessary. Thus, use of a NaI detector instead of an HPGe one may now be possible. A good feature of NaI detectors is their relative insensitivity to radiation damage caused by fast neutrons[14]. This could be a big advantage if the detector is located somewhere with a strong fast neutron background, such as in the radiation room at MIT LABA.

Another difference comes at the stage of dose reconstruction, where the required synovial boron dose is deduced from the count of boron photons. Boron concentration in brain tumors was the goal using the Petten telescope[13]; however, the synovial boron dose is the goal with the telescope to be developed at LABA. Boron concentration is a quantity independent of neutron irradiation. At Petten, when reconstructing the boron concentration, the ratio of boron photon counts to hydrogen photon counts (B/H), which is independent of neutron flux, was selected[13]. On the other hand, boron dose is proportional to the neutron flux. Therefore, B, the number of detected boron photons, is a better choice than B/H in determining the synovial boron dose. Consequently, the reconstruction approaches could be very different for the two systems.

Although the development of a telescope for BNCS was conducted based on a particular neutron production reaction (^{9}Be(d,n) at a deuteron energy of 1.5 MeV) and a particular therapy room (the radiation vault at LABA), the goal of this thesis was toward developing a general telescope system that is also applicable to other neutron production reactions and other physical configurations of the therapy room. More details will be provided in Chapter 7.

Chapter 3 Background Investigation Using Monte Carlo simulations

This chapter and the next will describe the development of a telescope system for BNCS designed using the Monte Carlo method[15,16]. In this chapter, the major problems involved in developing the system will be discussed first. Next, the BNCS model in Monte Carlo simulations will be introduced in detail. The eventual fate of the source neutrons will be explored, and the spatial distribution of neutrons and photons in the radiation vault will be studied. At the end of this chapter, the approximate position of the photon detector will be determined; the precise position will be determined in Chapter 4.

3.1 Primary problems to be solved in simulations

3.1.1 Location of the detector

First, it is important to determine a suitable location for the photon detector. The candidates include the positions inside the therapy room and those outside it. The apparent advantage of locating the detector outside the therapy room is that there is no need to build the detector shield, but this choice is more likely to be restricted by the practical situation such as space availability and the influence of the particle flux created by construction material of the ceiling/walls.

Several figures of merit will be applied to quantitatively evaluate the advantages and disadvantages of each location. The first figure of merit is neutron flux. Neutrons, primarily fast neutrons, can cause radiation damage in the effective volume of a photon detector. One of the direct consequences of this is the degradation of the energy resolution of the detector[14]. Prompt and delayed photons are induced as a result of neutron interactions with the nuclei in the detector and the surrounding materials. The detection probability of these photons is relatively high. Thus, a weaker neutron field around the detector promises not only less detector damage but also a higher signal to noise ratio (SNR). The second important figure of merit is the count rate of the detected 478 keV boron photons, B, from the synovium. A location at which the detector can collect more boron photons from the synovium is a better choice. The next significant figures of merit are ratios: the ratio of boron photon counts to hydrogen photon counts (B/H) and the ratio of boron photon counts to neutrons (B/N). These two figures of merit take into consideration the potential background contributions from 2223 keV hydrogen photons and neutrons, respectively.

3.1.2 Feasibility of the telescope system

The feasibility of the telescope system for BNCS is determined by addressing the following three aspects. First, the detector damage caused by fast neutrons must be endurable. This is especially crucial if an HPGe detector is chosen. (The threshold for damage to HPGe detectors is ~10^9 fast neutrons/cm^2)[14,17]. Second, the boron photon count from the synovium must be detected well above the background. This

detection process requires the discerning of weak signals superimposed on significant background/noise contributions. With the help of appropriately designed collimators and detector shields, the signal to noise ratio can be greatly improved. However, it is impossible to eliminate all the background counts: there will always be neutrons and background photons entering the detector via the aperture in the collimator; this aperture is designed to allow the boron photons from the synovium to enter detector. Third, the count rate of boron photons originating from the synovium should be high enough so that the collection time required to reduce the statistical error to an acceptable level is practical.

3.1.3 Parameters of the telescope system

The telescope system under development consists of a photon detector, a collimator, and a detector shield. Several parameters need to be selected: the location of the detector, the position of the collimators, the materials used for shielding and their respective thicknesses, and the size of the aperture in the collimator. Optimizations will be involved in this process.

3.1.4 Selection of the detector

NaI and HPGe detectors are the most widely used photon detectors[14]. NaI detectors have the advantages of high detection efficiency, easy handling, and low cost. The major disadvantage is that their energy resolution is relatively poor. HPGe detectors, by contrast, have the advantage of good energy resolution; however, they are expensive and sensitive to radiation damage. Figure 3.1 gives the appearance of the boron peak (470 – 485 keV) and the 511 keV peak for the two types of detectors, simulated with *Matlab*. The two peaks are well separated in the spectrum by HPGe detectors, and the shapes of the peaks are consistent with those measured, as illustrated in Figure 2.2. On the other hand, the two peaks in the spectrum overlap when NaI detectors are used.

At Petten, the 511 keV annihilation peak is the primary source of background affecting the detection of boron photons emitted from the target tissue. To fully distinguish the 478 keV peak from the 511 keV annihilation peak, the energy resolution of the photon detector has to be less than 4%, which is not possible for standard NaI detectors to achieve. Therefore, an HPGe detector has to be used for accurate boron photon count measurement. However, in BNCS, the boron concentration in the synovium is several hundred to several thousand times higher than that in BNCT, and photon emission from the joint is expected to be correspondingly significantly higher. The use of a NaI detector will be possible if the count rate of 511 keV annihilation photons is significantly less than that of boron photons. It will be especially plausible if the annihilation photon count does not vary significantly under various synovial boron concentrations, so that the 511 keV photon contribution to the boron peak could be assumed to be stable and constant.

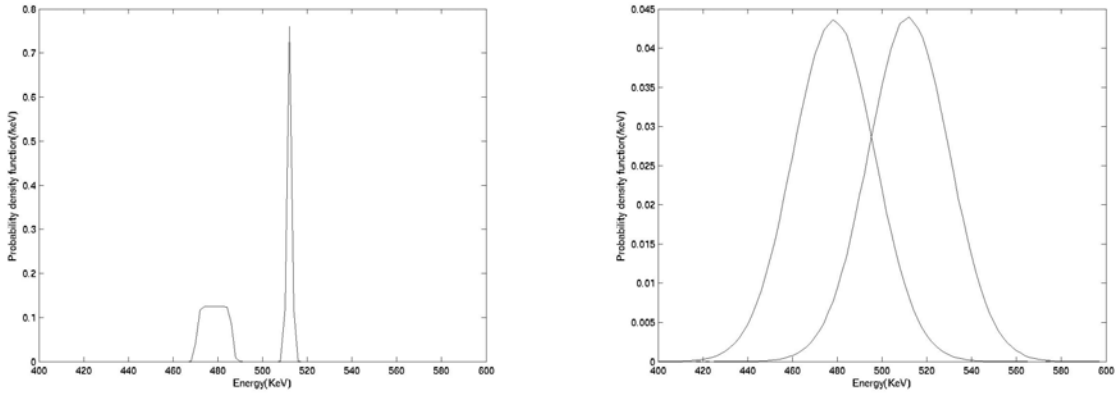

Figure 3.1 Simulated boron photon peak and 511 keV photon peak with *Matlab* for (a) a HPGe detector with a FWHM of 2 keV at 478 keV and (b) a NaI detector with a FWHM of 42 keV at 478 keV.

3.2 Special issues in conducting Monte Carlo simulations

The Monte Carlo code MCNP (version 4B)[18], which was developed at the Los Alamos National Laboratory, was used for design of the telescope system. Many features in this code such as flexible geometrical specification, ability in dealing with physical processes in very detailed manners, rich collection of variance reduction methods and extensive cross section data, make it versatile in solving problems associated with neutron, photon, electron, or coupled neutron/photon/electron transport.

Developing the telescope system using Monte Carlo simulations is hampered by low computational efficiency. To track neutrons and photons precisely, the beam tube, the anthropomorphic phantom, the telescope system, and the concrete surroundings of the radiation vault have to be included in the simulation model. The spatial volume of this simulation model is over one hundred cubic meters. However, the effective volume of a photon detector is much smaller, and therefore the count probability in the detector tally will be very low. It has been estimated in preliminary simulations that the count probability could be as low as 10^{-6} per source neutron for neutron tallies and 10^{-9} per source neutron for boron photon tallies. Neutron transport is very time consuming, and pure analog Monte Carlo simulations are not practical for solving the problems with such low count efficiencies using personal computers (PCs). Some effective variance reduction methods have to be applied. In MCNP neutron transport, implicit capture is used by default[18]. This method is helpful in most neutron transport problems; however, it is not powerful enough for solving problems with thick penetration involved. The best candidates of variance reduction methods available in MCNP include the point detector method (F5 tally) and the DXTRAN method[18]. These methods are both very powerful in dramatically improving the count

efficiency. More details of these methods and the effectiveness and deficiencies of these methods in developing the telescope system will be discussed in the next chapter (section 4.4).

In Monte Carlo simulations in this chapter and the next chapter, the variance reduction methods described above will be extensively used. In this chapter, the uncertainty of the simulation results regarding boron neutron capture and boron dose in the synovium is less than 1%. For neutron and photon fluxes, the uncertainty is less than 2%. In the next chapter, after the collimator and detector shield are added, the simulated counting efficiency will be significantly reduced. The number of particles generated such that the corresponding uncertainty in neutron and photon flux and fluence was always less than 5% except for that for 511 keV photons, which is around 10% under some situations.

3.3 BNCS model for simulations

The BNCS model for MCNP simulations, which is a part of the simulation model used in the development of the telescope system, had already been set up by former investigators at MIT LABA[6,8]. A very brief description is given here.

3.3.1 Accelerator neutron beam

A schematic of the accelerator neutron beam configuration is shown in Figure 3.2. The nuclear reaction for neutron production is ^{9}Be(d,n). Deuterons are accelerated to 1.5 MeV, and then directed to hit the beryllium target located close to the far end of the BNCS beam tube. In the source definition card in MCNP simulations, the angular distribution of the source neutrons[19] is approximated with 7 angular bins: 0°- 10°, 10°- 30°, 30°- 50°, 50°- 70°, 70°- 90°, 90°- 110°, and 110°- 180°. The normalized neutron emission probability in each angular bin is 1.2%, 8.7%, 15.1%, 15.2%, 13.4%, 15.0%, and 31.4%, respectively. The probability of emitting a source neutron in a forward direction (0°- 90°) is 57%, and that in a backward direction (90°- 180°) is 43%. The neutron energy distributions for the first angular bin (0°- 10°) and the last one (110°- 180°) are presented in Figure 3.3. The energy spectrum of the source neutrons is very hard, and the maximum neutron energy is over 6 MeV. The average neutron energy in the backward directions (2.9 MeV in the angular range of 110°-180°) is higher than that in the forward directions (2.0 MeV in the angular range of 0°-10°). A neutron beam with such an angular distribution and energy spectrum does not satisfy the requirements of boron neutron therapy well, since thermal neutrons are much more likely to be captured by ^{10}B in the synovium than fast neutrons. To make more neutrons useable in BNCS, the original neutron beam released from the beryllium target is moderated and directed toward the forward directions with the D_2O/graphite moderator/reflector assembly. D_2O is a very good neutron moderator. Compared to H_2O, it has smaller neutron absorption cross section and less photon yield. The graphite reflector surrounding the D_2O moderator is helpful to redirect the escaping

neutrons toward the beam direction to increase the neutron flux at the position. The dimensions of the D_2O moderator and the graphite reflector are illustrated in Figure 3.2.

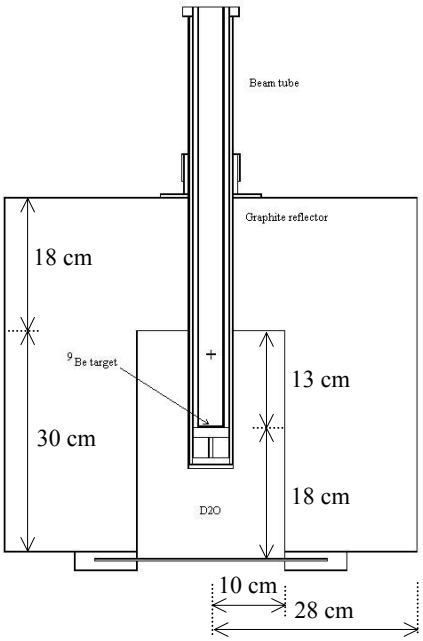

Figure 3.2 Schematic of beam tube, ^{9}Be target, and moderator/reflector assembly for BNCS neutron beam production.

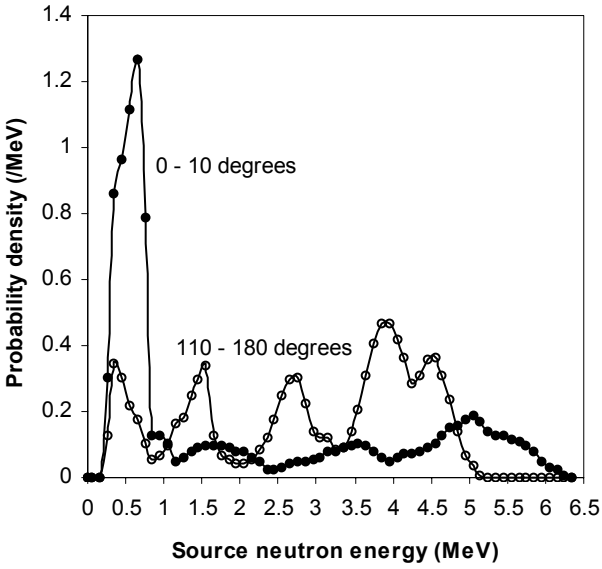

Figure 3.3 Angular distributions of neutrons emitted from ^{9}Be target in two angular bins: (0°, 10°) and (110°, 180°). The maximum neutron energy is over 6 MeV.

3.3.2 BNCS model for simulations

Figure 3.4 shows the entire BNCS simulation model[6], which includes the accelerator beam tube, target, target cooling apparatus, an anthropomorphic phantom[20] with one leg omitted, shielding wall, and back and side graphite reflectors around the knee position. The simulations are focused on irradiation of a knee joint, but by no means will the candidate joints for BNCS be limited only to knee joints. The major organs were originally included in the anthropomorphic phantom to allow calculation of patient effective dose, *E*, during joint irradiation. However, addition of the organs is not necessary for investigations of the telescope system and they make the geometrical description of the torso very complicated. MCNP simulations were run to examine whether this complexity is necessary. However, it was expected that the computational efficiency would be improved if a simpler description could be used. It was discovered that no difference in neutron and photon fluxes at the location of the knee joint could be recognized after the torso in Figure 3.4 was replaced with a cylinder of soft tissue. However, the improvement in computational efficiency (as determined by comparison of MCNP-generated FOM (figure of merit)[18]

which takes into consideration run time, precision and other factors) was also very limited (< 5%), and so the organs were all kept.

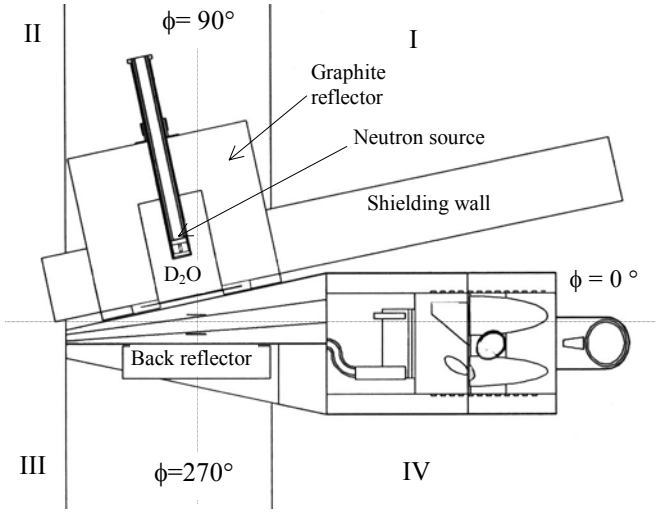

Figure 3.4 MCNP simulation model for BNCS, including target-moderator-reflector assembly, boron-containing shielding wall, anthropomorphic phantom, and back reflector (side reflectors are not visible). The space is divided into four quadrants: I (0° < φ <90°), II (90° < φ <180°), III (180° < φ <270°), and IV (270° < φ <360°). The slice shown is the X-Y plane at θ = 90°.

The shielding wall, with dimensions of 177.5 cm in length, 180 cm in height, and 20 cm in thickness[6], is made of polyethylene with 2% natural boron enrichment. It is very helpful in limiting the neutron dose to the human body. On the other hand, compared with that in the synovium, the total amount of ^{10}B contained in this wall is huge (~ 2240 g). The 478 keV boron photons emitted from this wall could affect the signal of the detected boron photons from the synovium. However, it is expected that the influence of these boron photons will be eliminated after the adoption of appropriately positioned collimators and detector shields.

The back and side reflectors (side reflectors are not visible in Figure 3.4) surround the knee joint and reflect the escaping neutrons back to the knee joint to increase the neutron flux in the synovium. After the location of the photon detector has been determined, a hole in one of the reflectors will be made to allow boron photons from the synovium pass to through in the direction of the detector.

3.3.3 Synovium representation and boron compound

The realistic configuration of the inflamed synovium is complex and irregular, and the exact description of the synovium with mathematical equations is very burdensome. In Figure 3.4, the synovium is represented with a thin shell region between two concentric cylindrical surfaces. The radii of

the two surfaces are 2.90 cm and 3.05 cm, respectively, and so the thickness of the shell is 0.15 cm. The length of this shell is 6 cm, and the total volume of the synovium is $\pi\times(3.05^2-2.9^2)\times6 = 16.823$ cm^3. The size and structure of rheumatoid synovium vary from patient to patient. Therefore, it is impossible to model a synovium that can represent all possible sizes and structures that a real synovium can have. This simplified synovium model is used to give a very rough picture of boron compound distribution, and is not intended to imitate a real synovium. For exploring the feasibility of a telescope system for boron dose determination, such a model is sufficient. The effect of synovium configuration on boron photon production in the synovium and boron photon detection of the telescope will be discussed later in Chapter 7.

The boron compound modeled in simulations is ^{10}B-enriched $K_2B_{12}H_{12}$. However, the results for $K_2B_{12}H_{12}$ will also be valid for other compounds. From the point of view of physics, only the amount of ^{10}B and its spatial distribution affect the production and the detection of boron photons, and the nature of the compound is not relevant. The synovial boron concentration modeled ranges from 1,000 ppm to 19,000 ppm. Practical BNCS treatments are unlikely if synovial boron concentrations are much less than 1,000 ppm since irradiation time would be long and healthy tissue dose would be correspondingly high; 19,000 ppm represents the maximum average synovial boron concentration measured during in vivo boron uptake studies.

3.3.4 Coordinate system

In Figure 3.4, the total space available in the radiation vault is divided into four regions (quadrants), which are denoted as I, II, III, and IV. Spherical coordinates (r,θ,φ) are employed to represent a spatial location. The symmetrical center of the synovium is selected as the origin of the coordinate system, i.e., r is the distance relative to the center of the synovium.

3.4 Ultimate fate of the source neutrons

From the energy and angular distribution of the source neutrons (Figure 3.3), it is expected that only a small fraction of the source neutrons are eventually absorbed in the synovium through boron neutron capture reactions. A large number of neutrons are stopped in the shielding wall and other features in the therapy room, most likely after one or more scatterings.

3.4.1 Neutron absorption and boron dose in the synovium

Monte Carlo simulations were performed to estimate the number of ^{10}B(n,α) reactions in the synovium under various boron concentrations. At the same time, the synovial dose was also determined with three different methods. The first method uses the F6 tally[18] in MCNP to directly seek the energy

deposited per unit mass of synovium. Two options (F6:n and F6:n,p) were both tried. In F6:n tallies, only the kinetic energy deposited by neutrons through heavy charged particles following reactions such as (n,α), (n,n), and (n,n′) is recorded, and the photon energy deposited in the synovium following (n,γ) and (n,n′γ) reactions is not included. On the other hand, in F6:n,p tallies, the energy deposited through heavy charged particles and neutron produced photons is summed. In the second method, the total energy deposited in the synovium through boron neutron capture reactions is calculated as the product of the number of boron neutron capture reactions (estimated using the F4 tally plus the FM card[18]) and the average energy released in each capture, which is 2.310×94%+2.792×6%= 2.339 MeV. Then the averaged boron dose in the synovium equals the total energy divided by the synovial mass. In the last method, the neutron flux in the synovium is determined first using the F4 tally, and the boron dose is obtained by multiplying flux-to-dose conversion factors by the neutron flux.

Figure 3.5 shows the number of boron neutron capture reactions in the synovium under various synovial boron concentrations: 0, 1,000, 2,000, 5,000, 10,000, 15,000, and 19,000 ppm. Clearly, the relationship between the number of ^{10}B(n,α) reactions and the synovial boron concentration is nonlinear, and a tendency to saturation becomes prominent at high boron concentrations (over 10,000 ppm). This effect of neutron self-shielding in the target tissue is more explicit in Figure 3.6, which presents the dose contribution per ppm of ^{10}B under various boron concentrations. The curve in Figure 3.6 decreases quickly with increasing boron concentration, which indicates that the average thermal neutron flux decreases significantly at high synovial boron concentrations. In addition, neutron flux suppression is already apparent at 1,000 ppm, and hence the self-shielding effect has an appreciable influence over the entire range of synovial boron concentrations in BNCS.

Table 3.1 gives the doses estimated with the three different methods. These results are very comparable. Columns 2, 3, and 4 display the total synovial dose, the total synovial neutron dose, and the synovial boron dose, respectively. The boron dose is clearly dominant in BNCS, and the photon dose and the neutron dose through other nuclear reactions add negligible dose to the total dose when the boron concentration is over 5,000 ppm.

On the other hand, the fraction of source neutrons absorbed in the synovium is very small. For instance, at 1,000 ppm, only 0.13% of the source neutrons are absorbed in the synovium, and the number is 0.68% and 0.89% at 10,000 ppm and 19,000 ppm, respectively. That is, in the range of the boron concentration in BNCS, less than 1% of the neutrons emitted from the beryllium target are used, and over 99% of the neutrons are ultimately absorbed in other components in the radiation vault, as described below.

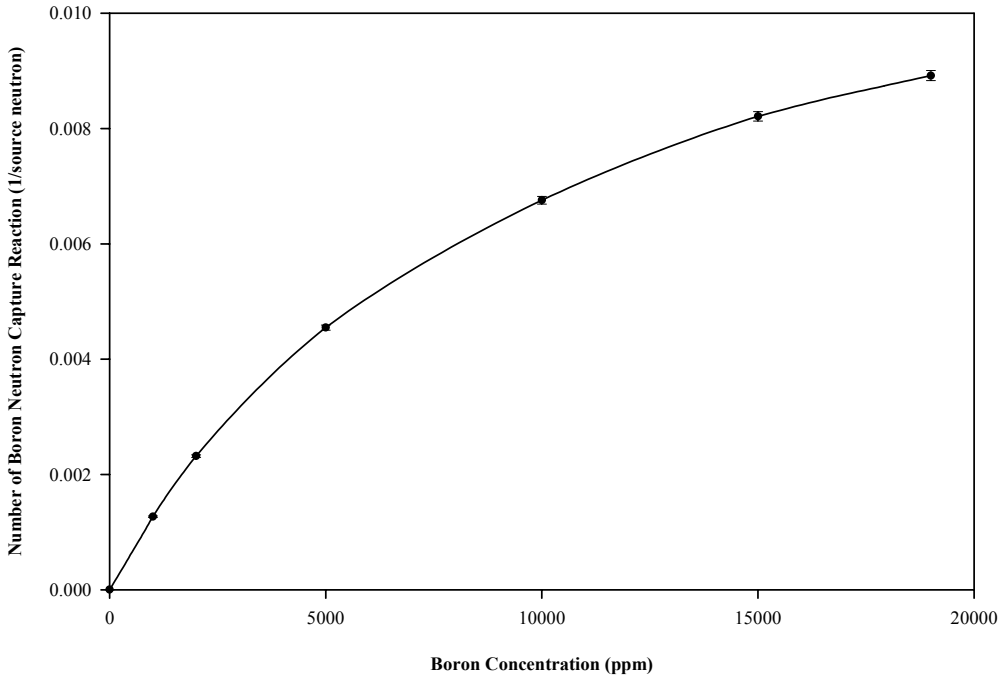

Figure 3.5 Number of $^{10}B(n,\alpha)$ reactions in the synovium as a function of the synovial boron concentration.

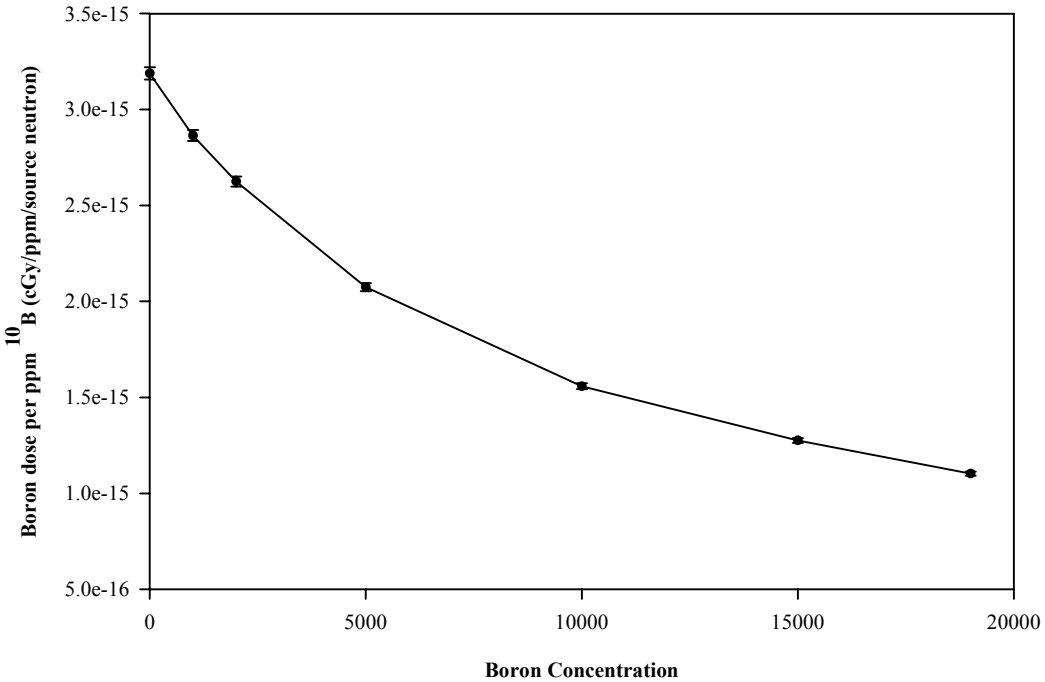

Figure 3.6 Synovial boron dose per ppm of ^{10}B as a function of the synovium boron concentration.

Table 3.1 Synovial dose estimated with three different methods (unit: Gy/source neutron)

Boron Concentration (ppm)	Neutron dose + Photon dose (F6:n,p)	Neutron dose (F6:n)	Boron dose (F4:n+FM)	Boron dose (F4:n+DE+DF)
0	1.96e-15	1.50e-15	0	0
1,000	3.02e-14	2.97e-14	2.82e-14	2.86e-14
2,000	5.36e-14	5.31e-14	5.16e-14	5.25e-14
5,000	1.03e-14	1.03e-13	1.01e-13	1.04e-13
10,000	1.53e-13	1.52e-13	1.50e-13	1.56e-13
15,000	1.85e-13	1.84e-13	1.83e-13	1.91e-13
19,000	2.01e-13	2.00e-13	1.98e-13	2.09e-13

3.4.2 Neutron absorption in other components

Monte Carlo simulations were also conducted to explore neutron absorption in other components of the BNCS therapy situation. Table 3.2 gives a summary of the results assuming a synovial boron concentration of 10,000 ppm. Since the fraction of neutrons absorbed in the synovium is so small (< 1%), variations in synovial boron concentration will not change the overall situation of neutron absorption. From Table 3.2, the boron-containing shielding wall absorbs 36.5% of source neutrons, among which 35.6% are captured by ^{10}B nuclei. The concrete floor, ceiling, and walls altogether absorb 34.0% of source neutrons.

Table 3.2 Neutron absorption in various components in BNCS model (boron concentration: 10,000ppm)

	Absorption (%)
Synovium	0.7
Boronated shielding wall	36.5
Floor, ceiling and walls	34.0
Inside accelerator	9.8
Li-poly delimeter	8.9
Air	2.5
Leg	1.3
D_2O/graphite	2.4
Torso+head	0.1
Escaped	3.6

Only the neutrons that penetrate through the front surface of the D_2O moderator are used for irradiation of the knee joint. Simulation results showed that over 90% of the source neutrons leave the D_2O moderator through the side and back surfaces. If the graphite reflector surrounding the D_2O moderator is absent, only 3% of the neutrons will hit the front surface of the moderator in the direction of the synovium. With the graphite reflector present, the number increases from 3% to 10%. This demonstrates the effectiveness of the reflector in beam directionality. On the other hand, nearly 60% of

the neutrons escape from the outer surfaces of the graphite reflector and enter the shielding wall or the air in the therapy room. The neutron flux in the shielding wall is expected to be large, and this is consistent with the large number of boron neutron capture reactions detected in the shielding wall as shown in Table 3.2. The leakage of neutrons to the air predicts the existence of a strong neutron field in regions I and II, since the graphite reflector is located in these regions.

Given the high neutron flux in the shielding wall and its composition, a large number of boron photons will be emitted from the shielding wall. A strong boron photon field is therefore formed in the radiation vault, especially at the places near the shielding wall in regions I and II. The influence from the boron photons emitted from the shielding wall will be discussed later in the chapter (section 3.5.4) and in the next chapter when the collimator and detector shield have been added.

3.5 Neutron and Photon spatial distribution inside the therapy room

To select the location of the photon detector, detailed information regarding the neutron and photon background distributions in the radiation vault must be obtained. To achieve the least detector shielding and the least detector damage, a location with the weakest neutron and photon backgrounds is the best.

To examine the background in the therapy room, point detectors (F5 tallies in MCNP[18]) were located at various directions and distances from the synovium. The neutron and photon fluxes at these locations were estimated. In all simulations, the synovial boron concentration was kept at zero ppm; therefore, the tallied boron photons were all from the boron-containing shielding units. To specifically analyze the influence of neutron scattering by the floor, the ceiling, and the surrounding walls of the therapy room, two cases, with and without the concrete structure of the radiation vault, were compared.

The possible combinations of r, θ, and φ are infinite, and only some representative locations were selected to examine the spatial distributions of neutrons and photons. Five polar angles (θ = 0°, 45°, 90°, 135° and 180°) and eight azimuthal angles (φ = 0°, 45°, 90°, 135°, 180°, 225°, 270°, and 315°) were selected. Since the angle φ is meaningless under the polar angles of 0° and 180° (the projection of any vector with a polar angle of 0° or 180° into the XOY plane is at the origin with a zero length), only one azimuthal angle of an arbitrary value was chosen for these two special polar angles. The coordinate pair (θ,φ) determines the direction, so altogether 3×8+2 = 26 directions were investigated. In each direction, three distances r were chosen: 100 cm, 200 cm, and 250 cm. In some directions, not all the three distances were accessible. For example, the location of (100 cm, 90°, 0°) was not practical because it was inside the torso of the human body; in other directions, r could not be 200 cm or 250 cm, otherwise the location would be outside of the radiation vault, or inside the concrete structure of the radiation vault. Only the positions in the air and inside the therapy room were accepted. Under this limitation, the real

number of detector positions was 54, instead of 26×3 = 78. The collected information at each detector position included thermal neutron flux (< 1eV), total neutron flux, 478 keV photon flux, 511 keV photon flux, and 2223 keV photon flux.

3.5.1 Neutron flux in the therapy room

The normalized neutron fluxes at the 54 detector locations appear in Figure 3.7, which contains six panels. The results in Figure 3.7 are organized according to the distance *r* (100 cm, 200 cm or 250 cm); the thermal and total neutron fluxes are displayed in separate panels. There is not an explicit azimuthal angle corresponding to the polar angle of 0° or 180°, and an angle of 90° is chosen for these two polar angles.

From Figure 3.7, for all distances, *r*, the neutron flux peaks in regions I and II (0°≤φ≤180°, see Figure 3.4). It is likely that the maximum flux is located somewhere around φ = 90°. This is because of the location of the beryllium target (region II) and the angular distribution of the source neutrons. Neutrons emitted in the backward directions have less possibility of being moderated and absorbed than those emitted in the forward directions. This is especially true for those neutrons emitted into the vacuum beam tube; except for the wall of the beam tube, there is no scattering material preventing these neutrons from reaching regions I and II. Since the beam tube lies in the direction of (θ,φ) = (90°, 100°), it is reasonable to assume that the neutron flux peaks somewhere close to this direction.

Compared to regions I and II, the neutron flux in regions III and IV (180°≤ φ ≤360°) is much lower. For example, for θ = 90° and *r* = 100 cm, the total neutron flux at φ = 90° is 3.5, 4.3, and 5.3 times higher than that at φ = 225°, 275° and 315°, respectively. The photon detector should therefore be located in region III or IV in order to reduce radiation damage to the detector, photon background in the detector, and overall shielding requirements.

In Figure 3.8, the simulation results are reorganized to show how the neutron flux varies with distance in certain directions in regions III and IV. The neutron flux continues to drop as the distance *r* increases. However, the neutron flux falls rapidly with distance when *r* is between 100 cm and 200 cm, and more slowly when the distance is over 200 cm. In Figure 3.8, the neutron flux in the direction of (θ,φ)= (90°, 315°) is much weaker than that in the other three directions.

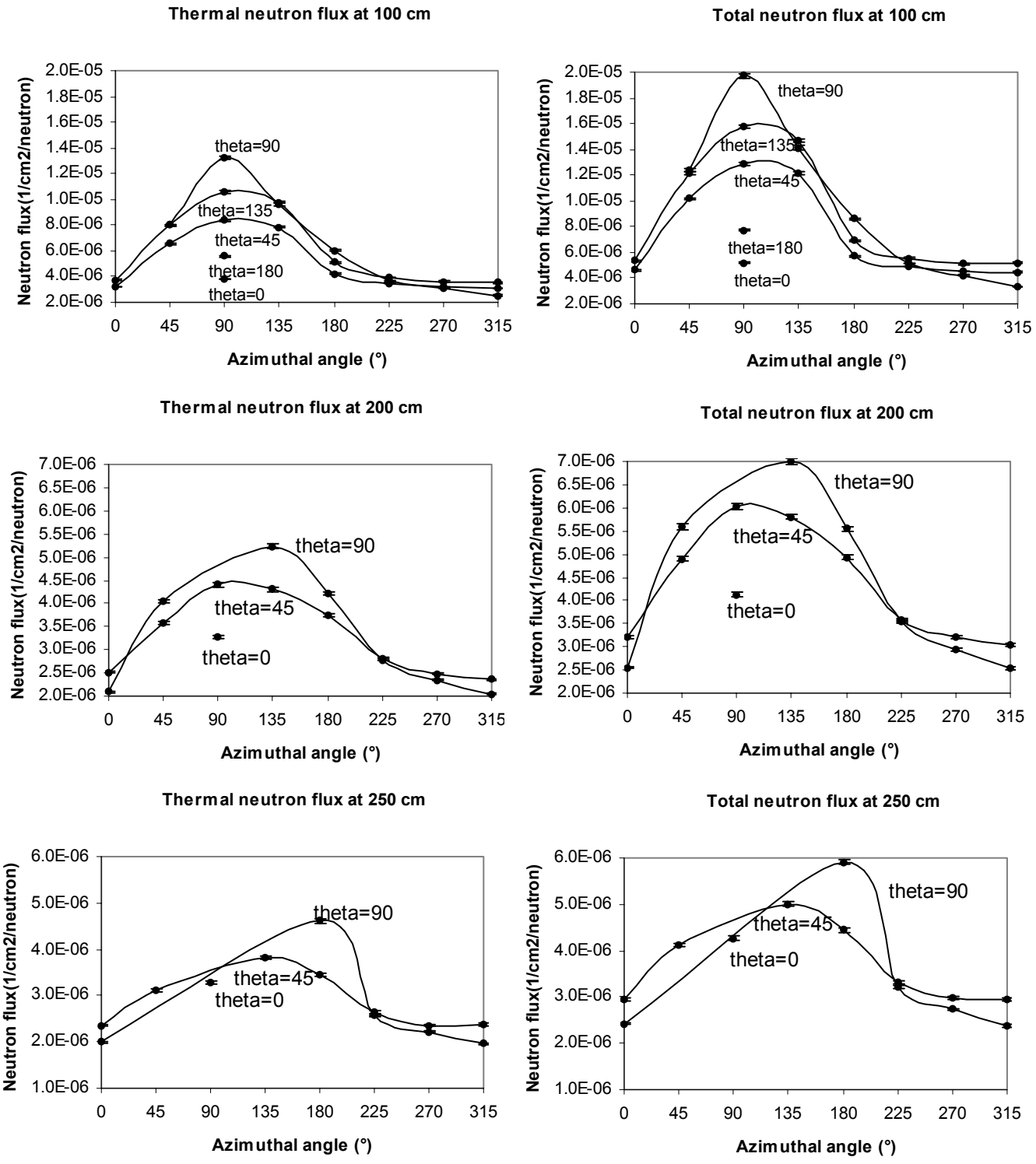

Figure 3.7 Thermal and total neutron flux estimated at three different synovium-to-detector distances (100 cm, 200 cm, and 250 cm) inside the radiation vault (26 directions for each distance), with the presence of the floor, ceiling and walls of the radiation room.

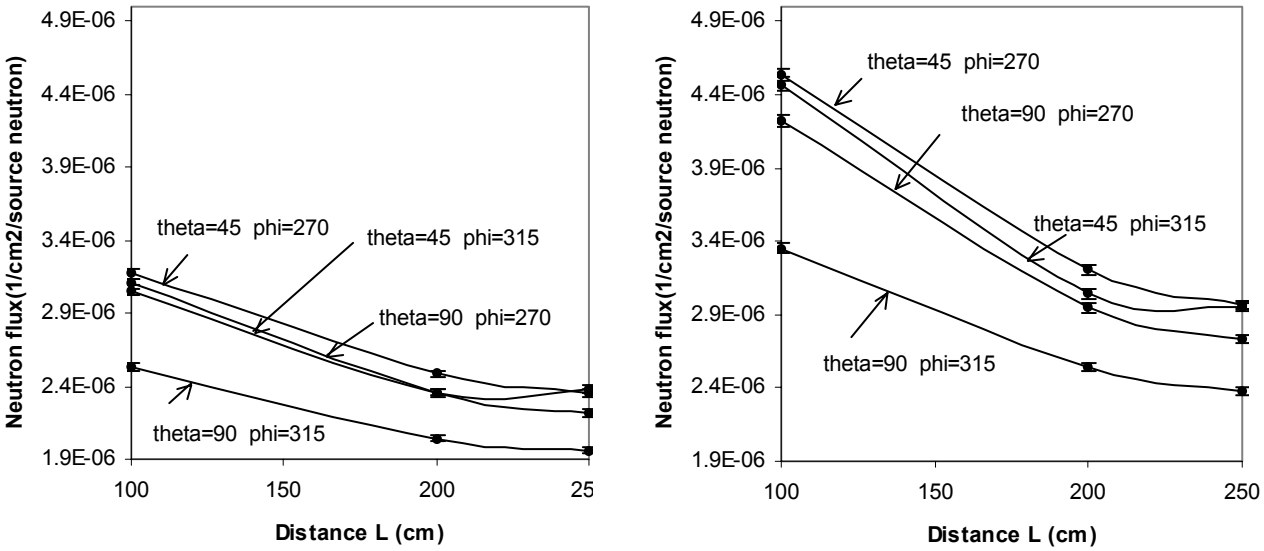

Figure 3.8 Thermal and total neutron flux as a function of synovium-to detector distance in four directions in regions III and IV with the presence of the floor, ceiling and walls of the radiation room.

3.5.2 Photon flux in the therapy room

Table 3.3 lists several primary photon emitters in the simulation model. Since MCNP only traces prompt gamma rays, the delayed gamma rays are not included. The leading photon emitter is the concrete of the radiation vault, which releases 0.68 photons per source neutron on average. The boron-containing shielding wall emits 0.34 photons per source neutron, the majority of which are from boron neutron capture reactions.

Figure 3.9 shows a typical photon spectrum, recorded at (r, θ, φ) = (200 cm, 90°, 270°). The distinguishable peaks include the 478 keV boron peak, the 511 keV annihilation peak, and the 2223 keV hydrogen peak. The 478 keV peak is the most prominent feature in the spectrum, which indicates that the influence from the boron-containing polyethylene wall is significant. Since MCNP does not take into account the Doppler effect, the boron photon peak appears as a single line, instead of an energy band of 15 keV (470 to 485 keV). In this spectrum, the energy resolution of a real photon detector is not considered, and so the discrete gamma peaks emerge as single lines. This is different from an actual photon spectrum collected by a photon detector, in which the signal gamma lines are broadened to peaks with a width determined by the energy resolution of a specific detector. Moreover, other features such as a Compton plateau appear in the measured spectrum. In particular, if a NaI detector is used, the 478 keV peak and 511 keV peak will not be distinguished separately.

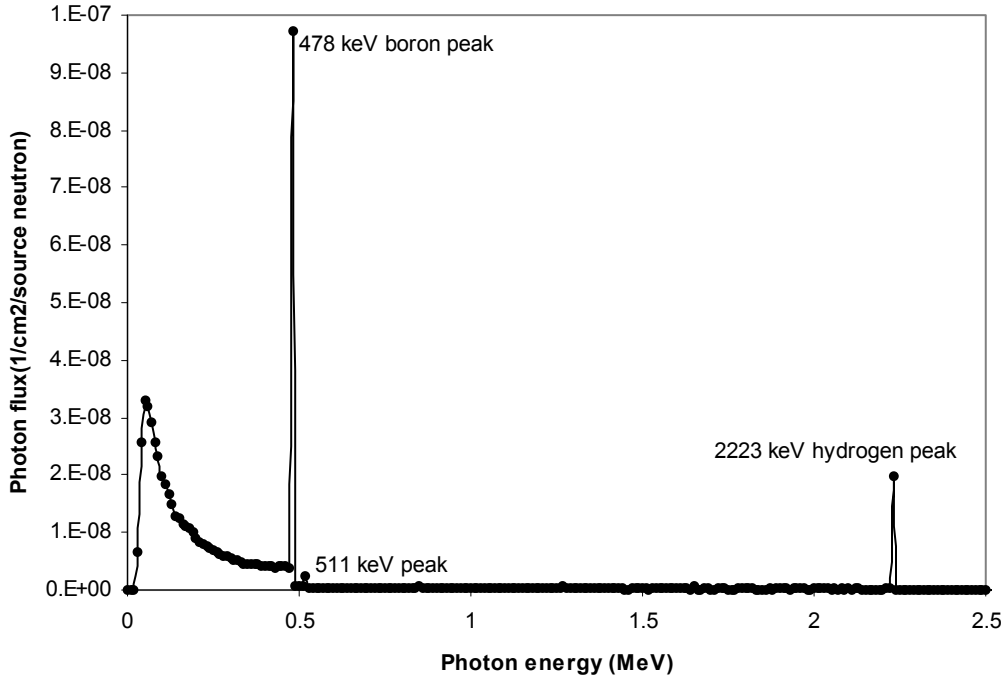

Figure 3.9 Simulated photon flux spectrum at position (200 cm, 90°, 270°).

Photon fluxes at the 54 locations are summarized in Figure 3.10, which contains nine panels for three peaks (478 keV peak, 511 keV peak and 2223 keV peak) at three distances (100 cm, 200 cm, and 250 cm). The distribution of the 478 keV photon flux shows obvious similarities to that of the neutron flux. The flux in regions I and II is generally much higher than that in regions III and IV. This is predictable since the shielding wall is located in regions I and II, which is the main location for boron photon production. For the 511 keV and the 2223 keV photons, the highest flux also appears in regions I and II. This is because of the presence of several major photon emitters in regions I and/or II (the shielding wall, the stainless steel beam tube, and the teflon nozzle).

The variation of the photon flux with distance from the synovium in four directions in regions III and IV is presented in Figure 3.11. Similar to the tendency of the neutron flux, all photon fluxes decrease as the detector is placed further away. The decrease with distance is also more apparent when the distance is less than 200 cm, and the dropping tendency slows down when the distance is greater than 200 cm. This decrease is less than that predicted by a $1/r^2$ relationship because the neutron and photon fluxes also include the contribution from particles scattered from the concrete floor, ceiling, and walls.

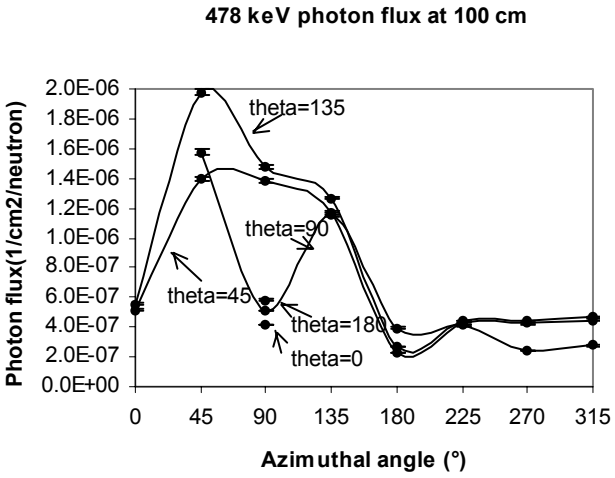
478 keV photon flux at 100 cm
Photon flux(1/cm2/neutron)
2.0E-06
1.8E-06
1.6E-06
1.4E-06
1.2E-06
1.0E-06
8.0E-07
6.0E-07
4.0E-07
2.0E-07
0.0E+00
theta=135
theta=90
theta=45
theta=180
theta=0
0
45
90
135
180
225
270
315
Azimuthal angle (°)

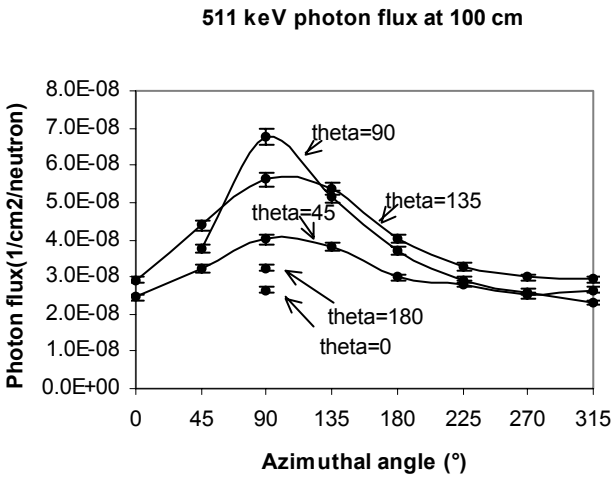
511 keV photon flux at 100 cm
Photon flux(1/cm2/neutron)
8.0E-08
7.0E-08
6.0E-08
5.0E-08
4.0E-08
3.0E-08
2.0E-08
1.0E-08
0.0E+00
theta=90
theta=135
theta=45
theta=180
theta=0
0
45
90
135
180
225
270
315
Azimuthal angle (°)

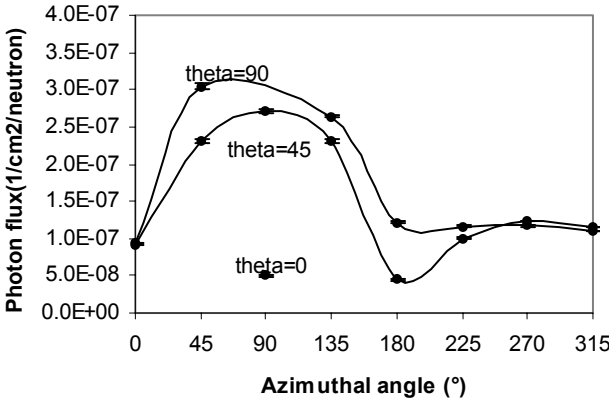
478 keV photon flux at 200 cm
Photon flux(1/cm2/neutron)
4.0E-07
3.5E-07
3.0E-07
2.5E-07
2.0E-07
1.5E-07
1.0E-07
5.0E-08
0.0E+00
theta=90
theta=45
theta=0
0
45
90
135
180
225
270
315
Azimuthal angle (°)

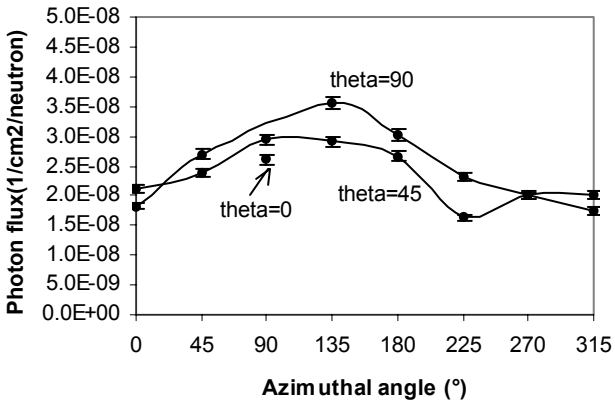
511 keV photon flux at 200 cm
Photon flux(1/cm2/neutron)
5.0E-08
4.5E-08
4.0E-08
3.5E-08
3.0E-08
2.5E-08
2.0E-08
1.5E-08
1.0E-08
5.0E-09
0.0E+00
theta=90
theta=0
theta=45
0
45
90
135
180
225
270
315
Azimuthal angle (°)

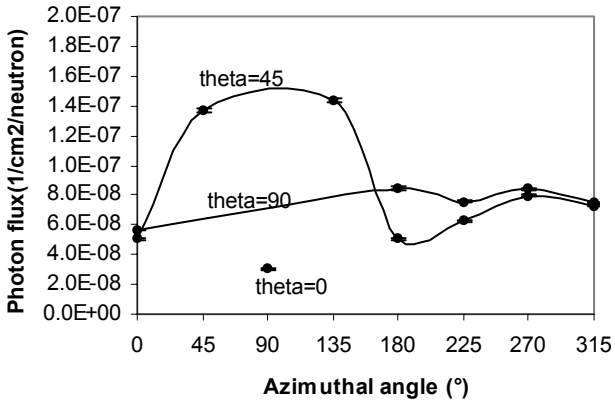
478 keV photon flux at 250 cm
Photon flux(1/cm2/neutron)
2.0E-07
1.8E-07
1.6E-07
1.4E-07
1.2E-07
1.0E-07
8.0E-08
6.0E-08
4.0E-08
2.0E-08
0.0E+00
theta=45
theta=90
theta=0
0
45
90
135
180
225
270
315
Azimuthal angle (°)

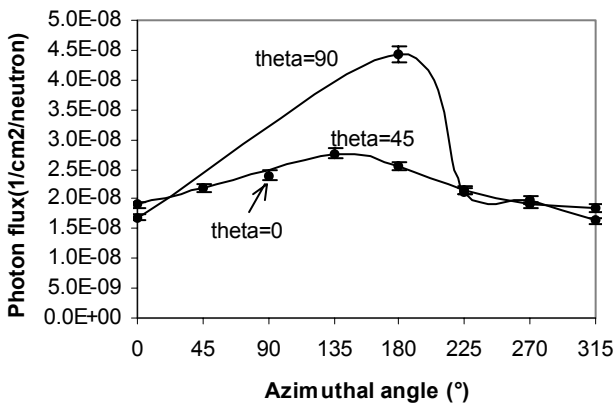
511 keV photon flux at 250 cm
Photon flux(1/cm2/neutron)
5.0E-08
4.5E-08
4.0E-08
3.5E-08
3.0E-08
2.5E-08
2.0E-08
1.5E-08
1.0E-08
5.0E-09
0.0E+00
theta=90
theta=45
theta=0
0
45
90
135
180
225
270
315
Azimuthal angle (°)

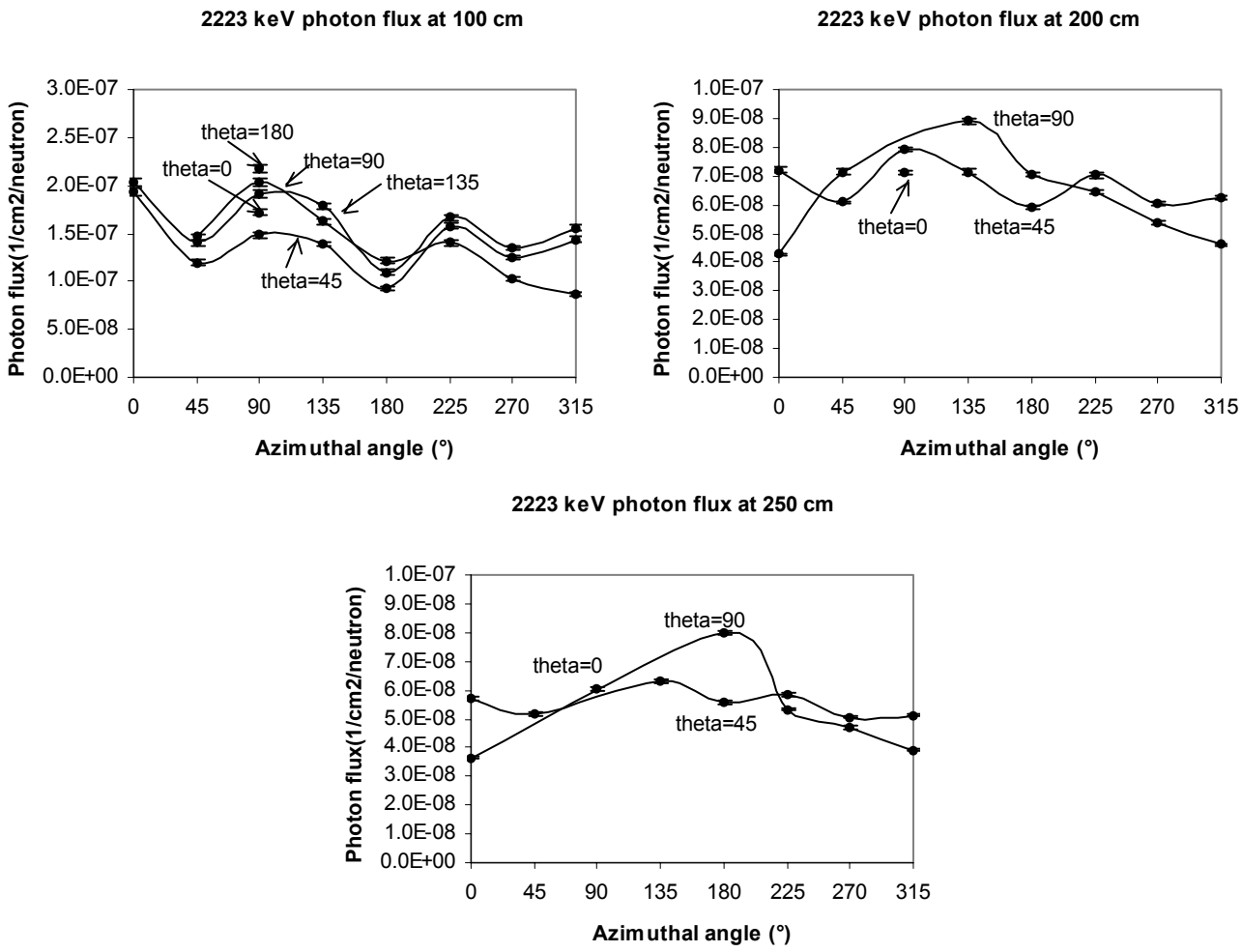

Figure 3.10 478 keV, 511 keV, and 2223 keV photon flux estimated at three different synovium-to-detector distances (100 cm, 200 cm, and 250 cm) inside the radiation vault (26 directions for each distance), with the presence of the floor, ceiling and walls of the radiation room.

Results from the simulations suggest that, the distance of the detector from the synovium should be set at approximately 200 cm since further increases of this distance will no longer significantly reduce the neutron and photon fluxes. In addition, at this distance there is still enough space behind the detector for positioning of shielding materials to reduce background neutron and photon contribution.

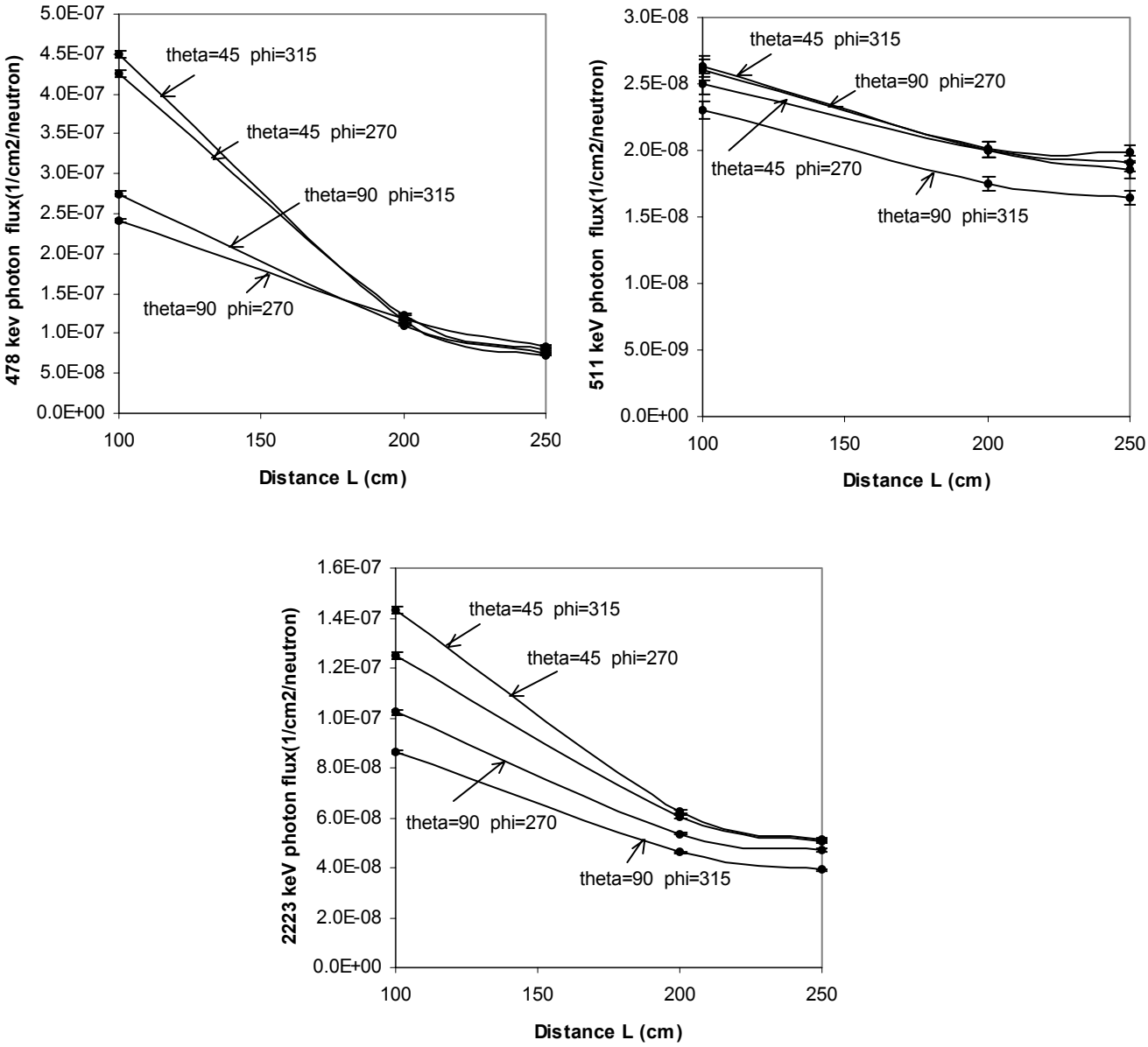

Figure 3.11 478 keV, 511 keV and 2223 keV photon flux as a function of synovium-to-detector distance in four directions in regions III and IV with the presence of the floor, ceiling and walls of the radiation room.

3.5.3 Influence of the concrete components

To take into account the neutron scattering and photon contributions from the concrete radiation vault, another set of simulations was performed with the walls, the floor, and the ceiling removed from the model. The new estimates of neutron and photon flux are exhibited in Figure 3.12 and Figure 3.13,

respectively. In general, compared to Figure 3.7 and Figure 3.10, the overall shapes of the flux curves are similar, however the magnitudes are reduced.

Neutrons and photons reaching the concrete floor, ceiling, and walls can be scattered back into the radiation vault, increasing the neutron and photon fluxes in this room. Moreover, neutrons can also produce photons in the concrete through inelastic scattering or capture, and these neutron-induced photons will increase the photon flux in the radiation vault. According to Table 3.2, 1/3 of the source neutrons are ultimately absorbed in the concrete; since the scattering cross section is larger than the absorption cross section, more scattering events than captures occur in the concrete. Therefore, the concrete structure is expected to have appreciable impact on the background distribution in the radiation vault. In Figure 3.7 and Figure 3.10, the neutron and photon fluxes at $\theta = 180°$ are always higher than those at $\theta = 0°$. Similarly, the fluxes at $\theta = 135°$ are always higher than those at $\theta = 45°$. The discrepancy comes from the contribution from the floor and the ceiling: the floor is 100 cm from the synovium, but the ceiling is 250 cm from it. Therefore, for a fixed distance *r*, the detectors in the directions with a polar angle of 180° or 135° receive more photons and neutrons scattered from the floor than the detectors in the directions with a polar angle of 45° or 0° receive from the ceiling. If the explanation is correct, after the ceiling and the floor are taken out from the model, this distinction in flux should disappear. In the top two panels in Figure 3.12 and the first three panels in Figure 3.13, the flux curves for $\theta = 45°$ and $\theta = 135°$ do overlap to each other. In addition, the data points for $\theta = 180°$ and $\theta = 0°$ match each other.

The presence of the concrete surroundings increases the neutron and photon fluxes at all locations in the therapy room. On the other hand, this increase is position dependent. The neutron flux at positions in regions I and II is more affected by the concrete structure than that at positions in regions III and IV. For example, at the location (100 cm, 90°, 90°) (in regions I and II), the neutron flux without and with the presence of the concrete surroundings is 1.38×10^{-5} and 1.97×10^{-5} /cm^2/source neutron, respectively, i.e. a flux increase of $1.97\times10^{-5}-1.38\times10^{-5} = 5.9\times10^{-6}$ /cm^2/source neutron. By comparison, at another location (100 cm, 90°, 270°) (in regions III and IV), the neutron flux without and with the presence of the concrete surroundings is 1.86×10^{-6} and 4.22×10^{-6} /cm^2/source neutron, respectively, and the flux increase is 2.4×10^{-6} /cm^2/source neutron, 41% of that at the location (100 cm, 90°, 90°). In addition, the flux increase resulting from the presence of the concrete is also distance dependent. In regions III and IV, at 100 cm, the total neutron flux is increased by a factor of 2 to 3 after the concrete vault is included in the model. This factor goes up to 4 to 8 at 200 cm, and 6 to 10 at 250 cm. The explanation is that at larger distances the direct contribution from the source is weaker, and the contribution from the neutrons scattered from the concrete becomes increasingly more important.

The ultimate way to eradicate the background boron photon contribution is to replace the boronated polyethylene shielding material with a material containing no ^{10}B. Polyethylene containing ^{6}Li is a good choice. ^{6}Li is also effective in neutron absorption (the thermal neutron cross section of ^{6}Li is 940 barns) and a merit of it is that no photons are emitted following ^{6}Li (n, α) reactions. Simulations with a lithium-containing shielding wall in the model showed that the function of the shielding wall was not affected (as determined by a comparison of flux reduction) and no boron photons could be detected.

3.5.4 Approximate direction of the detector

From the above analysis, the detector should be located in region III or IV to take advantage of lower neutron and photon background intensities. Positions with a polar angle θ of 90° could be good candidates since these positions are less affected by the presence of the floor or the ceiling. The neutron flux is the lowest in the direction of (θ,φ) = (90°, 0°); however, the detector cannot be put in this direction since any boron photon from the synovium has to penetrate the thigh, the torso, and the head of the patient before arriving at the detector.

The photon count in the boron peak region comes from several sources: the contribution from the synovium, which carries useful information about the synovial boron dose, the contribution from other boron-containing components in the therapy room such as the shielding wall, and the contribution from high-energy photons that Compton scatter within the detector. In above simulations, there was no boron compound modeled in the synovium. After 10,000 ppm of ^{10}B was loaded in the synovium, simulations indicated that for a detector without any collimation and shielding in regions III and IV, the boron photon count from the synovium would represent less than one percent of total count in the boron peak region of the collected spectrum. Therefore, the useful information is completely concealed by the background count. The way to deal with this situation is to add appropriately designed collimators and detector shields to significantly reduce the count contribution from the shielding wall and other objects in the radiation vault.

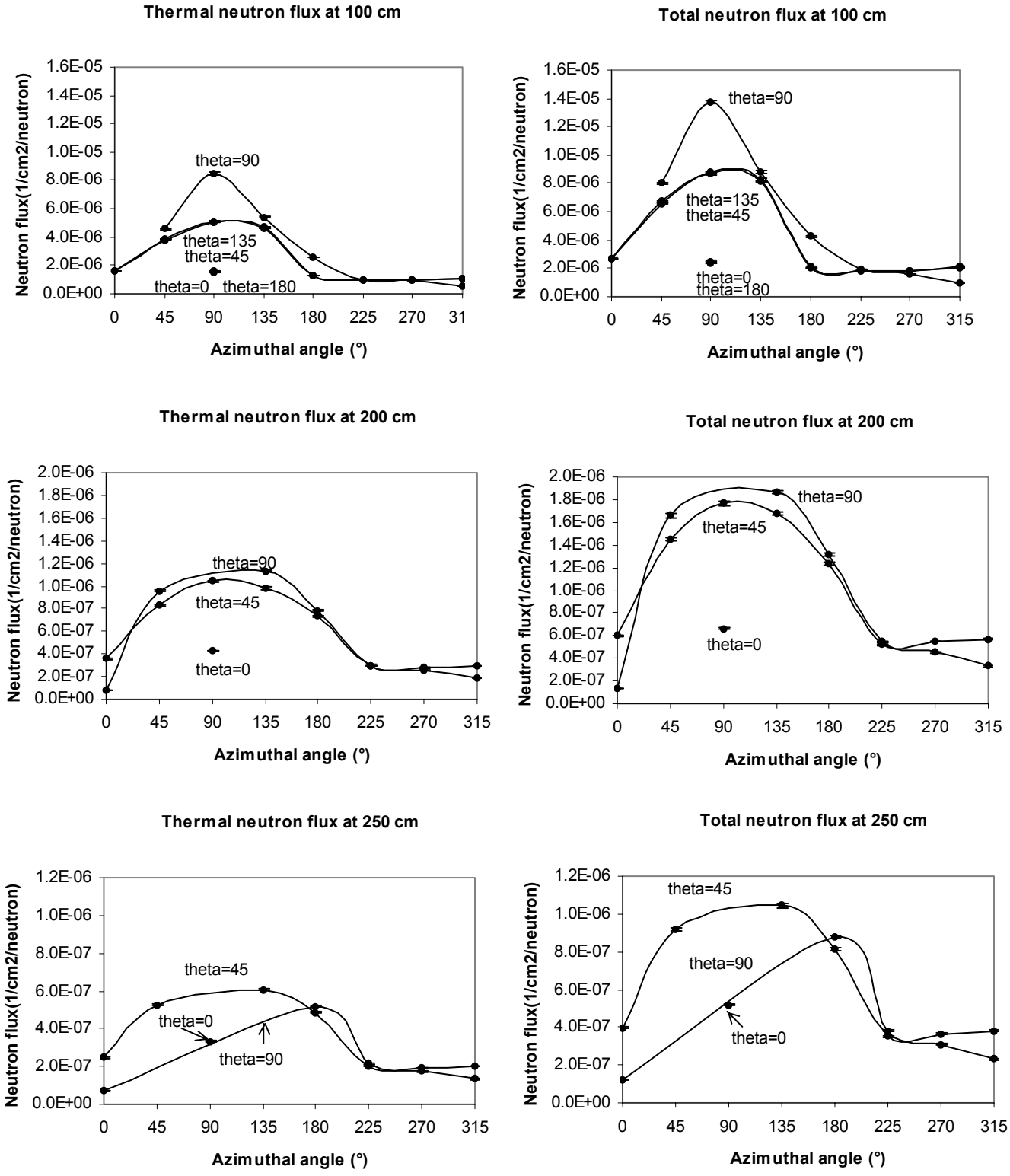

Figure 3.12 Thermal and total neutron flux estimated at three different synovium-to-detector distances (100 cm, 200 cm, and 250 cm) inside the radiation vault (26 directions for each distance), **without** the presence of the floor, ceiling and walls of the radiation room.

478 keV photon flux at 100 cm

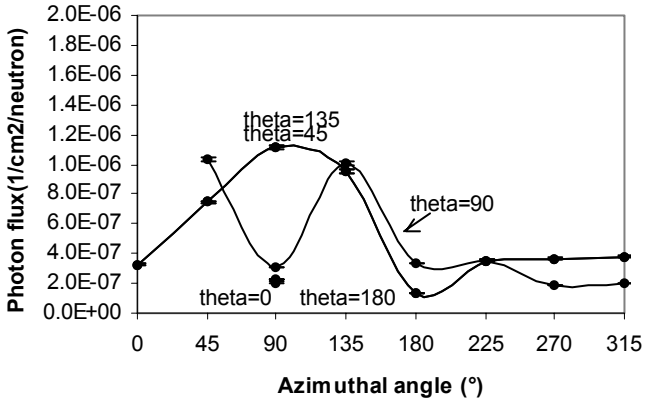

511 keV photon flux at 100 cm

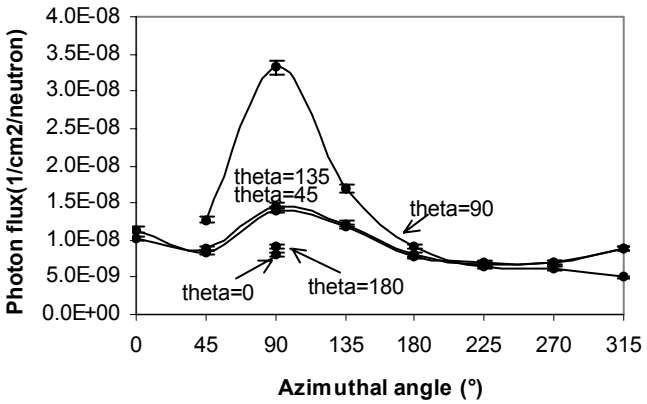

478 keV photon flux at 200 cm

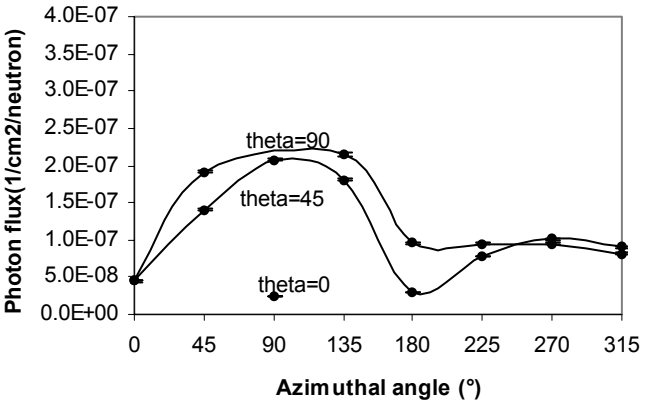

511 keV photon flux at 200 cm

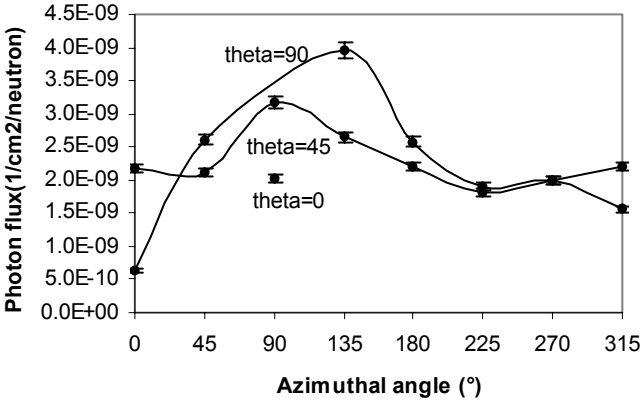

478 keV photon flux at 250 cm

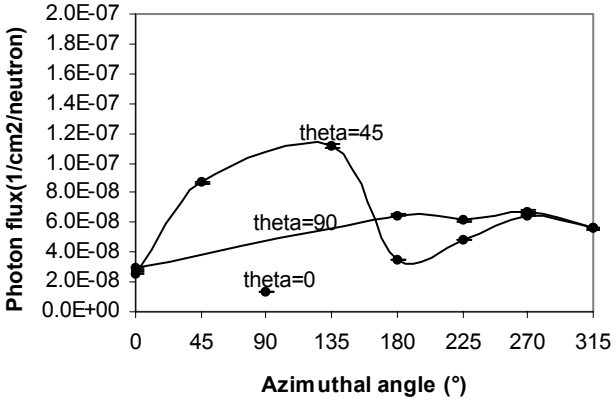

511 keV photon flux at 250 cm

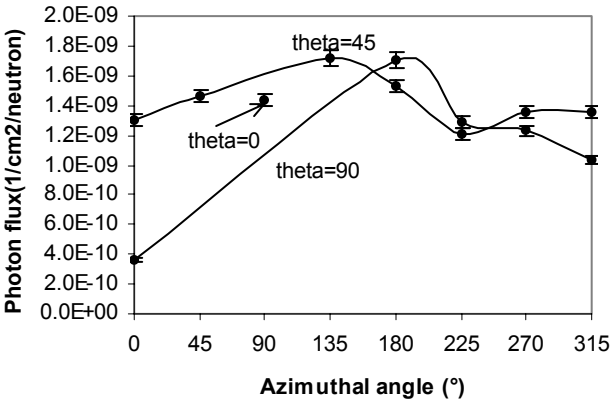

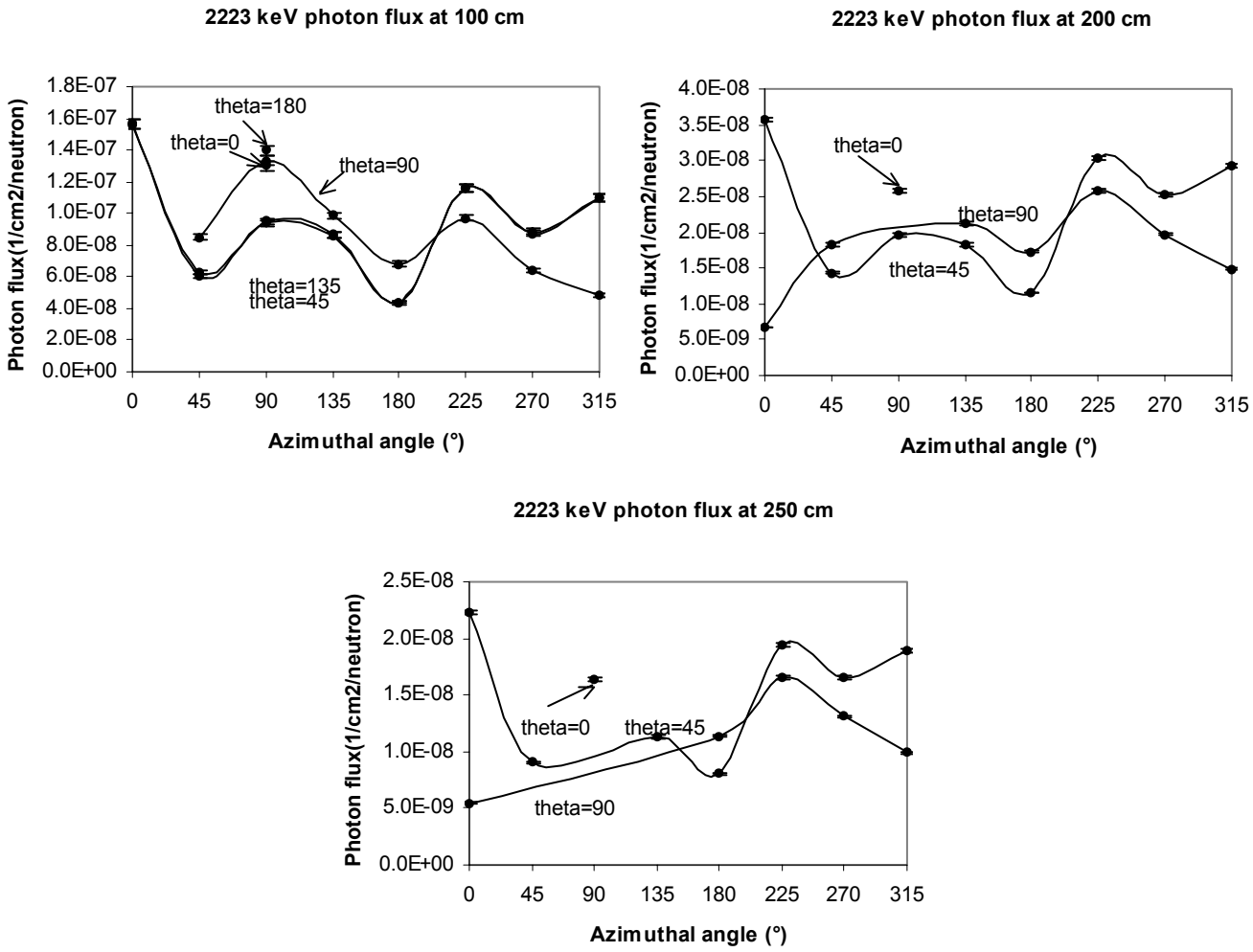

Figure 3.13 478 keV, 511 keV, and 2223 keV photon flux estimated at three different synovium-to-detector distances (100 cm, 200 cm, and 250 cm) inside the radiation vault (26 directions for each distance), **without** the presence of the floor, ceiling and walls of the radiation room.

3.6 Conclusions

Monte Carlo simulations using the MCNP code were carried out to design a telescope system for synovial boron dose determination in BNCS. The first task was to select an appropriate location for the photon detector. From the simulation results presented in this chapter, the detector should be positioned in region III or IV to take the advantages of weaker neutron and photon fields.

Without sufficient collimation and detector shielding, the signal from detected boron photons originating from the synovium is completely buried in the background photon count. At the same time, the neutron field is still too strong for a photon detector to endure. Appropriately designed collimators and

detector shields have to be added to the system to reduce the neutron field to protect the detector from radiation damage and to reduce the background photon count so that the signal from the boron photons emitted from the synovium can be discerned. In the next chapter, the focus will be on the design of an appropriate collimator and a detector shield for the telescope system. After addition of the collimator and detector shield, the candidate locations determined in this chapter will be evaluated quantitatively with several figures of merit. Then, the exact location of the photon detector will be determined.

Chapter 4 Design of the telescope system

Before setting up a real telescope system in the BNCS radiation vault, the feasibility of such a system has to be studied. One crucial point is whether or not the boron photons from the synovium can be detected above the background. The approximate direction and distance of the photon detector from the synovium were determined in the last chapter. In this chapter, collimation and the detector shield are investigated. The efficacy of the collimator and the shield is examined, and the performance of the detector at various system parameters is explored analytically and in simulations. The suitable location of the detector is obtained at the end of this chapter.

4.1 Collimation and detector shielding

4.1.1 Collimator and detector shield

The candidate locations of the detector were determined in the last chapter to be in regions III or IV and be approximately 200 cm from the synovium. After the collimator and the shield are added, more detailed information about each location, such as the neutron flux, the boron photon count from the synovium, and other figures of merit, will be available. This information is used to evaluate the advantages and disadvantages of each location, and is used to choose the final location of the photon detector.

In the BNCS therapy room, prior to sufficient collimation and shielding, the detected boron photon signal from the synovium is completely buried in the background. The overwhelming background count not only deteriorates the precision of determining the boron photon count from the synovium, but also blocks the detector by greatly increasing the dead time.

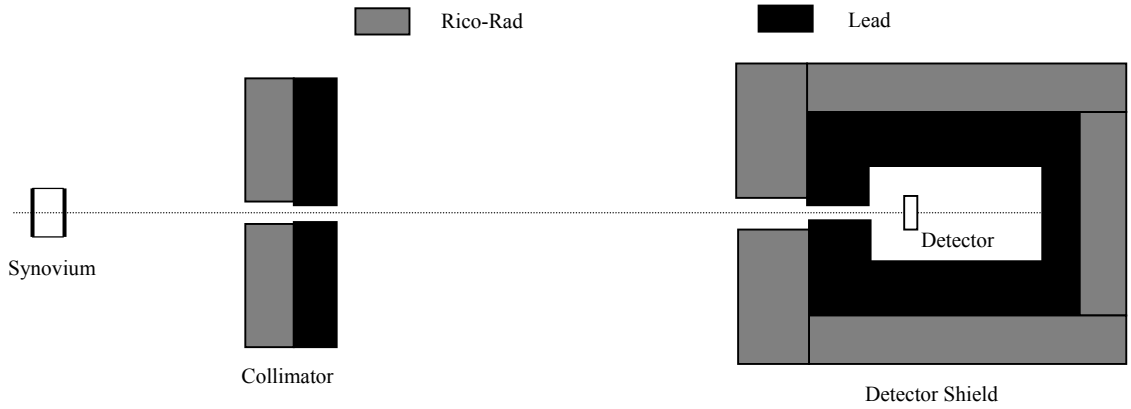

Figure 4.1 Schematic of the telescope system including photon detector, collimator for limiting the view angle of the detector to the synovium, and detector shield for reducing background counts and detector damage caused by fast neutrons.

A schematic of the telescope system, including the photon detector, the collimator and the detector shield, appears in Figure 4.1. The collimator consists of two layers. The front layer, used for neutron shielding, is made of boronated polyethylene, the same material as is used in the shielding wall (another name for this material is *Rico-Rad*); the second layer is lead, which is used for photon attenuation. The detector shield is composed of an outer layer of Rico-Rad and an inner layer of lead. Suitable thicknesses of Rico-Rad and lead in the collimator and the shield, and the diameter of the aperture in the collimator will be investigated in the following sections in this chapter.

The weight fraction of hydrogen in Rico-Rad is 12.05%, higher than that in water (11.11%). Therefore, Rico-Rad is very effective in fast neutron moderation and thermal neutron absorption. A potential drawback of using it as the neutron shielding material in the collimator and the shield is that boron photons can also be generated in it. On the other hand, in the collimator and the shield, a layer of lead is behind the Rico-Rad layer. Therefore, the majority of the boron photons generated in Rico-Rad will be stopped in lead, and the influence of these photons on synovial boron photon detection will be reduced.

The diameter of the aperture in the collimator determines the viewing region of the synovium by the detector. Fewer background neutrons and photons will be counted when using a smaller viewing region. On the other hand, the aperture cannot be so small that the signal collection time during joint irradiation is too long. The optimal diameter, which is dependent on the dimensions of the synovium, will balance the SNR and the boron photon count rate.

4.1.2 Viewing region of the detector and photon arrival probability

Figure 4.2 shows the geometry of the synovium and the simplified telescope system after a collimator is added between the synovium and the photon detector. Without the collimator, the detector can "see" the synovium and also its surroundings. The collimator confines the viewing region of the detector to a narrow cone. The most important parameters associated with the collimator are the distance between the collimator and the synovium l, and the radius of the aperture in the collimator r. Different combinations of the two parameters will produce various sizes of viewing region of the detector. In the final telescope system, the size of the detector is fixed (denoted as the radius a in Figure 4.2). The other parameters, such as the distances l and L (the distance from the synovium to the detector), the radius of the aperture in collimator r, the thickness of the collimator d, are changeable. An optimization process will be conducted to find a combination of parameters that yields acceptable performance of the system.

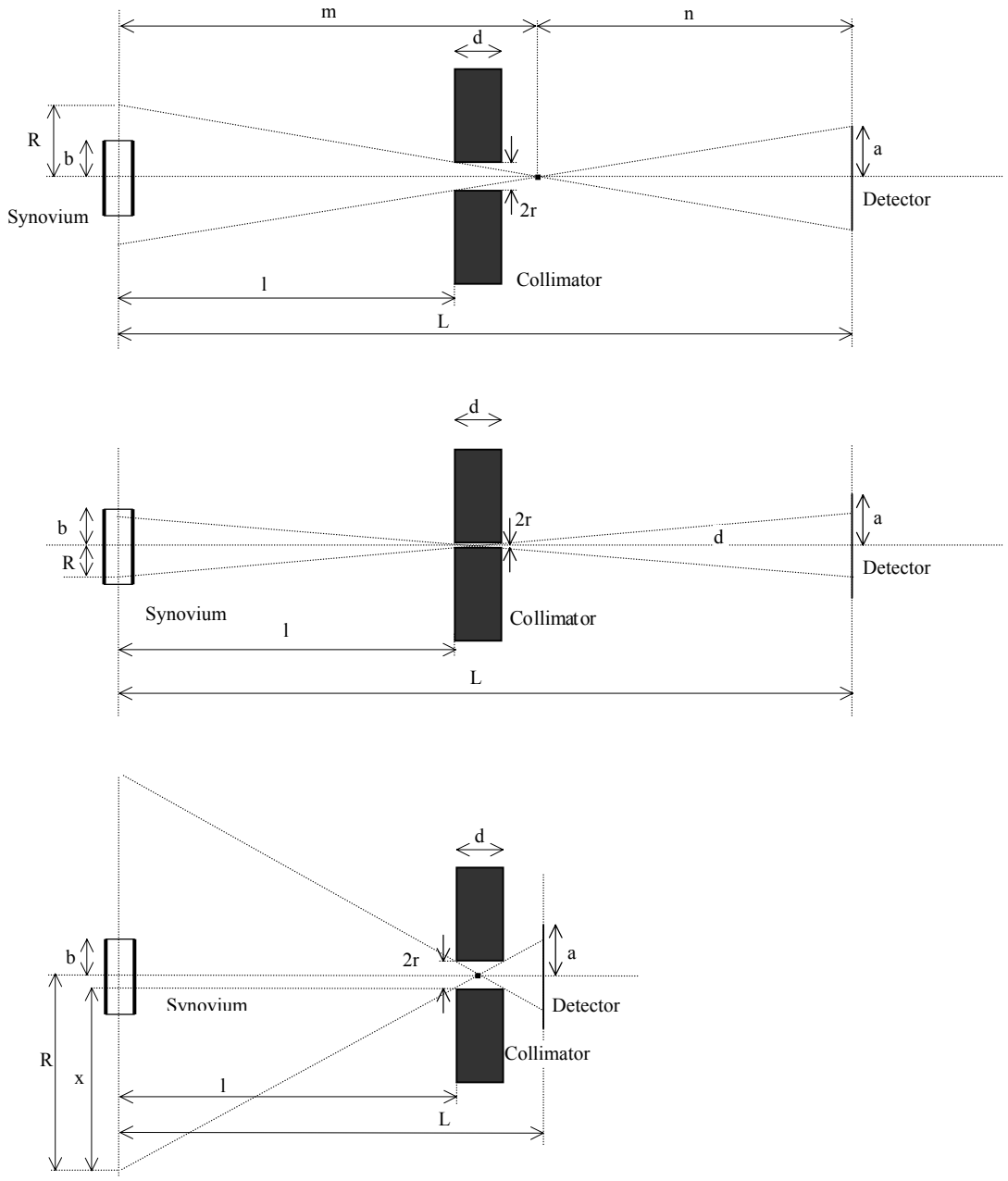

Figure 4.2 Illustration of the viewing field of the detector (R) to the synovium after a collimator is positioned between the synovium and the detector. In case (a), the entire detector surface receives boron photons from the synovium; in case (b) and (c), a part of the detector surface is not used for boron photon detection, either because the aperture in the collimator is too small (case (b)) or the detector is too close to the collimator (case (c)).

The deduction of the mathematical relation of the viewing region, represented by radius *R*, is based on Figure 4.2. There are two possible cases. In case one (Figure 4.2 (a)), the synovium is visible to each point on the detector surface; in case two, either because the aperture in the collimator is too small (Figure

4.2 (b)), or because the detector is too close to the collimator (Figure 4.c (c)), the synovium is visible to only a portion of the detector surface. In case one, the radius R of the detector viewing region at the location of the synovium can be calculated with the following three relations (see Figure 4.2 (a)):

$$\begin{cases} m+n=L \\ \dfrac{R}{m}=\dfrac{a}{n} \\ \dfrac{R}{r}=\dfrac{m}{m-l} \end{cases},$$

where m and n are defined in Figure 4.2 (a).

The solution is $R=\dfrac{a\cdot l+r\cdot L}{L-l}$.

In case two, the radius R is determined by the following two equations:

$$\begin{cases} R=x+r \\ \dfrac{x}{l}=\dfrac{2r}{d} \end{cases}.$$

The solution is $R= x + r = r\cdot(\dfrac{2l}{d}+1)$.

The radius of the viewing region is the smaller one of the two Rs above, i.e., R = min $(\dfrac{a\cdot l+r\cdot L}{L-l}, r\cdot(\dfrac{2l}{d}+1))$.

The viewing region, centered at the symmetrical center of the synovium (point O in Figure 4.3), has a total area of $\pi\cdot R^2$. Photons originating at different parts in the viewing region have different probabilities of arriving at the detector. Since the photon emission is isotropic, the probability equals the projection area of this point on the detector surface divided by $4\cdot\pi\cdot L^2$. The collimator determines this projection area of each point in the viewing region. The center of the viewing region O has the largest projection area, thus a photon generated there has the maximum probability of reaching the detector surface; on the other hand, the projection area of the points at the edge of the viewing region or outside it is zero, and ideally any photon generated there has no chance of being detected by the detector. This fact is illustrated in Figure 4.3(a) (see the difference for point O and O′). The projection area of the point O at the detector surface is $\pi\cdot(\dfrac{L}{l+d}\cdot r)^2$ (less than $\pi\cdot a^2$, the surface area of the detector) in this specific example, and the probability for a photon to strike the detector is $\pi\cdot(\dfrac{L}{l+d}\cdot r)^2/(4\cdot\pi\cdot L^2) = \dfrac{1}{4}(\dfrac{r}{l+d})^2$. This probability is fully dependent on the parameters of the collimator (location l, thickness d, the aperture radius r), and is not related to the location of the detector L. This demonstrates the crucial status of the collimator again.

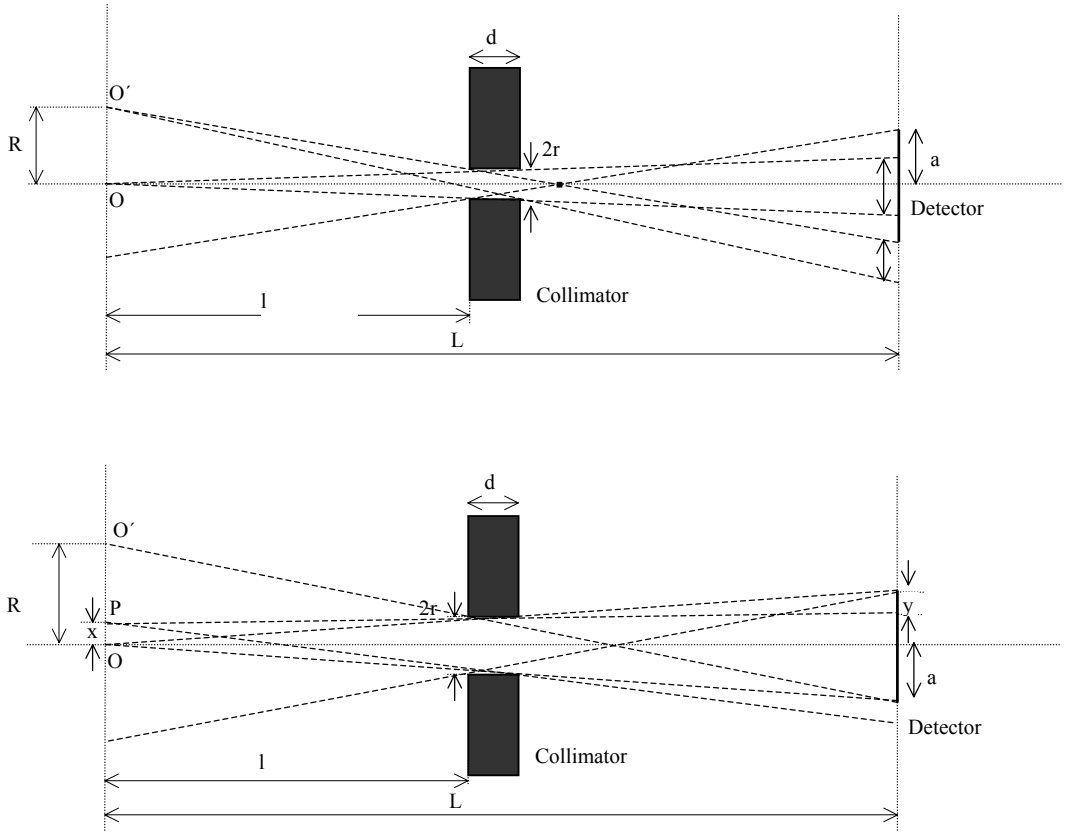

Figure 4.3 (a) illustrates a fact that photons emitted at different regions in the detector viewing region have different probabilities of arriving at the detector. Photons at point O have the largest probability, and photons at O′ have zero probability. (b) shows a special case: (l+d)/L=r/a . The projection area on the detector surface for any point P off point O is less than the projection area for point O, which is πa^2.

A curve depicting the arrival probability from point O ($x = 0$) to point O′ ($x = R$) is plotted in Figure 4.4 for the example in Figure 4.3 (a). The photon arrival probability drops from $\frac{1}{4}(\frac{r}{l+d})^2$ at point O to zero at O′. The probability curve shows a flat top, and the formation of which will be explained later. Figure 4.4 plots a linear probability descending from the transition point O′′ (probability is still $\frac{1}{4}(\frac{r}{l+d})^2$) to O′(probability is zero). However, the actual process is nonlinear, and the analytical expression is quite complicated.

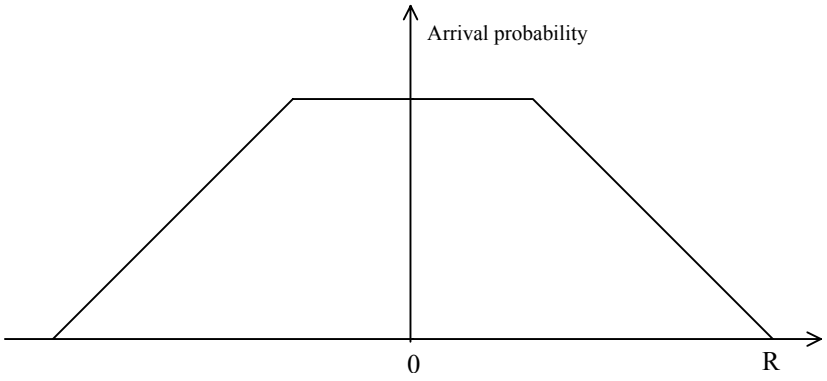

Figure 4.4 Schematic of the photon arrival probability curve.

Figure 4.3 (b) illustrates a special case, in which the condition $\frac{l+d}{L}=\frac{r}{a}$ is satisfied. Under this condition, point O exactly sees the whole detector surface ($\pi \cdot a^2$). In other words, the projection area of point O overlaps exactly with the detector surface. However, for any other points, the projection area is less than $\pi \cdot a^2$ (see Figure 4.3 (b), where any deviation from point O causes a fraction of the projection area to move out of the detector surface). A direct consequence is that there is no longer a flat top to the photon arrival probability curve. The analytical expression of the arrival probability for the case in Figure 4.3(b) was also deducted (the deduction process is lengthy and is not given here). For a point with a distance x from O (Figure 4.3 (b)), the photon arrival probability is approximated as

$$\left[2 \cdot a^2 \cdot \arcsin\left(\frac{\sqrt{a^2 - y^2/4}}{a}\right) - y \cdot \sqrt{a^2 - y^2/4}\right] / (4 \cdot \pi \cdot L^2),$$

where,

$$y = \begin{cases} 0 x = 0 \\ \dfrac{L-(l+d)}{l+d} \cdot x 0 < x \le r \\ a - r + \dfrac{L-l}{l}(x-r) r < x \le R \end{cases} .$$

The validity of this expression requires $R << L$, which is always true in a practical telescope system. It is easy to verify that when $x = 0$, the probability equals $\pi \cdot a^2/(4 \cdot \pi \cdot L^2)$, and when $x = R$ ($y = 2a$), the probability is zero. The non-linear response of the arrival probability with x is apparent in the above equation. The expression of y changes when x moves from $x < r$ to $x > r$, and the underlying reason is that the thickness of the collimator d cannot be omitted ($d/l << 1$ is not satisfied).

If $\frac{l+d}{L}=\frac{r}{a}$ is not met, the projection area of point O on the detector plane will not match exactly the area of the detector surface. If $\frac{l+d}{L}>\frac{r}{a}$, the projection area of point O is $\pi\cdot(\frac{L}{l+d}\cdot r)^2$, which is less than the detector surface area $\pi\cdot a^2$. If $\frac{l+d}{L}<\frac{r}{a}$, the projection area of point O is $\pi\cdot a^2$ ($\pi\cdot(\frac{L}{l+d}\cdot r)^2$ is larger than the detector surface area, and therefore the effective area is $\pi\cdot a^2$). For either case, there will be a top flat in the photon arrival probability curve, the maximum probability (at point O) for the two cases is $\frac{1}{4}(\frac{r}{l+d})^2$ and $\frac{1}{4}(\frac{a}{L})^2$, respectively.

The length of the top flat is also dependent on the relation between $\frac{l+d}{L}$ and $\frac{r}{a}$. If $\frac{l+d}{L}=\frac{r}{a}$ is satisfied, the length is zero. If $\frac{l+d}{L}>\frac{r}{a}$, the flat length is *r*. If $\frac{l+d}{L}<\frac{r}{a}$, the situation is a little complicated: if *a*>*r*, the flat length is $r-\frac{l+d}{L-l}(a-r)$, which is less than *r*; if *a*<*r*, the flat length is $r+\frac{l}{L-l}(r-a)$, which is larger than *r*.

Until now, only the function of the collimator in determining the size of the viewing field has been considered. However, it is clear from Figure 4.1 that the front portion of the detector shield also serves as a collimator. The aperture in the detector shield also limits the viewing region of the detector, and affects the curve of the photon arrival probability by altering the maximum probability and the length of the flat top. However, it is not necessary to repeat the above deduction process to obtain a set of new formulae. There is a simpler way. Imagine that the empty space between the collimator and the detector shield is filled with shielding materials (as illustrated in Figure 4.5), and then the collimator and the shield are both parts of a new collimator. The thickness of this new collimator *d′* is the sum of the thickness of the original collimator *d*, the distance from the rear surface of the collimator to the front surface of the shield l_{cd}, and the thickness of the shielding materials in front of the detector d_s. In this way, the above equations will be still valid after the detector shield is included, and the only difference is *d* has to be replaced with *d′*.

In conclusion, for a telescope system illustrated in Figure 4.1, the radius of the detector viewing region at the synovium is $R = \min\left(\frac{a\cdot l+r\cdot L}{L-l}, r\cdot(\frac{2l}{d'}+1)\right)$. Photons emitted at different locations inside the viewing region have different probabilities of arriving at the detector. If the relation $\frac{l+d'}{L}=\frac{r}{a}$ is satisfied,

no flat top appears in the photon arrival probability curve, and the maximum probability is $\frac{1}{4}(\frac{a}{L})^2$ of detection. If the relation $\frac{l+d'}{L}=\frac{r}{a}$ does not hold, a flat top appears. If $\frac{l+d'}{L}$ is larger than $\frac{r}{a}$, the length of the flat top is *r* and the maximum probability is $\frac{1}{4}(\frac{r}{l+d'})^2$ ($<\frac{1}{4}(\frac{a}{L})^2$). If $\frac{l+d'}{L}$ is less than $\frac{r}{a}$, the length of the flat top is $r-\frac{l+d'}{L-l}(a-r)$ (if $a>r$) or $\frac{l}{L-l}(r-a)+r$ (if $a<r$), and the maximum probability is $\frac{1}{4}(\frac{a}{L})^2$.

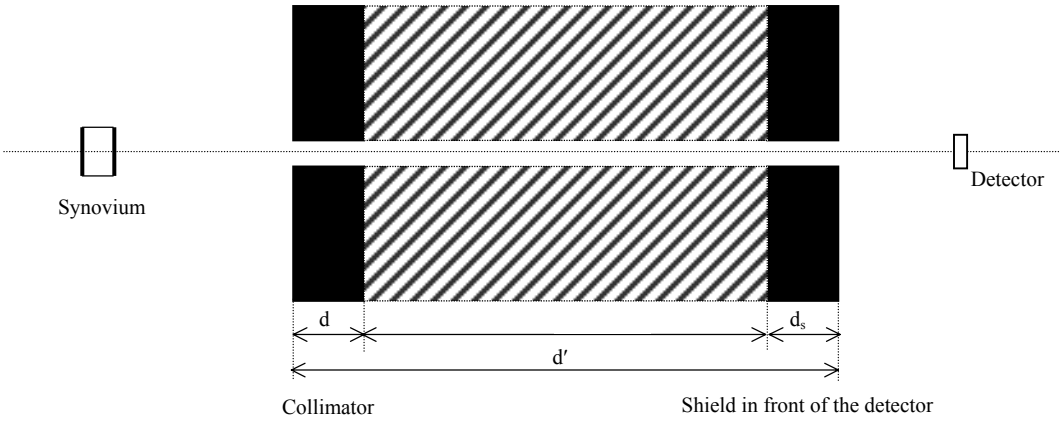

Figure 4.5 A plot showing that after the detector shield is in position, the formula of the detector viewing region derived for cases in Figures 4.2 and 4.3 is still valid if the empty space between the collimator and the detector shield is imagined to be filled with shielding material and d is replaced with d′.

In the deductions and discussions above, the collimator was assumed to function ideally: no particles can penetrate through it, and no particles are scattered to the detector from it. If these possibilities are taken into account, more particles enter the detector than predicted by the photon arrival probability.

4.1.3 Selection of the parameter *l*

Compared to the geometrical dimensions of the BNCS facility[6] and the telescope system under development, the synovium is very small in size (6 cm in length, 3 cm in radius and 0.15 cm in thickness in the simulation model). The whole synovium is visible to the detector if the radius *R* of the detector viewing field is larger than $3\sqrt{2}$ = 4.24 cm. It is not reasonable to choose a value of *R* much larger than 4.24 cm, and its value should be close to 4.24 cm or smaller than that for the purpose of background count reduction.

The prescribed value of *R* is obtained by adjusting the values of *l* and *r*, two primary parameters of the collimator. There could be countless combinations of *l* and *r* for a specific value of *R*. However, there are other considerations in choosing the parameters. An important issue in installing the telescope is

alignment. That is, the symmetrical axis of the aperture has to pass through the centers of the synovium and the front surface of the detector. It is likely that a satisfying alignment is more easily achievable for a larger collimator aperture. In general, when the aperture in the collimator is enlarged (r goes up), the distance l has to go down to keep R constant. Therefore, the collimator should be located as close to the synovium as possible. However, if the collimator is too close to the patient, the dose delivered to the patient will be changed as a result of scattering reactions in the collimator. Therefore, l should be large enough not to interfere with the therapy process. In BNCS, a value of 50 cm might be reasonable for l. In the simulations in this chapter, this value of l is evaluated.

4.1.4 Thickness of boronated polyethylene and lead in collimator

The simple guide to determining the thickness of Rico-Rad (boronated polyethylene) in the collimator and detector shield is to find that thickness for which additional increases in thickness will not further improve the shielding of neutrons. However, this thickness is difficult to determine via Monte Carlo simulations because of the computational inefficiency in deep-shielding problems. A simple test was therefore performed to assist in thickness selection of boronated polyethylene.

As illustrated in Figure 4.6, a layer of Rico-Rad was positioned in the direction of (90°, 270°) and at 50 cm from the synovium. Five point detectors were located at five different positions just behind the Rico-Rad, with 10 cm between each detector. The hole in the Rico-Rad is 5 cm in diameter. In simulations, the thickness of Rico-Rad was increased from 5 cm to 25 cm, with a step of 5 cm each time.

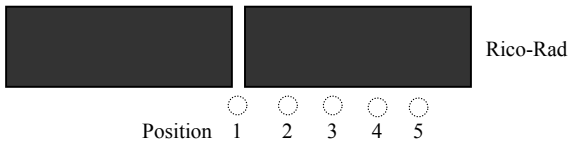

Figure 4.6 Configuration for investigating the effectiveness of Rico-Rad in neutron shielding.

Simulation results indicate that at all five positions, the neutron flux decreases as the thickness of Rico-Rad increases. The neutron flux at position 1 is the highest among the five positions. At this position, the total neutron flux behind 25 cm of Rico-Rad (7.34×10^{-7} /cm^2/neutron source) is 0.18 of that behind 5 cm of Rico-Rad (4.14×10^{-6} /cm^2/neutron source). The neutron flux at position 1 includes the contribution from neutrons directly passing through the aperture and from those penetrating through the shielding. However, at the other four positions, only shielding penetration is involved. Along the path from position 2 to position 5, the neutron flux continues to drop. When the thickness of Rico-Rad is 5cm, the neutron flux at position 5 is one order of magnitude less than that at position 1. This difference jumps to two orders of magnitude when the thickness of polyethylene reaches 25 cm. The simulation results

supply information on the efficacy of Rico-Rad in neutron shielding: 5 cm of this material is enough to stop most of the thermal neutrons; however, it may take approximate 20 cm to reduce the fast neutron flux by one order of magnitude. The simulation results only provide a guide in selecting the initial thickness of Rico-Rad, and the appropriate thickness will be ultimately determined via experimentation.

The thickness of lead is relatively simple to determine. The linear attenuation coefficient of 478 keV and 2223 keV photons in lead is 2.01 cm^{-1} and 0.514 cm^{-1}, respectively. After taking into account the build-up factor (~4.4 for 2223 keV photons and < 5 for 478 keV photons), 20 cm of lead can stop almost all of the 478 keV photons (17 to 18 orders of magnitude) and attenuate the hydrogen photons by 4 orders of magnitude.

The thickness of Rico-Rad and lead is chosen to be 20 cm both in the collimator and in the detector shield. Therefore, on the way from the synovium to the photon detector, the total thickness of Rico-Rad and lead is both 40 cm. It is expected that the probability of a boron or hydrogen photon penetrating the lead layers is negligible, and that the neutrons from the beam direction will be attenuated by 3 to 4 orders of magnitude.

4.2 Choice of suitable location of the detector

The advantages of positioning the photon detector in region III or IV have already been pointed out. The candidate directions (all directions in regions III and IV) include (θ,φ)= (90°, 225°), (90°, 270°), (90°, 315°), (45°, 225°), (45°, 270°), and (45°, 315°). However, after the distance l is fixed at 50 cm, it is impossible to put the collimator in the two directions with φ = 315°. Since, the collimator will touch the torso of the anthropomorphic phantom. It is also impossible for the direction (45°, 225°) because the collimator would physically interfere with the shielding wall. Therefore, only three directions ((90°, 225°), (90°, 270°), and (45°, 270°)) need to be examined. The distance of the detector from the synovium, L, should be approximately 200 cm (section 3.5). Four values of L will be tested: 150 cm, 175 cm, 200 cm, and 225cm (225 cm is close to the largest distance allowable in the therapy room after enough space is reserved for positioning of the shielding materials between the detector and the wall.). So there are altogether 12 positions (three directions × four distances) to be explored. To compare the positions at different Ls, the viewing region of the detector is kept the same under the four values of L, and thus the size of the aperture in the collimator has to be adjusted as L changes. Two values of R (radius of the viewing region) are chosen: 4.30 cm and 3.05 cm. At the first value of R, the whole synovium is visible to the detector; at the second value, the photon detector can see a large part of the synovium but not its entirety. The details are illustrated in Figure 4.7. The values of radius r under the eight combinations of Ls and Rs are listed in Table 4.1.

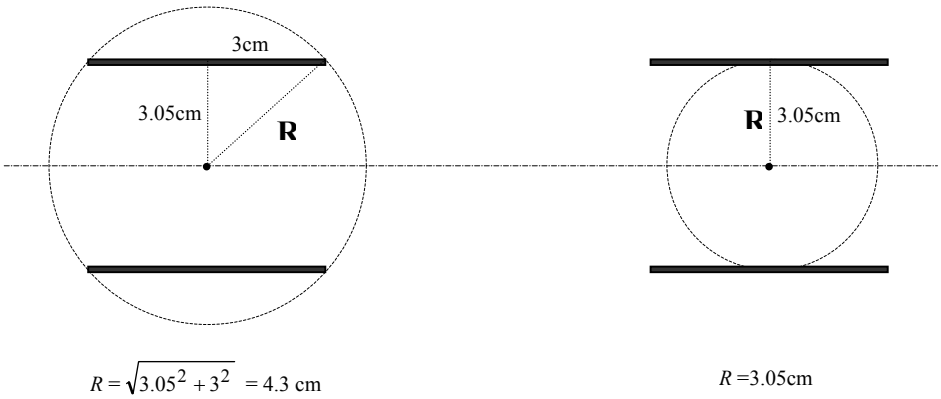

Figure 4.7 2D slice of the synovium showing: if R = 4.3 cm, the entire synovium is visible to the detector (the entire synovium is inside the detector viewing field represented with a circle with a radius R); on the other hand, if R = 3.05 cm, a part of the synovium is outside the viewing field of the detector.

Table 4.1 Radius of the aperture in the collimator under various combinations of distance L and radius R

L (cm)	r (cm) (R = 4.3 cm)	r (cm) (R = 3.05 cm)
150	2.035	1.445
175	2.355	1.631
200	2.600	1.780
225	2.790	1.900

The synovial boron concentration was modeled as either 0 ppm or 10,000 ppm. The results with no boron in the synovium will be compared with the results presented in the last chapter, before the collimator and the detector shield were added. Consequently, the effectiveness of the collimator and the shield in reducing the neutron and photon backgrounds can be determined. The difference in number of boron photon counts at 0 ppm and 10,000 ppm will show the influence of the boron compound in the synovium, which is one of the most important factors in judging the feasibility of the telescope system.

A hole of 7 cm in diameter is opened in the graphite back reflector along the direction from the synovium to the detector to avoid the attenuation of synovial boron photons from the synovium in the reflector.

4.2.1 Comparison at a detector location before and after shielding and collimation

The position of (r, θ, φ) = (200 cm, 90°, 270°) was selected to explore the effectiveness of the collimation and shielding in background reduction. The neutron and photon fluxes at this position are listed in Table 4.2. After collimation and shielding, the neutron flux, the 511 keV photon flux, and the 2223 keV photon flux are decreased by one order of magnitude. The decrease in the boron photon flux reaches two orders of magnitude. Without collimation and shielding, detection of the boron photons from

the synovium above background is very difficult since the boron photon flux from the synovium at 10,000 ppm is one order of magnitude lower than that from the shielding wall.

Table 4.2 Particle flux before and after collimation and shielding

Particle	Particle flux (/cm^2/source neutron)		
	Before collimation and shielding	After collimation and shileding	
		R = 4.3 cm	R = 3.05 cm
Neutron	4.5 e-7	6.2 e-8	3.8 e-8
511 keV photon	2.0 e-9	3.7 e-10	1.3 e-10
hydrogen photon	2.0 e-8	1.5 e-9	5.1 e-10
boron photon (0 ppm)	9.5 e-8	2.2 e-10	1.3 e-10
boron photon (10,000 ppm)	N/A	6.0 e-9	2.6 e-9

Figure 4.8 (b) shows the photon flux spectra at this location for the four combinations of two R values and two boron concentrations, and the photon flux spectrum before collimation and shielding is presented in Figure 4.8 (a) (the same as Figure 3.9). In Figure 4.8 (a), the most prominent feature in the photon spectrum is the 478 keV peak, which is formed by the boron photons produced in the boron-containing shielding wall. However, after the collimator and the shield are added, this background boron peak is almost extinguished, and is much weaker than the neighboring 511 keV annihilation peak. The background boron photon flux drops from 9.5×10^{-8} /cm^2/neutron source to 1.8×10^{-10} /cm^2/neutron source (R = 4.3 cm), a decrease of 99.8%. The remaining boron photons originate from boronated polyethylene in the collimator and the shield, which was confirmed by the finding that the boron peak completely disappears if boronated polyethylene in the collimator and the shield is replaced with lithiated polyethylene. Thus, with the aid of collimation and shielding, the contribution to the boron photon signal from the shielding wall can be reduced to a negligible level.

The increase in the detected boron photon signal is very apparent after 10,000 ppm of boron concentration is loaded in the synovium. For example, for R= 4.3 cm the boron photon flux at 0 ppm is only 3% of that at 10,000 ppm. If the synovial boron concentration is 1,000 ppm, the boron photon flux from boronated polyethylene represents 14% of the total boron photon flux. Therefore, compared with the boron photon count originating from the synovium, the count of boron photons from boronated polyethylene in the collimator and the detector shield is unimportant. It is imaginable that the majority of the detected boron photons from boronated polyethylene are emitted somewhere close to the aperture. An effective way to further reduce the background boron photon count is to replace those portions of boronated polyethylene surrounding the aperture with polyethylene containing no boron. This will be especially helpful if the synovial boron concentration is low.

With a synovial boron concentration of 10,000 ppm, the 511 keV photon flux is 4.7% of the boron photon flux for both R = 4.3 cm and R = 3.05 cm. This fraction is 7% at 5,000 ppm, and 25% at 1,000 ppm, respectively. Therefore, for most practical boron concentrations, the 511 keV photon flux is at least one order of magnitude lower than the 478 keV photon flux. Another issue to consider is whether or not the 511 keV contribution to the "boron count" can be assumed to be a constant, independent of the synovial boron concentration. If this were the case then a constant value could simply be subtracted from the boron peak and the necessity of utilizing a detector capable of distinguishing the 478 keV peak from the 511 keV peak would be eliminated. At this detector position, the 511 keV photon flux only drops by ~10% after the boron concentration is increased from 0 ppm to 10,000 ppm. (The decrease is also because of less emission of 511 keV photons caused by more neuron captures in the synovium.) Therefore, the 511 keV photon flux is much lower than the 478 keV photon flux and is quite stable under various boron concentrations. From the information available now, the use of a NaI detector is very promising.

A hydrogen peak is apparent in the photon spectrum, and it is the only high-energy photon peak that has a count comparable to the boron peak. If the synovial boron concentration is 10,000 ppm, the 2223 keV photon flux is 21% of that of boron photons at R = 4.3 cm, and 14% at R = 3.05 cm. The boron photon peak sits on the Compton plateau of hydrogen photons, and the impact from the Compton plateau is dependent on the type and effective volume of the photon detector. However, since the hydrogen photon flux is only 1/5 of the boron photon flux, the influence from the Compton plateau is expected to be very small. If the synovial boron concentration is 2,000 ppm, the hydrogen photon flux is about 3/5 of the boron photon flux, and the influence of hydrogen photons on the boron photon peak is still unimportant.

The background count decreases as the aperture in the collimator shrinks. However, the boron photon count decreases faster. The boron photon flux drops over one half (58%) when the radius of the aperture is changed from 2.6 cm (R = 4.3 cm) to 1.78 cm (R = 3.05 cm). In contrast, the decrease in neutron flux and the 511 keV photon flux is 43% and 58%, respectively. Since the photon flux drops faster than the neutron flux when the aperture contracts, there is no advantage in adopting a smaller aperture from the point of view of a better signal to noise ratio if the neutron irradiation is endurable to the photon detector.

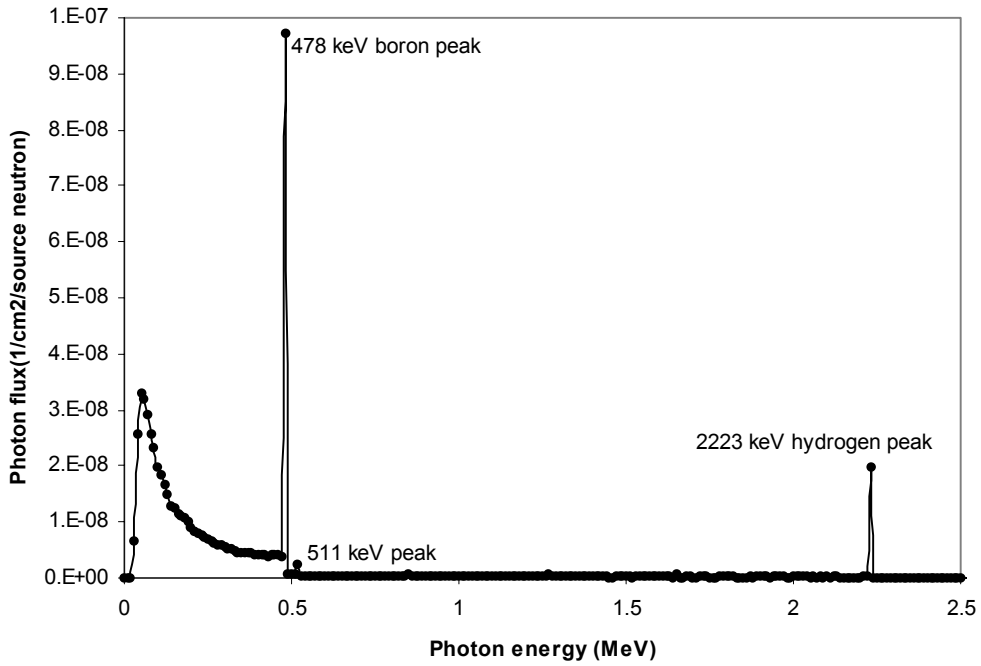

(a)

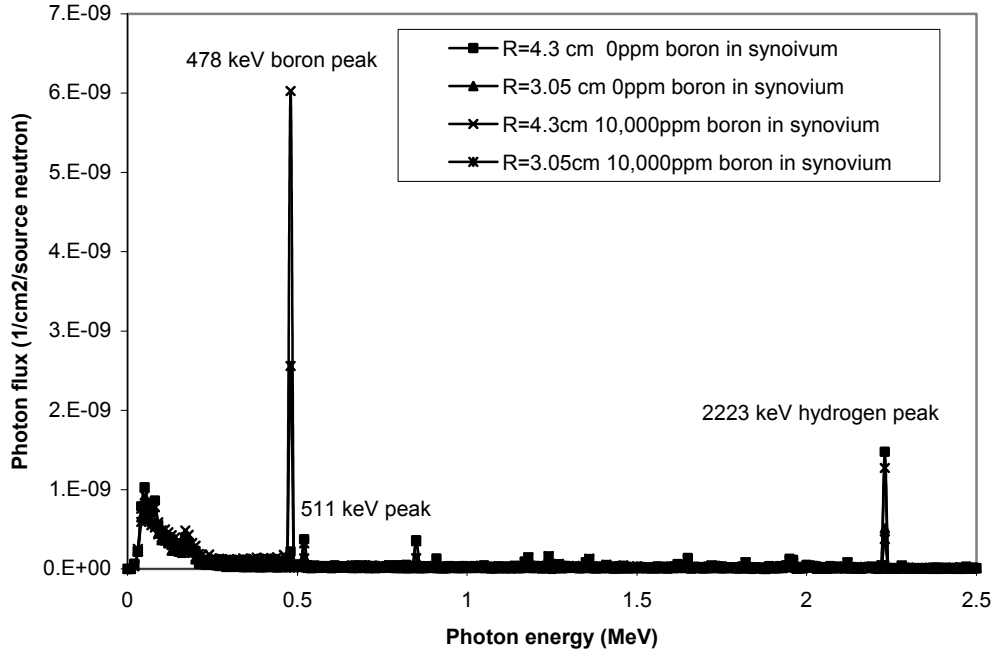

(b)

Figure 4.8 Simulated photon flux spectrum at position (200 cm, 90°, 270°): (a) before collimation and detector shielding (same as Figure 3.9); (b) after the collimation and detector shielding (two sizes of aperture and two boron concentrations).

The application of the detector shielding and collimation reduces the background count and improves the signal to noise ratio significantly. However, there are still neutrons and background photons remaining at this position after shielding. It is worthwhile to investigate where these remaining background particles come from. These particles can either enter the detector via the aperture or penetrate through the shielding to strike the detector. We have already seen that the size of the aperture affects the background count. Here a question arises: if the radius of the aperture is reduced to zero, will the neutron flux go to zero and will all photon peaks be eliminated? Simulations were performed to answer this question, and the results are as follows. With no aperture in the collimator, there are still neutrons arriving at this position. The neutron flux is approximately 1.0×10^{-8} /cm^2/neutron source, compared to 3.8×10^{-8} /cm^2/neutron source for r = 1.78 cm. Therefore, the aperture is the primary entrance of the neutrons; however, there exists the contribution from neutrons penetrating the shield. The 511 keV peak is also identifiable in the spectrum detected when the aperture is eliminated. It is likely that these 511 keV photons are generated in the lead shield surrounding this position since for a 511 keV photon the probability of penetrating through 20 cm of lead is extremely low (10^{-17}-10^{-18}). On the other hand, the 478 keV and 2223 keV hydrogen peaks are completely eliminated, and hence it is concluded that all the 478 keV photons and 2223 keV photons enter the detector through the aperture.

4.2.2 Comparison of various directions and positions

In the previous section, we compared the background counts at a specific location, before and after shielding, and the effectiveness of the shielding was demonstrated. In this section, locations in various directions (θ,φ) and distances L from the synovium are compared. Results of this comparison will be used to choose the final location of the detector.

Several figures of merit are used to conduct quantitative evaluations. The selected figures include the neutron flux (N), the 478 keV photon flux at 10,000 ppm (B), B/N, and B/H. However, these figures are not of equal importance. The first two, i.e., the neutron flux and the boron photon flux, will be more important. As stated previously, the figures B/N and B/H focus on the relative background influence to the boron peak from neutrons and hydrogen photons, respectively. B/N emphasizes the potential background count from neutron-induced prompt and delayed photons generated in the effective volume of the photon detector, and B/H takes into account the Compton plateau of hydrogen photons under the boron peak. The relative importance of these two ratios depends on the type and the size of the detector. However, the larger these ratios, the better the SNR.

The simulated neutron and photon fluxes for the three different directions and two values of *R* are shown in Figures 4.9, 4.10, 4.11 and 4.12. Table 4.3 lists the values of the figures of merit.

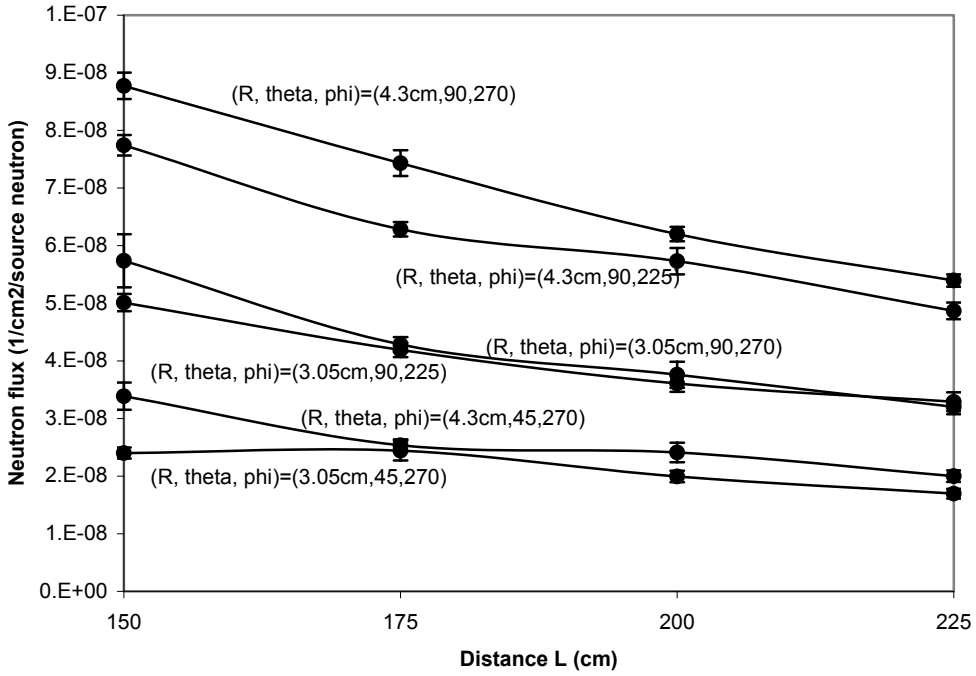

Figure 4.9 Neutron flux at various locations (3 directions and 4 distances) for two sizes of aperture.

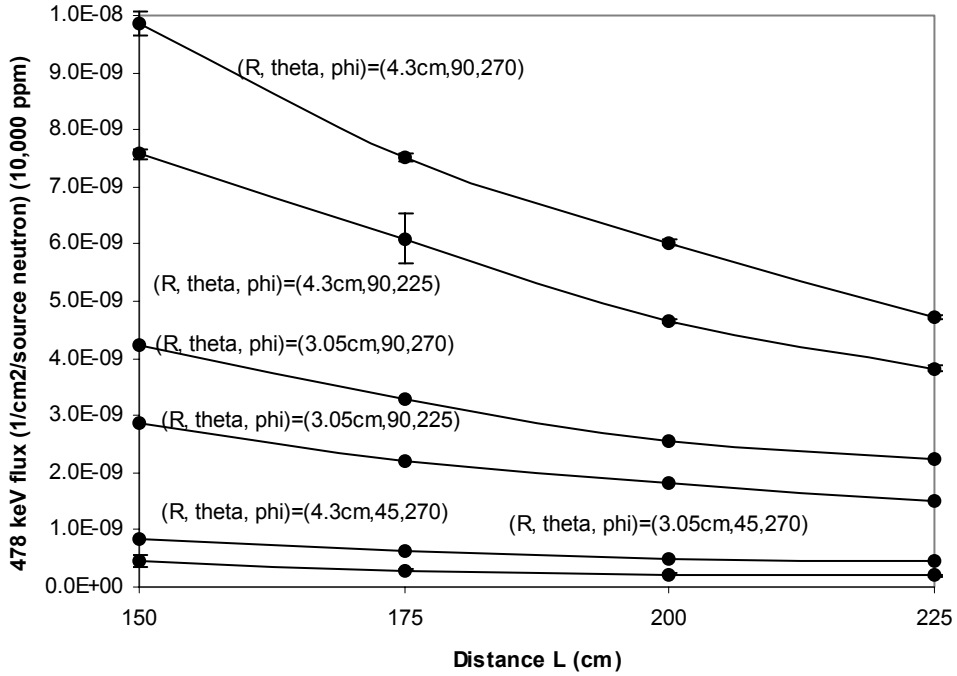

Figure 4.10 478 keV photon flux at various locations (3 directions and 4 distances) for two sizes of aperture.

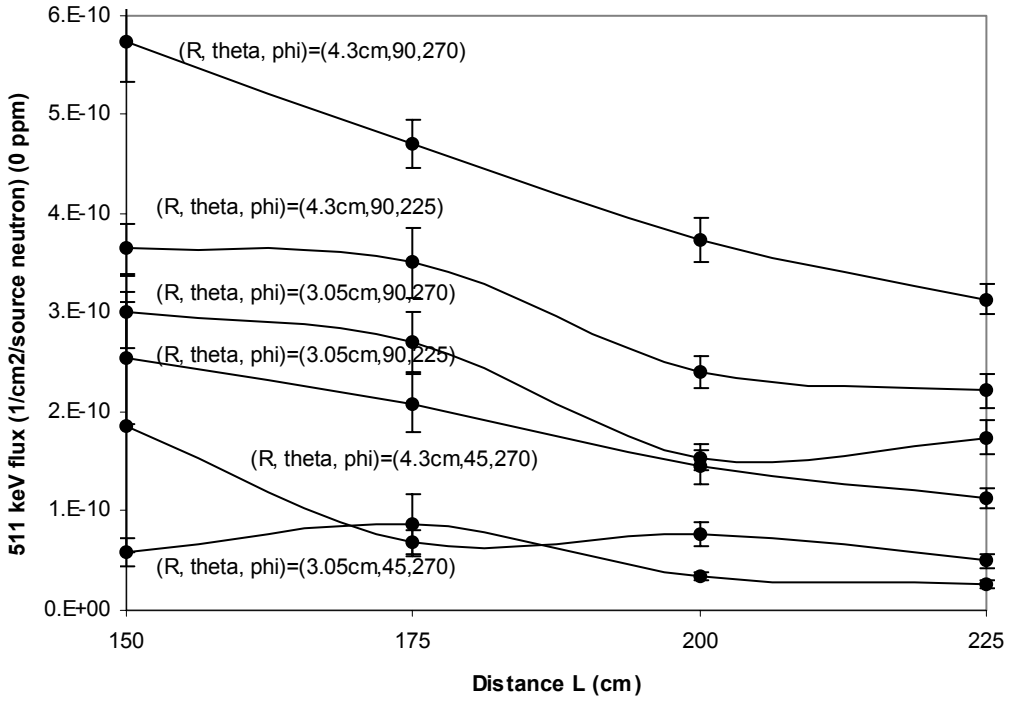

Figure 4.11 511 keV photon flux at various locations (3 directions and 4 distances) for two sizes of aperture.

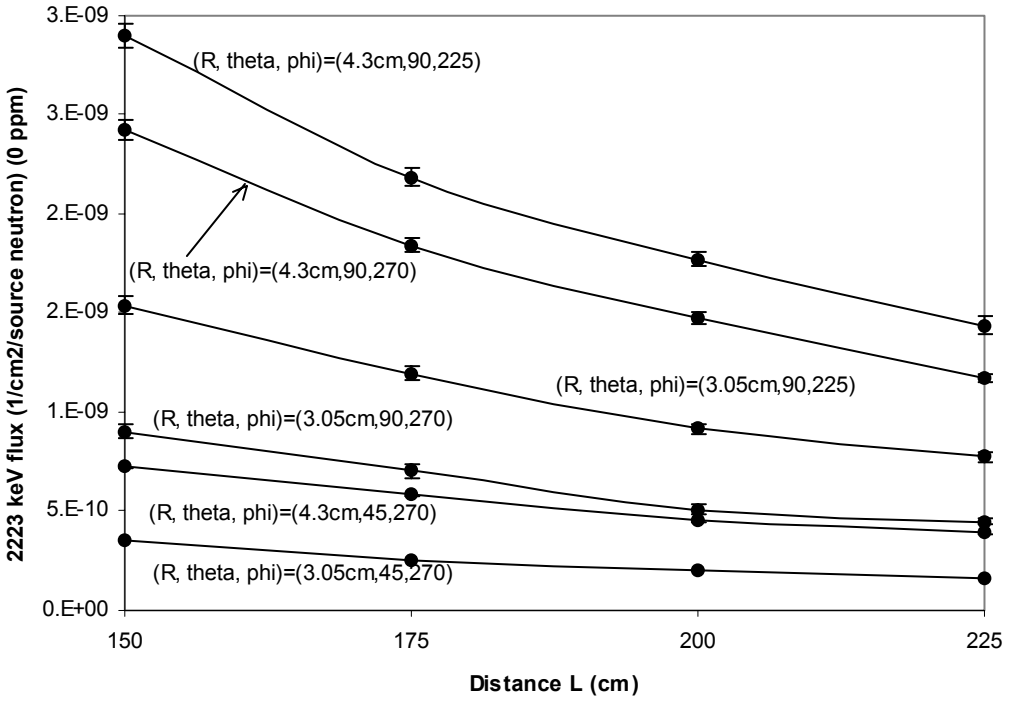

Figure 4.12 2223 keV photon flux at various locations (3 directions and 4 distances) for two sizes of aperture.

Table 4.3 Values of figures of merits for locations in three directions (l=50 cm)

R= 4.3 cm

	(90°, 270°)				(90°, 225°)				(45°, 270°)			
	150 cm	175 cm	200 cm	225 cm	150 cm	175 cm	200 cm	225 cm	150 cm	175 cm	200 cm	225 cm
n flux	8.02e-8	6.31e-8	6.06e-8	4.96e-8	6.87e-8	6.01e-8	4.95e-8	4.50e-8	6.26e-8	5.49e-8	4.60e-8	4.21e-8
B flux	9.86e-9	7.52e-9	6.03e-9	4.72e-9	7.57e-9	6.10e-9	4.66e-9	3.83e-9	8.23e-9	6.59e-9	5.22e-9	4.29e-9
B/n	0.12	0.12	0.10	0.10	0.11	0.10	0.09	0.09	0.13	0.12	0.11	0.10
B/H	4.6	4.3	4.7	4.7	3.0	3.0	3.1	3.1	3.9	4.0	3.9	4.2

R= 3.05 cm

	(90°, 270°)				(90°, 225°)				(45°, 270°)			
	150 cm	175 cm	200 cm	225 cm	150 cm	175 cm	200 cm	225 cm	150 cm	175 cm	200 cm	225 cm
n flux	4.87e-8	4.05e-8	3.44e-8	2.89e-8	4.79e-8	4.08e-8	3.42e-8	3.10e-8	4.32e-8	3.57e-8	3.07e-8	2.68e-8
B flux	4.24e-9	3.30e-9	2.56e-9	2.24e-9	2.88e-9	2.21e-9	1.83e-9	1.50e-9	3.40e-9	2.72e-9	2.22e-9	1.77e-9
B/N	0.09	0.08	0.07	0.08	0.06	0.05	0.05	0.05	0.08	0.08	0.07	0.07
B/H	5.6	5.8	6.8	6.6	2.1	2.1	2.2	2.3	3.1	3.5	3.8	3.8

4.2.2.1 *L* dependence

Despite the fact that the viewing region of the detector is the same for all values of L, all neutron and photon fluxes decrease as L increases. This is expected since the particle arrival probability follows the $1/L^2$ law. If the $1/L^2$ law is strictly satisfied, the fluxes at L= 225 cm should be $(150/225)^2 = 0.44$ of those at L=150 cm, or a decrease of 56%. However, the decrease of the simulated fluxes is slower than the prediction, and is also particle type dependent. Boron photons and hydrogen photons show a flux decrease of around 50%: 50% to 52% for the hydrogen photon flux, and 47% to 52% for the boron photon flux. On the other hand, neutrons and 511 keV photons show a flux decrease of around 40%: 35% to 45% for both the neutron flux and the 511 keV flux. The different flux decrease of the particles is a result of their different origins. Most of the detected hydrogen and boron photons are generated somewhere in or around the synovium, and therefore their decrease approximately follows the $1/L^2$ law. However, the detected neutrons also include those that penetrate the shield (section 4.2.1) and 511 keV photons are generated inside the shielding surrounding the detector.

The L dependence prevails in all three directions and two values of R.

4.2.2.2 *R* dependence(*r* dependence)

The neutron and photon fluxes drop as the detector viewing region decreases. Since this aperture is the primary channel for all particles to reach the detector, it is not surprising that in Figures 4.9 to 4.12 the fluxes of neutrons and photons decrease dramatically as R is reduced from 4.3 cm to 3.05 cm. The R dependence also relies on the type of particle. Again, this dependence is stronger for boron photons and hydrogen photons. The decrease in the neutron flux is 35% to 40%, and is rarely dependent on the direction or L. The loss of 478 keV photons is L independent, and also slightly dependent on the

direction: the drop is 55% to 60% in the two directions with an azimuthal angle φ=270° ((90°, 270°) and (45°, 270°)), and is a little higher (61% to 64%) in the third direction (90°, 225°). The decrease of the hydrogen photon flux is strongly direction dependent: the decrease is 62% to 65% in the direction of (90°, 270°), 45% to 48% in (90°, 225°), and 52% to 57% in (45°, 270°), respectively. The direction dependence of boron photons and hydrogen photons will be covered in detail in section 4.2.2.4. A reliable analysis of 511 keV photons is hard to achieve. The 511 keV photon flux is one to two orders of magnitude lower than the other three fluxes, and it is difficult to get reliable estimations especially for R = 3.05 cm using the MCNP code since the counting efficiency is very low.

4.2.2.3 *l* dependence

In the simulations described above, the distance l was fixed at 50cm from the synovium at all times. Under this l, only three directions among the six directions in regions III and IV are available. In the other directions, the collimator physically interferes with either the torso of the anthropomorphic phantom or the Rico-Rad shielding wall. To include the other three directions ((90°, 315°), (45°, 225°), and (45°, 315°)) in the comparison without shrinking the size of the collimator, the distance l has to be increased. Here, l is doubled to 100 cm. To compare these six directions, it is not necessary to perform all possible combinations of L and R. Instead, one specific case is enough. The chosen values of L and R are 200 cm and 4.3 cm (r = 1.335 cm), respectively. The estimated values of the figures of merit for l = 100 cm are listed in Table 4.4.

Table 4.4 Values of figures of merits for locations in six directions in regions III and IV (l=100 cm)
R= 4.3 cm L=200cm

	(90°, 270°)	(90°, 225°)	(90°, 315°)	(45°, 270°)	(45°, 225°)	(45°, 315°)
n flux	4.43e-8	4.46e-8	3.93e-8	3.96e-8	5.17e-8	4.06e-8
B flux	3.93e-9	2.79e-9	2.82e-9	3.36e-9	2.76e-9	2.56e-9
B/N	0.09	0.06	0.07	0.08	0.05	0.06
B/H	5.0	2.4	2.5	3.8	3.1	2.2

The conclusions drawn from the simulations are as follows. Again, the same viewing region of the detector does not guarantee the same count or flux at the detector surface under different ls. For l=50 cm, the ideal maximum photon arrival probability and the top length of the photon arrival probability curve are 3.91×10^{-5} and 2.63 cm, respectively; however, for l=100 cm, the two values drop to 1.23×10^{-5} and 1.34 cm, respectively. Therefore, although R is not changed, fewer boron photons from the synovium will be detected for l= 100 cm, which is also true for neutrons, 511 keV and 2223 keV photons.

Similar to the R dependence, the loss of 478 keV photons is also slightly direction dependent. The boron photon flux drops by 35% in the directions of (90°, 270°) and (45°, 270°), and is a little higher

(40%) in another direction (90°, 225°). The decrease in hydrogen flux shows the opposite tendency: it drops 22% in the direction (90°, 225°), which is less than the decrease observed in the other two directions (35%-39%). The 10% decrease in the neutron flux is again less than that of photons fluxes, and it is also independent of the direction. The situation for 511 keV photons is not very clear because of the statistical uncertainty associated with this estimate, but the average flux decrease is around 30%, a little lower than the boron and hydrogen photon fluxes. It is difficult to give a quantitative explanation of the above results. The dependence of flux decrease on particle type and direction could be related to the origins of these particles. For example, the detected boron photons are generated in the synovium, but the detected hydrogen photons are more likely emitted from the rest of the tissue and the polyethylene layer in the collimator. The arrival probability for a particle is dependent on its original location, and hence the particle flux and its variation with the parameters of the collimator are dependent on the particle type and the viewing angle of the detector to the synovium.

The dependence of the various fluxes on the parameters of the telescope system L, l and R can be summarized as follows. The particle fluxes can be reduced with increasing L, increasing l, or decreasing R. However, the slope of the reduction with distance is related to the type of particle, and it can also be direction dependent. One important feature is that the neutron flux always drops more slowly than the boron photon flux as a result of the greater tendency for scattering of neutrons compared with photons. Therefore, if the neutron flux is reduced through adjusting any of the three parameters, the B/N figure gets worse. Compared to the neutron flux and the 511 keV photon flux, the boron and hydrogen photon fluxes are more sensitive to the adjustment of the system parameters.

4.2.2.4 Direction dependence

Under the same telescope parameters (l, L and R), the neutron and photon fluxes vary as the direction of the telescope changes relative to the synovium. Since the aperture is the main entrance of these particles, the difference in flux is attributed to the difference in the view from the aperture.

The largest boron photon flux is measured in the direction of (90°, 270°), as shown in Figure 4.10 and Table 4.3. The reasons for this are as follows. Any vector along a direction with an azimuthal angle φ of 270° is normal to the symmetric axis of the synovium (see Figure 3.4). On their way to the detector, the boron photons experience the least attenuation in the direction (90°, 270°) inside the knee joint. The mean free path of 478 keV photons in water is 10.1 cm, which is comparable to the size of a knee joint. Therefore, varying photon attenuation inside the knee joint can cause an appreciable difference in the boron photon count in different directions. This explanation is consistent with the finding in Table 4.4 that the greatest number of boron photons is obtained in the two directions with the azimuthal angle φ

equal to 270° among the six directions. For instance, the boron photon flux in the direction of (90°, 225°) is 20-30% lower than in (90°, 270°), which corresponds to a longer attenuation length of 2.3 to 3.6 cm in water. The count difference between the two directions with the same azimuthal angle φ but a different polar angle θ can be attributed to the different extent of the knee joint in different directions and the heterogeneous production of boron photons in the synovium caused by thermal neutron flux suppression in the joint.

It is difficult to predict the direction in which the lowest neutron flux exists. From Table 4.4, the six directions can be organized into three groups. The direction (45°, 225°) belongs to the first group, and the neutron flux in this direction is over 5×10^{-8} /cm^2/neutron source. The neutron flux of the second group is around 4.5×10^{-8} /cm^2/neutron source, and the two directions (90°, 225°) and (90°, 270°) are in this group. The third group includes three directions ((90°, 315°), (45°, 270°), and (45°, 315°)), and the neutron flux is 4×10^{-8} /cm^2/neutron source, the lowest among the three groups. The difference is around 30% between the highest and the lowest neutron fluxes, which is quite significant. The neutron fluxes in the two directions with an φ angle of 315° are the lowest among the six directions, and those in the directions with an φ angle of 225° are the highest. Therefore, generally the neutron flux decreases as the φ angle increases. That is, the neutron flux in region III is generally lower than that in region IV after the collimator and the shield are put in position. The appreciable difference in neutron flux in different directions is related to the difference in the visible part of the joint to the detector.

For the two figures of merit B/N and B/H, from Table 4.4, the largest values appear in the two directions with an azimuthal angle of 270°. For example, the value of B/N in (90°, 270°) is 30% to 80% larger than that in the four directions with an azimuthal angle unequal to 270°, and the value of B/H in (90°, 270°) is 60% to 120% larger than that in those four directions. Therefore, a better signal to noise ratio is anticipated in these two directions.

4.2.2.5 Choice of detector location

From the results of the simulations, there is not a single location for which all four figures of merit are optimized. However, the two directions (90°, 270°) and (45°, 270°) have more advantages than others. A photon detector in the direction (90°, 270°) takes advantage of the best values for the boron photon count, B/N, and B/H. In another direction (45°, 270°), the neutron flux is the lowest and the values of the other three figures are the second best. Therefore, the φ angle of the best detector location is around 270°.

There are important advantages of positioning the telescope in the plane of θ =90°, which is parallel to the floor: there is enough space for shielding materials, both above and below the photon detector; the

distance from the synovial center to the floor is around 1 meter, and it is not necessary to suspend any part of the collimator and the shield in the air; since the symmetric axis of the aperture is parallel to the floor and the neutron beam axis, it is more convenient to install the shielding units and do the system alignment.

Therefore, after considering the performance of the telescope and its practical implementation, the direction (90°, 270°) is chosen.

4.3 Analysis of the feasibility of a telescope system

The appropriate position of the detector in the therapy room is selected; however, the feasibility of the telescope system has not been confirmed. That is, we still have not determined whether the neutron field at this position is sufficiently low for a photon detector and whether the count rate of boron photons emitted from the synovium is high enough for practical application.

In the previous simulations, the F5 tally (point detector estimator) in MCNP was employed, and hence the collected information was in the form of flux (/cm^2/source particle). Here, the F1 tally (current tally) may be more suitable since the particle count is more directly related to the questions posed above. Unlike the F5 tally, in which the deterministic estimation is already involved, the F1 tally requires the explicit application of powerful variance reduction methods to improve the computational efficiency. The method chosen here is DXTRAN[18]: a DXTRAN sphere surrounds the detector location (200cm, 90°, 270°) so that during each particle collision, regardless of the location of that collision in the therapy room, a fraction of the particle weight is moved onto this sphere. The weight is determined according to the physical probability that the collision would have resulted in a neutron reaching this sphere. Thus, all neutrons contribute to the final tally, and the counting efficiency is greatly enhanced. Inside the DXTRAN sphere, a real detector is not modeled; instead the detector is replaced with a surface representing the front surface of a real detector. A potential issue with the DXTRAN method is that a large dispersion of tally contribution from individual particles could be caused if deep penetration is involved in simulations. Consequently, to speed up the convergence of the tallied results, some simplifications in the simulation model were made. It was assumed that the background contribution from the concrete structure of the radiation room is negligible. Therefore, the ceiling, floor, and walls were removed, and all parts of the detector shield were also removed except for the part in front of the detector. With these simplifications, the neutron fluence at the detector surface will be somewhat underestimated.

A complete analysis of the variation of neutron and photon counts under various boron concentrations was performed. The simulated F1 current spectrum shows similar features to the F5 flux spectrum in Figure 4.8. The counts of thermal neutrons, fast neutrons, and photons of three energies at boron

concentrations of 0 ppm, 2,000 ppm, 5,000 ppm, 10,000 ppm, 15,000 ppm, and 19,000 ppm are tabulated in Table 4.5.

Table 4.5 Number of neutrons and photons arriving at the detector surface under various synovial boron concentrations (l=50 cm, R= 4.3 cm, L=200 cm, (90°, 270°))

Boron Concentration (ppm)	Neutron count (/cm^2/source neutron)		Photon count (/cm^2/source neutron)		
	Thermal (<1eV)	Fast (> 1eV)	478 keV	511 keV	2223 keV
0	5.2 e-7	5.4 e-7	3.8 e-9	6.3 e-9	2.8 e-8
2,000	4.4 e-7	5.2 e-7	4.0 e-8	6.4 e-9	2.8 e-8
5,000	3.9 e-7	5.4 e-7	7.5 e-8	6.4 e-9	2.5 e-8
10,000	3.5 e-7	5.4 e-7	1.1 e-7	5.7 e-9	2.5 e-8
15,000	3.2 e-7	5.2 e-7	1.3 e-7	5.7 e-9	2.4 e-8
19,000	3.1 e-7	5.4 e-7	1.4 e-7	5.7 e-9	2.3 e-8

4.3.1 Neutron count

There are more neutrons arriving at the detector than 478 keV, 511 keV or 2223 keV photons. For example, at 10,000 ppm, the neutron count is 8 times, 36 times, and two orders of magnitude higher than that of 478 keV photons, hydrogen photons and 511 keV photons, respectively.

The neutron count is boron concentration dependent. With an increase in the synovial boron concentration, the neutron count at the detector surface decreases. Compared to that at 0 ppm, the neutron count drops 12% at 5,000 ppm, 17% at 10,000 ppm and 20% at 15,000 ppm. As shown in Table 4.5, the lost neutrons are all thermal neutrons (<1eV); the decrease in the fast neutron count is negligible. The explanation of this phenomenon is that the lost thermal neutrons are absorbed by ^{10}B in the synovium: at a higher boron concentration, more thermal neutrons are captured in the synovium and therefore the number of thermal neutrons reaching the detector decreases. In contrast, there is very little absorption of fast neutrons in the synovium, and so the fast neutron count is unaffected by changing the amount of boron in the synovium. Thermal neutron captures inside the photon detector are followed by emission of prompt and/or delayed photons. (More details of interactions in the detector are provided in Chapter 6.) Since the number of thermal neutrons is several times to one order of magnitude higher than that of 478 keV photons, an appreciable decrease in the neutron count could affect the detection of 478 keV photons by varying the background photon contribution from neutron induced photons to the 478 keV boron peak. However, since only thermal neutrons are influenced, a piece of thermal neutron absorber (such as lithiated polyethylene) put directly in front of the detector will solve the problem by absorbing all thermal neutrons (as will be discussed in section 4.3.5).

One issue with neutron bombardment of the photon detector is detector damage, primarily caused by fast neutrons. NaI detectors are generally very resistant to neutron irradiation, but germanium detectors will show signs of energy resolution degradation after exposure to an excessive number of fast neutrons.

In addition to the operating temperature and the fabricating germanium material (p–type or n-type), the neutron radiation damage in HPGe detectors is also dependent on the efficiency of the detector[14,17]. A detector with a higher detection efficiency is more sensitive to radiation damage. For example, for the GMX series of coaxial HPGe detectors by ORTEC[17], the threshold fluence is 4×10^9 /cm^2 for detectors up to 30% in efficiency, and 1×10^9 /cm^2 for detectors up to 70% in efficiency.

A rough estimation was done to investigate the possibility of the use of an HPGe detector. For this estimate the threshold fluence for detector damage is assumed to be 1×10^9 fast neutrons/cm^2. The fast neutron count is 5×10^{-7}/source neutron at the detector surface (one half of the neutron fluence at 0 ppm), the radius of the detector surface is 2.5 cm, and the neutron yield for the Be(d,n) reaction is 1.67×10^{13}/(minute·mA). Therefore, on average, the neutron fluence at the detector surface is roughly $5\times10^{-7}\times1.67\times10^{13}$ /($\pi\times2.5^2$)=4.3×10^6 cm^2/(minute·mA). Therefore, the lifetime of this detector is $10^9/4.3\times10^5$ ~ 40 hours at a beam current of 1 mA before deterioration in energy resolution can be expected. This time is too short for practical therapy applications. Moreover, as described above, the estimate of neutron fluence is lower than the actual value. If the addition neutron contribution induced by the infrastructure of the therapy room and other objects in the therapy room is appreciable, the lifetime of HPGe detectors for this application is even shorter. Therefore, from simulation results, an HPGe detector is not appropriate for telescope system designed for in-room used during BNCS treatments.

4.3.2 Boron photon count

Consistent with the nonlinear relation between the number of $^{10}B(n,\alpha)$ reactions in the synovium and the synovial boron concentration, the boron photon fluence at the detector surface increases nonlinearly with the increase of the synovial boron concentration, as illustrated in Figure 4.13. The rate of increase in the boron photon count per ppm begins to decrease as boron concentration in the synovium increases. Refer to boron photon production in the synovium (section 4.3.6), only 17 per million of the boron photons emitted from the synovium arrive at the detector. Therefore, only a very small fraction of the boron photons emitted from the synovium will be ultimately detected. However, the boron photon count rate is sufficient for the purpose of reliable and prompt determination of the synovial dose. At 10,000 ppm, the boron photon count at the detector surface is 1.13×10^{-7} /(source neutron). The neutron yield is 1.67×10^{13} n/minute·mA, and hence the count rate at the detector surface will be $1.13\times10^{-7}\times1.67\times10^{13}/60 = 3.15\times10^4$ /second·mA. If the intrinsic full energy detection efficiency of the photon detector is assumed to be 50% (the average of the efficiencies of an HPGe detector with 30% relative efficiency and that of a 10.2 cm × 10.2 cm NaI detector), the count rate of the 478 keV boron photons is 1.58×10^4 /second·mA. The statistical error of the boron photon count will be less than 1% in one second of collection time. With

a synovial boron concentration of 2,000 ppm, the full energy count rate is 5580 /second·mA, which is still high enough (2 seconds for a count uncertainty of 1%). Compared to that at Petten, the boron photon count rate for BNCS can be 2 to 3 orders of magnitude higher.

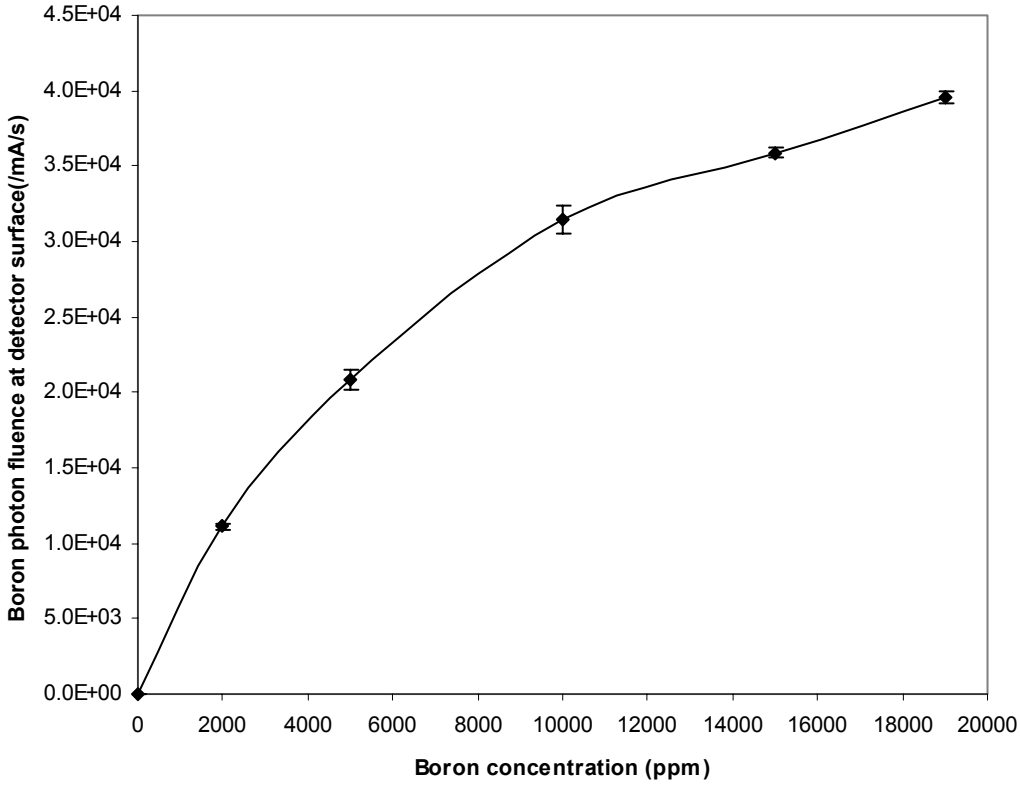

Figure 4.13 Boron photon count rate at the detector surface under various synovial boron concentrations, normalized at 1 mA of beam current.

4.3.3 511 keV annihilation photon count

The count of 511keV photons shows a very slight decrease as the synovial boron concentration increases (~ 10% in the entire range of the synovial boron concentration); however, this decrease cannot be considered statistically important since the uncertainty of the 511 keV photon counts in Table 4.5 is 5 to 10%. The count of 511 keV photons reaches ~10^{-9} per source neutron, which is at least one order of magnitude lower than the boron photon count if the synovial boron concentration is over 2,000 ppm. It is verified again that the 511keV photon count can be assumed to be a constant, and the subtraction of it from the combined peak count of boron photons and 511keV photons will not introduce an appreciable error to the obtained 478 keV photon count. Therefore, distinguishing the 511 keV peak from the boron peak is not necessary, and the use of a NaI detector instead of an HPGe detector is feasible.

4.3.4 Hydrogen photon count

The hydrogen photon count shows a slight dependence on the boron concentration. Compared with that at 0 ppm, the hydrogen photon count drops 8% at 5,000 ppm, 10% at 10,000 ppm and 13% at 15,000 ppm. This decreasing tendency is very likely connected to the neutron flux suppression in the regions around the synovium: at a higher boron concentration, fewer hydrogen photons are produced in the neighborhood of the synovium through the $^{1}H(n,\gamma)$ reaction since the thermal neutron flux in water is reduced by more neutron captures in the synovium.

4.3.5 Lithium polyethylene in front of the detector

The majority of the neutrons striking the photon detector come to the detector from its front side. Therefore, placing a piece of material with a high neutron absorption cross section directly in front of the detector can be helpful to reduce the low-energy neutron flux inside the detector. To avoid a significant loss of 478 keV photons, this piece of material should be thin and mainly composed of light elements. Lithium polyethylene is a good choice because of its low photon yield. The drawback of this approach is that it only works for thermal neutrons because the neutron absorption cross section of ^{6}Li for fast neutrons is rather low.

At Petten, since primarily thermal/epithermal neutrons are involved in therapy, a piece of lithium polyethylene in front of the detector can be extremely helpful in attenuating the neutron current at the detector surface. However, at LABA, fast neutrons with energy up to 6 MeV are included, and this thin piece of lithium polyethylene is transparent to them. On the other hand, since about one half of the neutrons at the detector surface are thermal neutrons with energy less than 1 eV, this piece of lithium polyethylene is still expected to be very effective.

To improve the macroscopic thermal neutron absorption cross section, ^{6}Li enriched lithium polyethylene is used in simulations. The polyethylene contains 7.5% of lithium with ^{6}Li enriched to 93%. The thickness of polyethylene is 5 mm. The mean free path of 0.025 eV thermal neutrons in this polyethylene is 1.7 mm, and therefore 5 mm is enough to absorb most of the thermal neutrons. Simulations confirmed the effectiveness of a thin layer of lithium polyethylene: after positioning this piece of lithium polyethylene, the total neutron current at the detector surface drops from 1.1×10^{-6}/source neutron to 5.6×10^{-7}/source neutron, a decrease of 49%. All neutrons absorbed in polyethylene are those belonging to the thermal region, and there is no effect on neutrons with energy above 1 eV. At the same time, the attenuation of 478 keV photons in 5 mm lithium polyethylene is 5%. Compared to the improvement in neutron reduction, this loss is acceptable.

4.3.6 Function of the side and back graphite reflectors

The function of the side and back graphite reflectors surrounding the knee joint, as mentioned above, is to scatter the escaping neutrons back toward the synovium to increase the synovial boron dose[8]. In Figure 3.4, only the back reflector is visible, and the two side reflectors (one above the joint and another below it) are not seen. The thickness of the reflectors is 10 cm. When setting up the telescope system, a hole has to be opened in one of the reflectors along the path from the synovium to the detector to avoid the loss of 478 keV photons in this specific reflector. In the simulations described above, a 7-cm diameter hole is modeled in the back reflector. In this section, a quantitative evaluation of the effectiveness of the reflectors in increasing the synovial boron dose is pursued, and the influence of the hole in the back reflector on boron photon production in the synovium is also investigated.

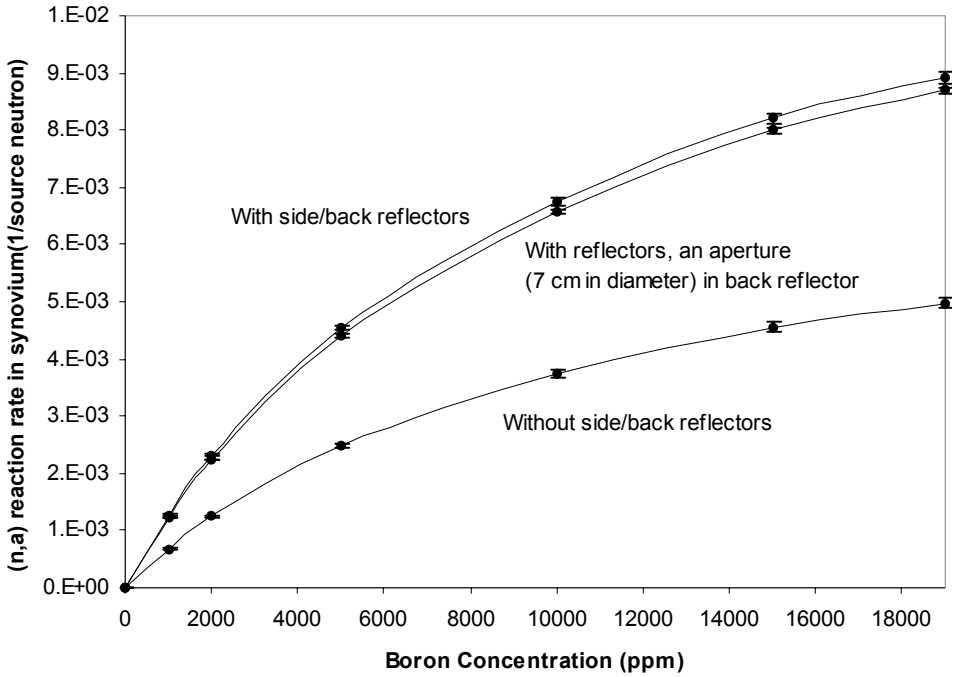

Figure 4.14 Number of (n,α) reactions in the synovium as a function of the synovial boron concentration, with and without the presence of the back/side reflectors and a 7-cm diameter hole in the back reflector.

Figure 4.14 gives the number of $^{10}B(n,\alpha)$ reactions in the synovium (normalized to per source neutron) under various boron concentrations. Data are shown for results with or without the reflectors and with a 7 cm hole in the back reflector. If the reflectors are removed, the number of neutrons absorbed in the synovium is significantly reduced. For example, at 10,000 ppm, the reaction number drops 45% from 6.76×10^{-3}/source neutron to 3.74×10^{-3}/source neutron. The decrease in number of reactions is similar at other boron concentrations: 47% at 1,000 ppm and 44% at 19,000 ppm. Thus, a 7-cm diameter aperture

inside the back reflector causes a 2- 3% decrease in the number of boron neutron capture events in the synovium.

4.3.7 Detector outside of the therapy room

At this point, only detector positions inside the therapy room have been considered. It is worthwhile to explore the possibility of locating the photon detector outside of the therapy room so that the concrete structure of the therapy room itself (ceiling or walls) can serve as the detector shield. At Petten, the front collimator is made of lead and tungsten, which is designed for photon shielding only[13]. However, at LABA, even if the detector can be positioned outside the room, the collimator will still include two layers for shielding both neutrons and photons. The difference is a result of the presence of fast neutrons in the BNCS neutron beam as described above.

The possibility of locating the detector outside the therapy room was studied via simulation. The detector surface was located in the (90°, 270°) direction. The distance from the synovium to the concrete wall was 300 cm, and hence the detector was 300 cm + 50 cm (thickness of the wall) +10 cm (distance from the detector to the wall) = 360 cm from the synovium. The radius R of the detector viewing region was 4.3 cm, and the corresponding radius r of the aperture in the collimator was 3.355 cm.

The simulation results indicated that at a synovial of boron concentration of 10,000 ppm, the neutron count at the detector surface is 4.4×10^{-7} (/source neutron), 49% of that (8.9×10^{-7} /source neutron) at L = 200 cm (this position is inside the room). In addition, compared to those at L = 200 cm, the photon count drops from 1.1×10^{-7} (/source neutron) to 3.6×10^{-8} (/source neutron) for boron photons, and from 2.5×10^{-8} (/source neutron) to 1.7×10^{-8} (/source neutron) for hydrogen photons. The plateau background count under the boron peak is also less than that at L = 200 cm, which indicates that the yield of high-energy photons from concrete is not an issue.

The count rate in the boron photon peak is expected to be $3.60\times10^{-8}\times1.67\times10^{13}/60\times50\%$ = 5010 /(second·mA) (the full energy detection efficiency of the photon detector is again assumed to be 50%). In accordance with the previous conclusion regarding the response of B/N and B/H to L, both the values of the figures decrease as L increases, from 0.13 at L = 200 cm to 0.08 at L = 360 cm for B/N, and from 4.5 at L = 200 cm to 2.1 at L = 360 cm for B/H.

Therefore, from two aspects simulation results support the possibility of locating the detector out of the therapy room. First, the count rate of boron photons from the synovium is expected to be high enough. A count rate of ~ 5000 /second/mA means that the counting uncertainty reaches 1% in 2 seconds if the beam current is 1 mA. Second, the concrete wall can be used as the detector shield for both neutrons and photons since the neutron and photon fluxes are all apparently reduced.

4.4 Limitations of the Monte Carlo method

The Monte Carlo method has been extensively used in the preliminary design of the gamma ray telescope system. This approach has been very valuable for studying many aspects associated with the telescope system before a real telescope was assembled. With the help of the Monte Carlo method, the neutron and photon background distribution in the radiation room was determined; the performance of the telescope system, which was quantified with several figures of merit, was studied under various collimation and shielding conditions; the optimum location for the photon detector was determined.

However, the application of the Monte Carlo method was limited because of computational inefficiency. This issue became especially acute when determining the suitable thickness of the shielding materials. Variance reduction methods were implemented to improve the counting efficiency to make the required computational time acceptable. The F5 tally in MCNP, in which deterministic estimation is applied, has been widely used to estimate the neutron and photon fluxes. Another powerful variance reduction method in MCNP, DXTRAN, was also applied to accelerate the convergence of the particle current tallies (F1 tally in MCNP). The computational efficiency has been significantly improved with the appropriate use of these non-analog approaches.

Variance reduction methods have their limitations too. In MCNP, the efficiency of a Monte Carlo simulation is described with a quantity called FOM (Figure of Merit)[18]. FOM is defined as $1/(R^2 \cdot T)$, where R is the relative error of the result, and T is the computational time. Because T is proportional to the total number of transported source particles and R^2 is proportional to the reciprocal of it, FOM is independent of the number of source particles. Usually the application of variance reduction methods such as DXTRAN increases the average time used for tracking one source particle because more computational effort is needed. Therefore, to improve the overall computational efficiency, R^2 has to decrease more quickly than the increase in computational time T. R^2 can be decomposed into the sum of two components[18]: the component reflecting the history-scoring efficiency and the component expressing the dispersion in nonzero history scores. An effective variance reduction method works on either improving the history-scoring efficiency or decreasing the spread of the nonzero scores. The point detector and the DXTRAN method both belong to the first category. However, these methods failed when selecting the appropriate thickness of the shielding materials. This is because, while the scoring efficiency component of R^2 decreased, the second component of R^2 increased. The overall efficiency was deteriorated.

As a conclusion, the Monte Carlo method has been verified to be very valuable; however, because of its low computational efficiency, the solutions of some other issues such as the ultimate thickness of the

shielding materials and the response of a NaI detector in a mixed field of neutrons and photons can be more easily obtained through experimentation.

4.5 Conclusions

The application of appropriate collimators and detector shields can improve the performance of the telescope system dramatically. Online measurement of the synovial boron dose is promising. If the detector is located inside the therapy room, a large amount of shielding material must be used to both protect the detector and reduce the background count. The possibility of locating the detector outside of the therapy room is also supported by results of simulations.

The use of a NaI detector is also promising. Simulation results indicated that the count rate of the 478 keV boron photons from the synovium is much higher than that of the 511 keV annihilation photons, and also the count rate of 511 keV photons is basically not affected by variations in synovial boron concentration. Therefore, distinguishing the 511 keV annihilation peak from the 478 keV boron peak is not necessary, and the 511 keV photon count can be simply subtracted from the total photon count under the boron peak.

In the following three chapters, the building, testing, and characterization of a real telescope in the BNCS therapy room will be described, and the results and conclusions from the preceding simulations will be examined experimentally.

Chapter 5 Installation of the telescope system in the LABA radiation vault

In the last chapter, based on Monte Carlo simulations, it was concluded that a telescope system for online detection of the boron photons emitted from the synovium during BNCS clinical treatments is promising. This chapter focuses on installation and testing of a real telescope system in the LABA radiation vault. Problems such as detector shielding, not fully resolved in simulations, were studied during assembly of the collimator and the detector shield. Additional simulations were performed, partially because the ultimate experimental system was different in some aspects from the original simulation model, and partially because some new problems arose as the experiments proceeded.

5.1 Set up of the physical telescope system within the treatment facility

5.1.1 Locations of the photon detector and the collimator

At Petten, the ceiling of the treatment room served well as a suitable detector shield for the telescope system[13]. In the last chapter, the feasibility of positioning the photon detector outside the LABA radiation vault and using the concrete wall to shield the detector was confirmed. Accordingly, one choice could be to locate the detector outside the room if suitable space outside the therapy room is available and provided a centimeter-sized hole is drilled through the concrete.

The primary disadvantage of positioning the detector inside the radiation vault is that shielding the detector becomes a significant issue. However, there are also advantages for a position inside the room. First, according to results of simulations in Chapter 4, the boron photon count drops with distance faster than the neutron count and the 511 keV photon count, and hence the signal to noise ratio is higher at a shorter synovium-to-detector distance. Second, the possibility of moving the detector closer to the synovium exists. The influence of neutrons and high-energy photons on boron photon detection (which is dependent on a specific detector) has not been completely studied. (In simulations, only the B/N and B/H ratios were estimated). If the boron photons from the synovium cannot be separated from the background signal, one approach to improve the signal to noise ratio would be to move the detector closer the synovium.

While it is physically feasible to locate the detector outside of the LABA radiation vault, the decision was made to position the detector inside the vault for demonstration of the feasibility of the telescope system. Based on the results of simulations, the locations of the photon detector and the collimator were chosen as described in Chapter 4. However, other limitations, such as the space availability in the radiation vault, were also taken into account when determining the physical detector location. It was concluded via simulations that the detector should be located in a direction around (90^o, 270^o) to take the advantage of the optimal performance of the telescope (section 4.2.2) and convenient shield installation.

A synovium-to-detector distance, *L*, of approximately 200 cm was considered to be a near optimum choice from the point of view of good signal to noise ratio and sufficient space for addition of shielding materials.

The free space for the telescope was limited by the arrangement of the radiation vault. The restrictions came from the apparatus that had already been installed for other research projects and also from the reservation of some space for other purposes such as a pathway. The selected location is close to the optimal location identified in simulations. The value of *L* is 260 cm, and the direction of the detector is 15° off the beam line, corresponding to an azimuthal angle of 270°. The front surface of the collimator is 30 cm from the synovium, and this choice was also restricted by the space availability. In this arrangement, the collimator is close enough to the human body phantom that a slight increase in dose (approximately 5%) to a small region of the torso results. After knowing *L* and *l*, for a prescribed viewing region of the knee joint by the detector, the radius *r* of the aperture in the collimator can be calculated using the equations derived in Chapter 4. In the experiments described here, the locations of the detector and the collimator will not be changed, and it is the *r* that will be modified to adapt to the different sizes of the viewing region of the detector.

5.1.2 Photon detector

The feasibility of using a NaI detector for synovial boron photon detection was confirmed via Monte Carlo simulations as described in Chapter 4. The crystal size of the NaI(Tl) detector used for experimental studies is 10.2 cm × 10.2 cm. A picture of the detector is presented in Figure 5.1. Five gamma energies were used to calibrate the energy resolution of the detector: 511.0 keV from ^{22}Na, 661.6 keV from ^{137}Cs, 1173.2 keV from ^{60}Co, 1332.5 keV from ^{60}Co, and 1785.5 keV from ^{22}Na. Under the selected working parameters of the detector, the FWHM (Full Width at Half Maximum) of the photon peaks is 42.8 keV, 51.2 keV, 66.9 keV, and 71.4 keV, and 88.1 keV, respectively. The FWHM of NaI detectors can be approximated with an analytical expression[18]:

$$\mathrm{FWHM} = a + b \cdot \sqrt{E + c \cdot E^2} \ ,$$

where E is the photon energy in keV, and a, b, c are the coefficients. With the help of *Matlab*, the values of a, b and c were estimated as 2.5659, 1.7090, and 0.0002, respectively. The energy resolution of the NaI detector at other energies can be estimated with this equation. In particular, the FWHM for 478 keV photons is 41.7 keV, corresponding to an energy resolution of 8.7%.

Figure 5.1 Picture of the NaI detector used in experiments. The 10.2 cm × 10.2 cm NaI crystal and the PMT are encapsulated inside the aluminum shell.

5.1.3 Collimator and detector shield

Lead and boronated polyethylene were selected as photon and neutron shielding materials. Standard lead bricks, 20.3 cm × 10.2 cm × 5.1 cm were used to build most of the lead shield; various other pieces of lead were also used. The boronated polyethylene contains 2 wt% of natural boron and 12.05 wt% of hydrogen, and thus this material is a good fast neutron moderator and low energy neutron absorber. The polyethylene has been machined into one-inch thick slabs with various lengths and widths. A potential problem of using boronated polyethylene as the neutron shielding material is that the tremendous number of boron photons generated in it could interfere with the detection of the boron photons from the synovium. However, it was predicted in simulations that the boron photon count from the synovium will be much higher than that from the polyethylene shield.

Both the collimator and the detector shield consist of a layer of boronated polyethylene and a layer of lead. The thicknesses of boronated polyethylene and lead in the collimator and the shield were not obtained through simulations, but through experimentation. The initial thickness of the boronated polyethylene layer and the lead layer in the collimator and in the shield was set at 15 cm and 20 cm, respectively, and the ultimate thicknesses of the materials was determined experimentally.

Special attention had to be paid to the streaming effect when positioning the shielding materials. In Monte Carlo simulations, a lead or polyethylene layer in the shield and the collimator was modeled as a whole entity. However, in experiments, any shielding unit had to be built with smaller pieces of lead bricks or polyethylene slabs. Accordingly, gaps between the neighboring units are generally unavoidable, and it is possible for neutrons and photons to travel through the gaps without being intercepted in the shield. The streaming effect was addressed by a staggering arrangement of the shielding materials, and the effectiveness of this on reduction of particle streaming was confirmed experimentally.

The detector shield is stacked on two heavy-duty steel tables, each of which can hold 1500 lbs. The space under the top surface of the tables is filled with boronated polyethylene to attenuate neutrons scattered from the floor. The collimator is located on a third steel table.

5.1.4 Phantoms of the human body and the synovium

The human body phantom is composed of two uncovered plastic boxes which represent the torso and one of the legs[6]. (The assumption is that the second leg can be moved out of the way of the direct neutron beam during treatment.) The knee region is surrounded on 3 sides by 10 cm thick graphite reflectors, as described in Chapter 3. The structure of real knee joints is rather complicated. In the previous Monte Carlo simulations, the fine structures of the joint were ignored, and the part of the synovium loaded with boron compound was simply represented with a thin cylindrical shell. Given the relatively long mean free path of fast and even thermal neutrons in tissue, this simplification is justified. The primary objective of the experiments at the initial stages was to verify the correctness of the simulation results and to explore the feasibility of the telescope system for BNCS. Consequently, the effort of making a more realistic model of the joint and the synovium was not necessary. In Chapter 7, Monte Carlo simulations will be conducted to do comparisons between experimental results and simulation results for a simple configuration of the synovium. If the validity of the Monte Carlo method can be proved under a simplified phantom model, the real situations under a more complicated model can be roughly understood through running Monte Carlo simulations. In this human body phantom, the leg-shaped plastic box is used to represent a leg, and the structure of a knee joint is not included.

5.1.5 Preparation of synovium phantoms

The synovium is represented by specially made synovium phantoms. These synovium phantoms contain various amounts of boron compound to represent the synovium with various boron concentrations. From the point of view of boron photon production and detection, the molecular structure and the composition of the boron compound used in the phantoms is unimportant; what is important is the total amount of ^{10}B and its spatial distribution. Therefore, although the appropriate ^{10}B compound for BNCS is still under investigation, the results obtained from this research will be valid for any compound. The boron compound used in the construction of the synovium phantoms is B_4C, which is in the form of a very fine powder and has a purity of almost 100%. It was assumed that the boron concentration was uniform throughout the synovium. Several phantoms with boron concentrations of 0 ppm, 2,000 ppm, 5,000 ppm, 10,000 ppm, 15,000 ppm, and 19,000 ppm were made.

Initially, the B_4C powder was simply poured into plastic tubes with a diameter of one or two centimeters. The effort in phantom preparation was trivial; however, the experimental outcome was very

disappointing. The tubes representing various boron concentrations were tested, but no reliable difference in the boron photon count could be detected. It was determined that this failure was due to the neutron self-shielding effect inside the mass of boron compound. The thermal neutron flux at the center of the plastic tube is much weaker than that at the outer surface, since many of the thermal neutrons are absorbed in the boron compound on their way to the center to the tube. Thus, the majority of the neutron capture events occur in the very outer region of the tube, and the compound close to its center is "wasted". MCNP simulations were performed to demonstrate this effect more explicitly. Figure 5.2(a) shows a cross-section through an MCNP model of a tube, 1.5 cm in diameter, divided into eight concentric shells, each of which has 1/8 of the total volume of the boron compound. The number of boron neutron capture events in each shell is plotted in Figure 5.2(b) (the data in Figure 5.2(b) have been normalized by the total number of captures in the boron compound). The outermost shell contributes 63% of the total absorptions in the phantom, and by comparison the innermost layer only contributes 5%. The total number of boron neutron captures in these phantoms is small, and the variation of boron uptake within the synovium is unlikely to be noticed.

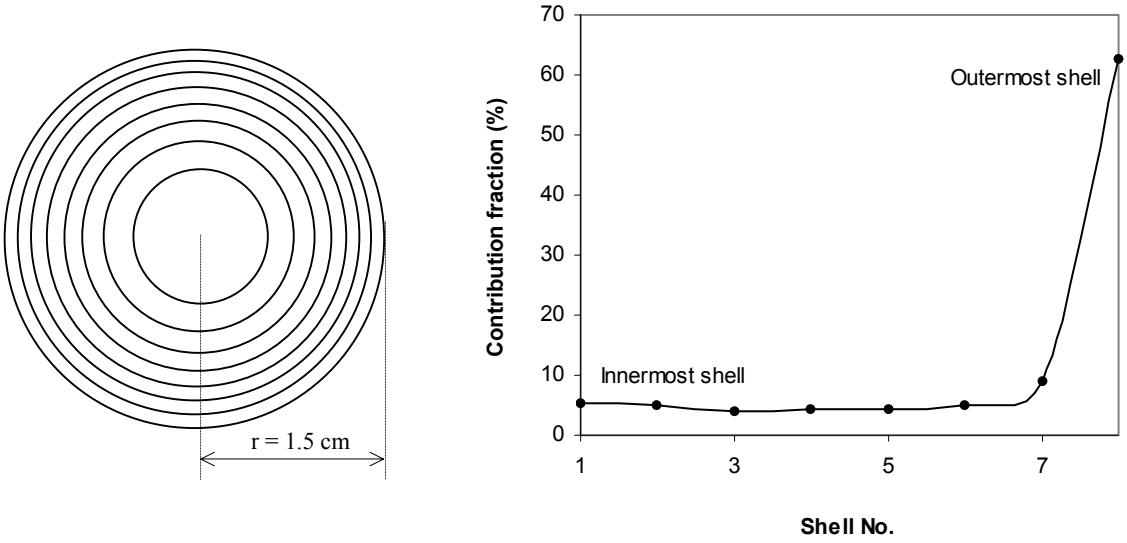

(a) (b)

Figure 5.2 (a) Division of the cylinder (1.5 cm in radius) into eight concentric equal-area regions; (b) fraction of $^{10}B(n,\alpha)$ reactions occurred in the eight regions.

The way to improve this situation is to increase the total surface area of the synovium phantom. In MCNP simulations described in the preceding chapters, the boronated synovium was represented by a thin shell (0.15 cm) formed by two concentric cylindrical surfaces. The influence of the self-shielding

effect was not as significant as that for the solid cylinder phantoms described here. However, the apparent non-linearity (saturation) emerging at high boron concentrations in Figure 3.5 indicates it still affects the results.

Another simple phantom configuration was tested next. The boron compound was spread into a square-shaped thin layer (< 1 mm). MCNP simulations were employed to compare three different sizes of the layer: 2 cm × 2 cm, 4 cm × 4 cm, and 6 cm × 6 cm. It was confirmed in simulations that the larger the surface area, the greater the number of neutron capture events. On the other hand, the number of boron photons detected by the NaI detector is also controlled by the size of the aperture in the collimator. The larger the size of the synovium phantom, the larger the radius of the aperture has to be if the entire sample is to be viewed by the detector. With a larger aperture in the collimator, the detector receives more neutrons and background photons from the knee region. The radius of the aperture was selected to be 2 cm to avoid the potential overwhelming background counts at larger apertures. Under this dimension of the aperture, the greatest number of boron photons was detected for the layer size of 4 cm × 4 cm. Thus, the size of the phantom was chosen to be 4 cm × 4 cm.

In a synovium phantom, the B_4C compound has to be uniformly distributed in a volume with a surface of 4 cm × 4 cm. It was shown mathematically in Chapter 4 that different parts of the detector viewing region may have different photon detection probabilities. After a perfect alignment is achieved, 478 keV boron photons produced at the center of the synovium phantom have the largest probability of arriving at the detector; in contrast, those produced at the edge of the phantom have the lowest probability. If the boron compound is not distributed uniformly throughout the phantom, the number of detected photons will depend not only on the boron concentration, but also on the spatial distribution of the boron compound in the phantom. This should be avoided since it would be hard to separate the count change only due to the change of the boron concentration.

Several approaches to phantom construction were attempted before a method capable of generating thin layers (< 1mm) with uniform boron distribution was developed. This method used a mixture of flour and boron compound. First, the B_4C was blended with flour in a 4 cm × 4 cm plastic bag; it was relatively easy to mix the two dry powders evenly. Next, water was added to make a piece of dough. Then, the plastic bag was sealed, and put between two lead bricks with smooth surfaces. It was found that a very thin and uniform layer of flour and boron compound could be made under the pressure of the lead. The uniformity could be approximately checked by holding the phantom toward light and examining the transparency of different regions. A potential problem with the phantoms was that flour might go moldy after some time; however, this was not a problem. The phantoms have been used for a long time, and the experimental results remain very consistent.

The synovium phantom was located inside the leg phantom parallel to the front surface of the moderator/reflector assembly, and the symmetric axis of the moderator/reflector assembly intersects the phantom at its center.

When choosing the configuration of the synovium phantom used in experiments, there was no intention to mimic a real synovium. The reasons are similar to those described in Chapter 3 when choosing the configuration of the synovium phantom in the Monte Carlo simulation model. First, the issues such as neutron flux suppression in the synovium phantom and photon attenuation in the joint are common for synovium phantoms of various configurations. Even though the number of boron photons emitted from the synovium and the number of boron photons detected are dependent on the configuration of the phantom, the most crucial task of the preliminary experiments is to examine whether the boron photons from the synovium can be detected above background. Further, the real situation for a complicated realistic synovium will be understood based on the work for much simple configurations. Second, the adoption of a simple synovium phantom configuration is helpful for avoiding the misleading results caused by other factors that could affect boron photon production and detection such as non-uniformity of boron compound in the phantom, the configuration of the phantoms was chosen to be simple. Third, simple phantoms of sufficient quality can be more easily made, thus ensuring that the variation of the detected boron photon count under various boron concentrations is attributed to the variation of synovial boron concentration. The effect of various configurations of the synovium phantom on boron photon production will be studied and compared in Chapter 7, and the factors that affect the boron photon production will be discussed.

5.1.6 Schematic of the telescope system

A schematic of the experimental setup of the telescope system is shown in Figure 5.3. The telescope system consists of a NaI(Tl) photon detector, a collimator, and a detector shield. The collimator includes two layers: the Rico-Rad layer for neutron shielding, and the lead layer for attenuating photons. The thicknesses of the two layers were initially set at 15 cm and 20 cm, respectively. The detector shield is the biggest part in the system, both in volume and in weight. It also contains an outer layer of Rico-Rad (initially set at 20 cm thickness) and an inner layer of lead (initially set at 15 cm thickness).

The radius of the aperture in the collimator is 2 cm, and the corresponding radius R of the detector viewing region at the position of the synovium phantom is 2.5 cm. The value of R is a little less than $2\sqrt{2}$ = 2.8 cm, at which the whole phantom (4 cm × 4 cm) is viewable to the photon detector. Therefore, the photon detector cannot "see" the four corners of the phantom.

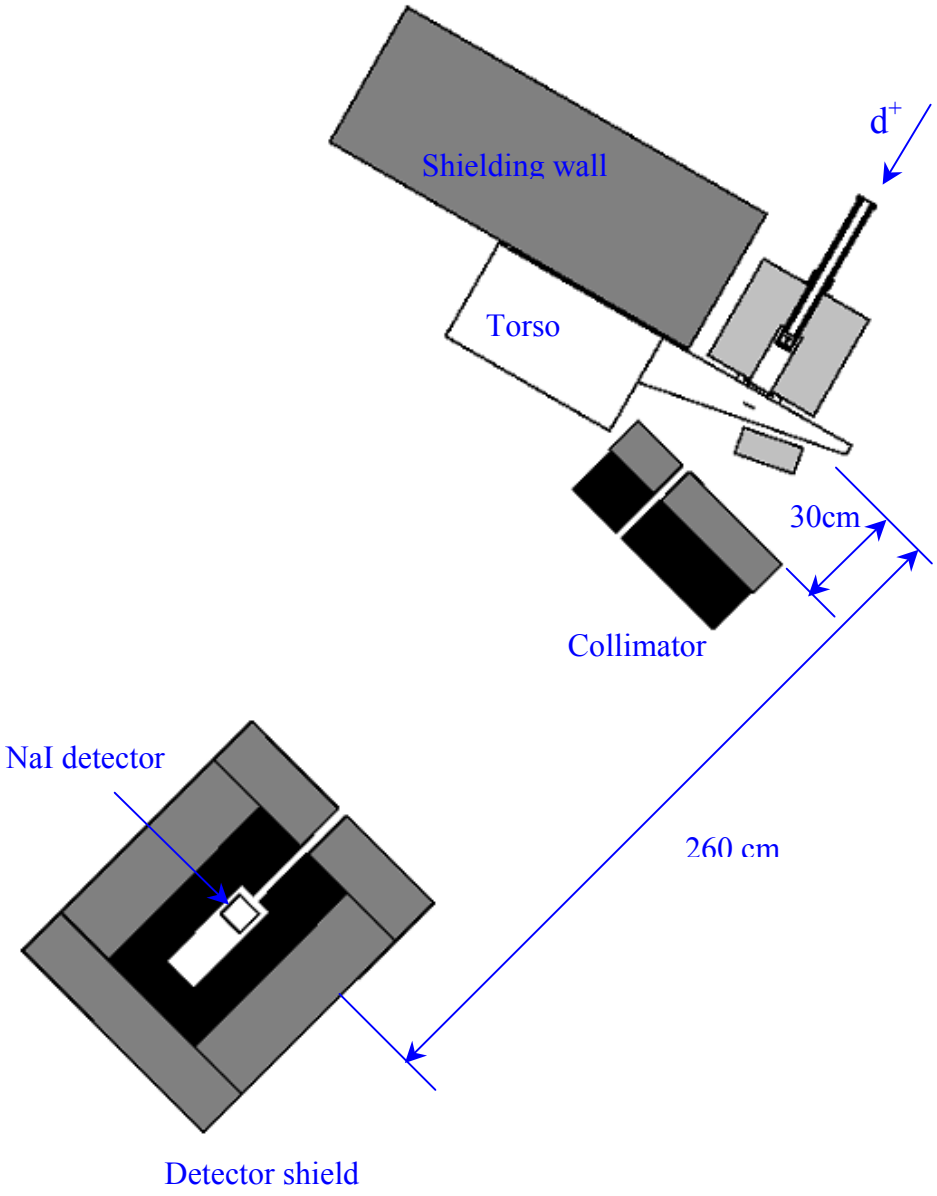

Figure 5.3 Schematic of the configuration of experimental setup, including the beam part (beam tube, target, and moderator/reflector assembly), the human body phantom, and the telescope system.

5.1.7 Accessory electronics system and operational parameters

The accessory electronic system is very simple. The signals collected by the detector pass through a preamplifier and an amplifier[14] in sequence. Then the shaped and amplified signals are transmitted to a computer based multi-channel analyzer[14] to be analyzed.

The accelerator beam current was set at 100 μA, one order of magnitude lower than the expected current in BNCS clinical treatments. The nuclear reaction for neutron production was ^{9}Be(d,n) at a deuteron energy of 1.5 MeV. The energy and angular distributions of the source neutrons from the ^{9}Be target were introduced in Chapter 3. The multichannel analyzer, made by EG & G ORTEC (model 916 A), was set at a total channel number of 512. At a beam current of 100 μA, the dead time of the MCA was ~10% after sufficient shielding (described in section 5.6) was positioned. The spectrum collection was set to 100 seconds (live time). During spectrum collection, the beam current, which was monitored with the control software of the accelerator, fluctuated around the prescribed value (100 μA). Therefore, after each measurement the spectrum was normalized to exactly 100 μA, based on the value of the total collected charge on the beryllium target.

5.2 Collimation

To make proper measurements of the 478 keV boron photons from the synovium, the symmetric axes of the synovium phantom, the aperture in the collimator, and the aperture in the detector shield have to be carefully aligned with the central axis of the NaI detector. Otherwise, the measured boron photon count rate will be lower than expected since misalignment is equivalent to adopting a smaller pinhole in the collimator.

Alignment was performed with a laser level, the beam size of which was about 1 cm in diameter. When doing alignment, the leg phantom was removed. The laser level was put at the position of the phantom center with the laser beam pointing in the prescribed direction. Then, the positions of the collimator and the detector shield were adjusted so that the laser beam passed through the center of the apertures, and was interrupted at the center of the detector surface. The difficulty in the alignment process is a result of the large distance between the detector and the synovium phantom (~260 cm) since a small positional deviation at the phantom side may cause a much larger deviation at the detector side.

5.3 Detected photon spectrum

The features observed in the measured photon spectrum are strongly related to the shielding conditions around the photon detector. Initially, before the front part of the detector shield was installed, no photon spectrum could be recorded. A dead time of 100% was read from the control software of the multi-channel analyzer (MCA). After more shielding materials were added, the photon spectrum appeared, but no separate photon peaks were discernable. A large low-energy contribution with a steep slope emerged at the low energy end of the spectrum, which indicated the detection of a tremendous number of low energy

particles (photons, x-rays and/or neutron-induced heavy ions). After the detector was sufficiently shielded, discrete photon peaks began to appear.

A representative photon spectrum taken by the MCA for the NaI detector under the shielding conditions described in section 5.1.6 is shown in Figure 5.4. Four photon peaks are easily distinguishable: the 2223 keV hydrogen peak, the 133.6 keV peak from thermal neutron capture in ^{127}I, the 203 keV peak from neutron inelastic scattering on ^{127}I, and the "boron peak" covering the energy region of Doppler-broadened 478 keV photons as well as 511 keV photons. Other possible peaks include the single and double escape peaks of 2.223 MeV photons, with energies of 1.712 MeV and 1.201 MeV, respectively. However, these escape peaks are not visible in the spectrum. The area under the "boron peak" is the largest of the photon peaks. However, when recording the photon spectrum, there was no boron loaded in the synovium phantom. Therefore, this peak is entirely a "background" peak. The composition of the background peak is complicated, and the details will be supplied in section 5.4 as well as in the next chapter.

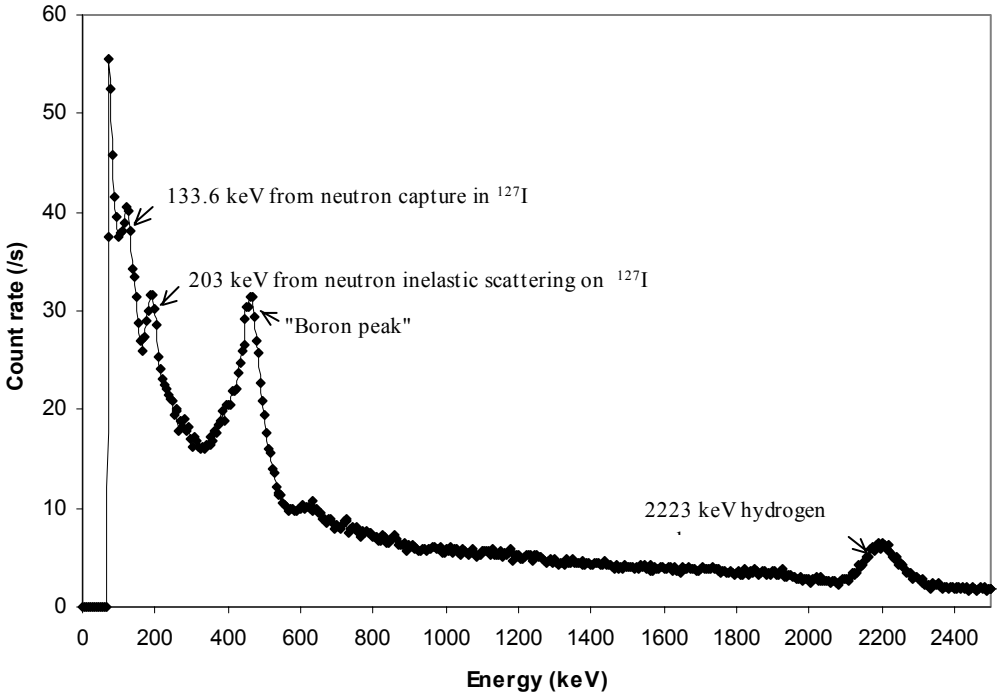

Figure 5.4 Photon spectrum collected by the NaI detector under the configuration illustrated in Figure 5.3.

Given the existence of a background boron peak, the synovium phantoms were put into position to test whether the boron photons originating from the synovium could be detected above the background. Comparison was done on two cases: one with no boron compound in the synovium, and another with

10,000 ppm. Figure 5.5 shows the measured photon spectra under the different boron concentrations. A very sharp increase in the boron peak area when the synovial boron concentration is increased from 0 ppm to 10,000 ppm is observed. In fact, contributions from the synovial boron photons are discernable at synovial boron concentration as low as 2,000 ppm. Results will be discussed in Chapter 7.

The stripped spectrum, obtained by subtracting the no boron spectrum from the 10,000 ppm spectrum, is also presented in Figure 5.5. In this spectrum, except for a very sharp 478 keV boron peak, there are only some small fluctuations around zero. Thus, the presence of the boron compound in the synovium affects only the boron peak region in the spectrum, and its impact on the rest of the spectrum is negligible.

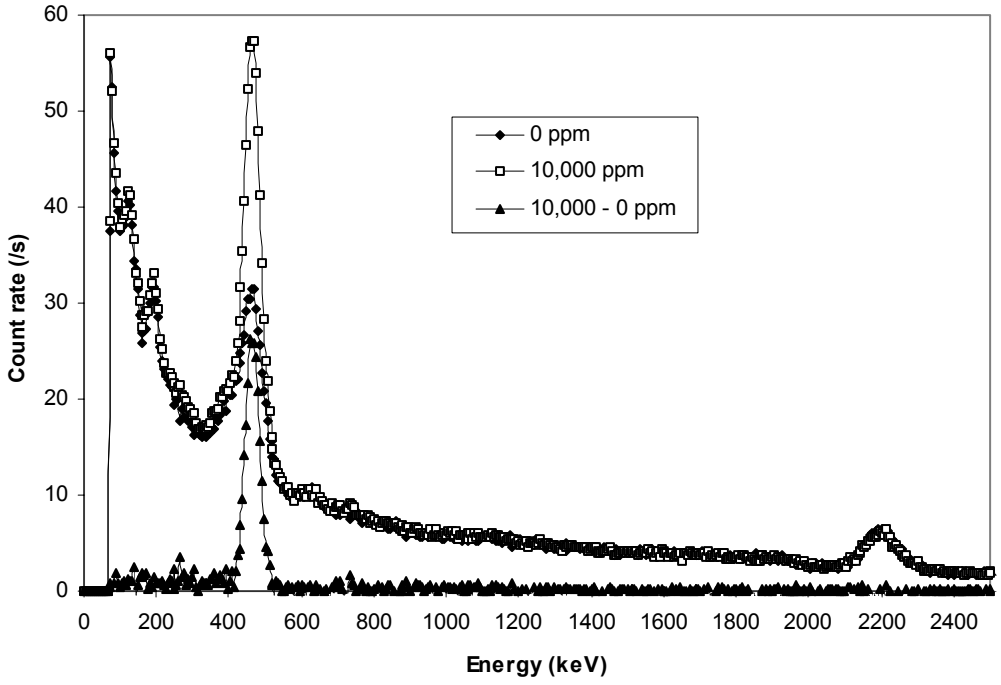

Figure 5.5 Photon spectra at 0 ppm and 10,000 ppm of synovial boron concentration and stripped spectrum derived from subtraction of the 0 ppm spectrum from the 1,0000 ppm spectrum.

5.4 Exploring the spatial distribution of the background counts

Without detector shielding, the count of 478 keV photons from the synovium is completely submerged in the background noise. On the other hand, the background count cannot be fully eliminated even with shielding because of the existence of an aperture in the detector shield. When building the collimator and the detector shield, the initial thicknesses of the shielding materials were chosen based on results of simulations. It was predicted in simulations that with this shielding, the primary channel for neutrons and

background photons to enter the detector would be the aperture in the detector shield. First, however, it was necessary to experimentally determine whether the thicknesses of the shielding materials are really sufficient before the possibility of further background reduction could be explored.

As illustrated in Figure 5.6, neutrons and photons can hit the detector from six directions, i.e., the front, back, left, right, top, and bottom sides of the NaI detector. The aperture in the detector shield is on the front side of the detector. The appearance of the neutron induced photon peaks (133.6 keV and 203 keV) in Figure 5.4 reveals the existence of a neutron field inside the NaI crystal. It is worthwhile to study where the remaining background count comes from, after the collimator and the shield have been settled. This investigation will supply direct evidence to answer questions such as whether the thickness of the shielding materials (lead and boronated polyethylene) is sufficient, whether the streaming effect has been overcome, and whether the aperture (pinhole) in the shield is the primary passageway for background neutrons and photons to enter the detector. The investigation could also provide clues to clarify the origin of the background boron peak: is the background peak formed by the photons produced outside the detector (511 keV annihilation photons and/or 478 keV photons produced in boronated polyethylene) or by the photons induced by neutrons inside the NaI detector (511 keV annihilation photons, prompt or delayed photons following neutron inelastic scattering or capture).

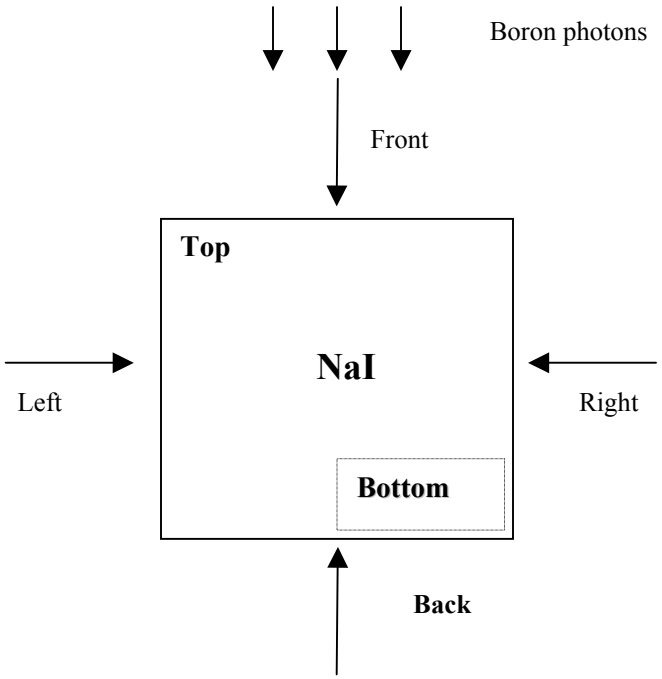

Figure 5.6 Schematic of the NaI detector, showing that background particles can enter the detector from six directions.

The approach taken was simply to sequentially add more photon or neutron shielding materials to one side of the detector and then to check whether the measured photon spectrum and the background boron peak were affected. If the spectrum and/or the boron peak were not changed after the addition, the shielding on that side was considered sufficient. If the spectrum and/or the boron peak were altered significantly, more neutron and/or photon shielding would be added to that side of the detector. The additional shielding material was added directly adjacent to the detector inside the existing shielding rather than to the outside. To test the neutron background and the photon background individually, separate layers of cadmium or lead were used. The influence of fast neutrons could not be studied directly since cadmium is only good for absorbing thermal neutrons, and the narrow space between the detector and the inner surface of the lead shield would no longer permit additional neutron moderating material. However, under such a shielding condition, generally thermal neutrons and fast neutrons will be present together. Accordingly, in any direction, noticeable attenuation of thermal neutrons also implies the presence of fast neutrons.

5.4.1 Photon and neutron background test on left, right, top, bottom, and back sides

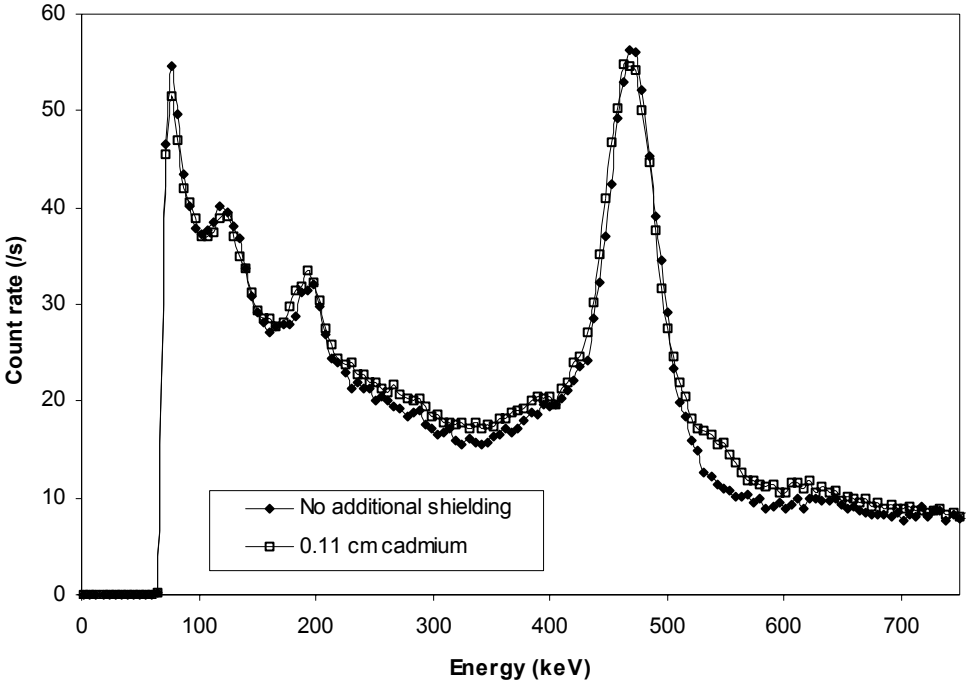

Figure 5.7 Boron peak and low energy region in the photon spectrum before and after the addition of 0.11 cm cadmium on all side of the detector except for the front side.

Separate experiments were conducted on each of the left, right, top, bottom, and back sides. The thicknesses of lead and cadmium used were 1.27 cm (1/2 inch) and 0.11 cm (1/24 inch), respectively. The mean free path of 478 keV photons in lead is about 0.5 cm, and 1.27 cm of lead is enough to attenuate these photons by one order of magnitude. On the other hand, essentially no thermal neutrons can penetrate 0.11 cm of cadmium. (The mean free path of 0.025 eV thermal neutrons in cadmium is 0.0088 cm.) It was found that no change in the measured spectrum was observed after the extra shielding material was appended, regardless of whether it was lead or cadmium. Next, the shielding material was added on the five sides at the same time to examine the overall background contribution from these five directions.

No difference in the photon spectrum was observed after the addition of the additional lead, which verified that the photon count contribution from these directions could be neglected. The spectra prior to and after the addition of the cadmium sheets appear in Figure 5.7. In Figure 5.7, minor changes in the measured spectrum are noticed. In particular, a small bulge is recognizable on the right shoulder of the background boron peak. The central energy of this small photon peak is around 559 keV, indicating that it is a result of (n,γ) reaction in cadmium[21]. (The emission of a 559 keV photons accompanies 73% of cadmium neutron captures.) On the other hand, the shape of the remaining spectrum and the boron peak does not appear to be altered, indicating that the neutron current coming from all directions other than the front surface is weak and does not affect the detected spectrum. (Actually the neutrons absorbed in the cadmium layer also include those escaping the interior of the NaI crystal; therefore, the number of neutrons coming from the exterior of the detector is even less). As a result, we can conclude that both the neutron and photon shielding in all directions other than the front is sufficient, and the addition of more shielding materials will not improve the performance of the detector shield.

5.4.2 Background test on the front side of the detector

Background reduction tests with lead and cadmium were also performed on the front side of the detector to examine the influence from neutrons and photons entering the detector in this direction. Two trials with lead were conducted. In the first trial, 5 centimeters of lead were located right in front of the detector (inside the existing shield), completely covering the front surface. In the second trial, 5 more centimeters of lead were positioned in front of the polyethylene layer of the detector shield (outside the existing shield), covering the aperture in the shield. The detected spectra as well as the original one (no extra lead), are presented in Figure 5.8. The photon spectrum is dramatically changed after the extra lead is applied: the slope at the low energy region of the spectrum is completely eliminated, and the 133.6 keV and 203 keV photon peaks are more distinct; even after 10 centimeters of lead (trial two) block the aperture in the detector shield, the background boron peak is still very apparent. About 1/4 of the total count under this peak is lost with 5 centimeters of lead covering the front surface of the detector (trial

one). This finding rejects the possibility that this peak is mainly caused by 478 keV and/or 511 keV photons produced outside the detector since otherwise this 5 centimeters of lead should have attenuated the count of this peak by 4 to 5 orders of magnitude. Figure 5.9 shows the hydrogen peak before and after the extra lead shielding. Five centimeters of lead in front of the detector (trial one) eliminates the 2223 keV hydrogen peak, which indicates that the detected hydrogen photons enter the NaI crystal from the front side of detector. These hydrogen photons are most likely produced in the regions neighboring the synovium and the polyethylene layer in the collimator.

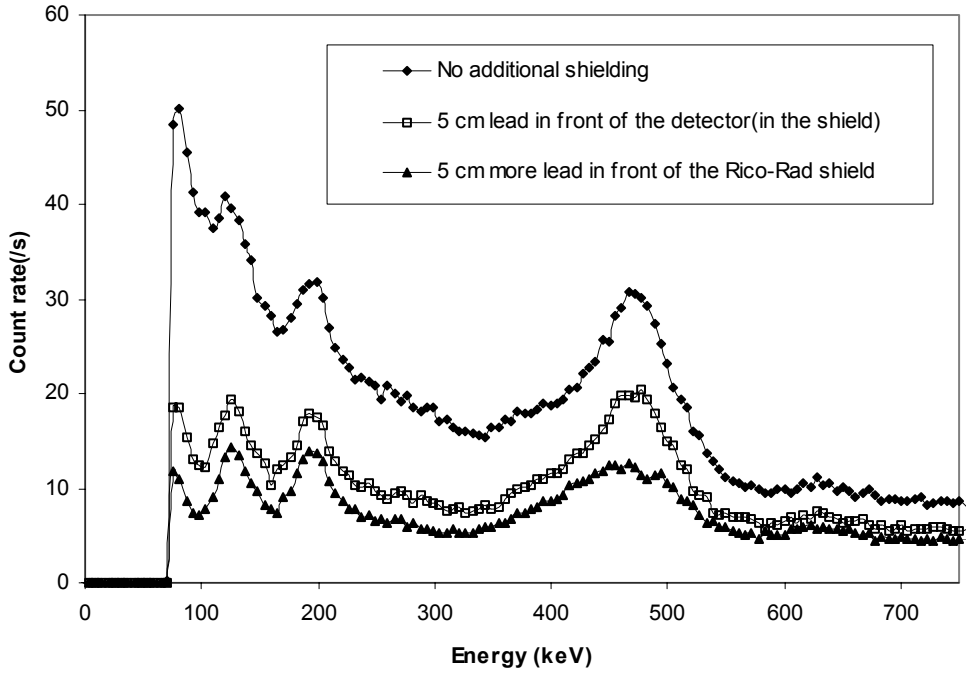

Figure 5.8 Boron peak and low energy region in the photon spectrum before and after the addition of the additional lead in front of the detector.

Figure 5.10 shows the results for the cadmium test. 0.11 cm (1/24 inch) to 0.42 cm (4/24 inch) of cadmium was attached to the front surface of the NaI detector. After cadmium shielding, two regions in the detected spectrum are affected: the low energy region, and the background boron peak. The low energy slope is eliminated with only 0.11 cm of cadmium. The plateau under the 133.6 keV peak is attenuated much faster than that under the 203 keV peak. The mass attenuation coefficient of cadmium is 1.43 cm^2/g at 100 keV, 0.28 cm^2/g at 200 keV, and 0.088 cm^2/g at 500 keV, respectively. After penetrating through 0.11 cm of cadmium, the fraction of photons stopped in cadmium is 0.73 at a photon energy of 100 keV, 0.23 at 200 keV, and 0.08 at 500 keV. That is, such a thin layer of cadmium is already very effective in attenuating photons of 100 keV, but for photons of higher energies such as 500 keV the

effect is very slight. This is consistent with the appearance of the photon spectra in Figure 5.10, and demonstrates that the large contribution at the low energy end of the spectrum is mainly formed by low energy photons, not by heavy recoil nuclei gaining energy through elastic or inelastic scatterings with neutrons inside the NaI crystal. For the background boron peak, addition of cadmium results in the appearance of a small peak on the high-energy side. This peak corresponds to the 559 keV photons emitted following cadmium neutron capture, which confirms the existence of low energy neutrons coming from the front side of the detector. In addition, the height of the boron peak is reduced, and the peak channel shifts toward the high energy. The reduction in peak height is due to the loss of photon contribution from thermal neutron captures in the NaI crystals. From Figure 5.10, the peak count loss after the attachment of a thin cadmium layer is small compared to the total peak count. However, this does not mean that the photon contribution to the boron peak from thermal neutron captures is small. The explanation is the following: first, cadmium is only effective in absorbing neutrons with a very low energy (the "cutoff" energy of cadmium is 0.4 eV). Second, neutrons can be moderated inside the NaI crystal, which is confirmed by the appearance of a very apparent 133.6 keV peak from the $^{127}I(n,\gamma)$ reaction even after the front surface of the photon detector is covered with 0.42 cm of cadmium. The magnitude of the neutron-based contribution to the background boron peak will be discussed in Chapter 6.

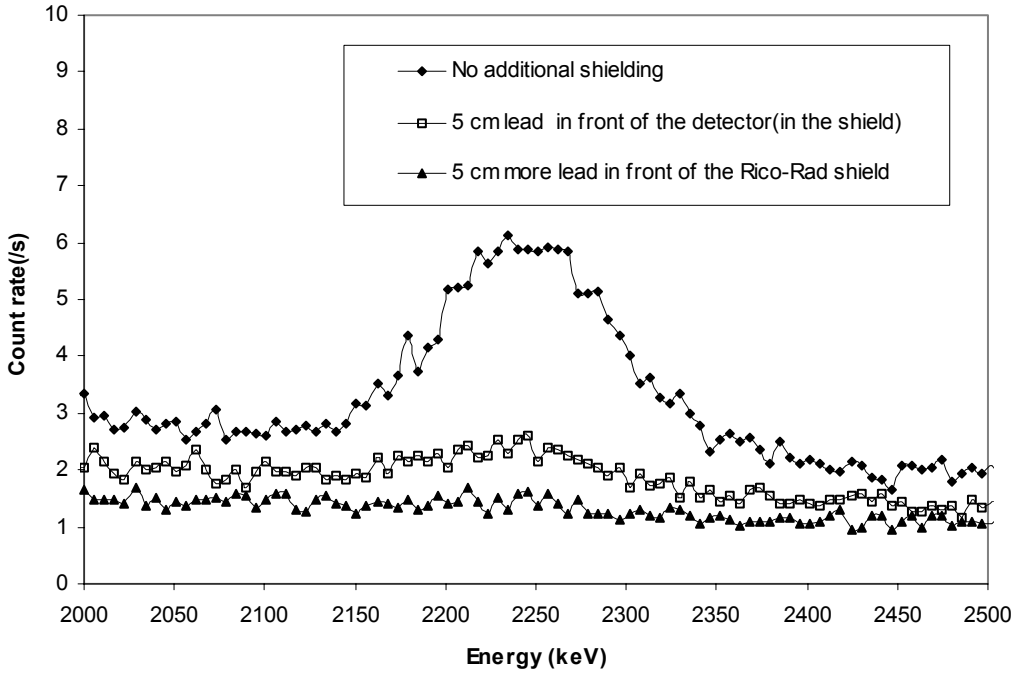

Figure 5.9 Hydrogen peak in the photon spectrum before and after the addition of the additional lead in front of the detector.

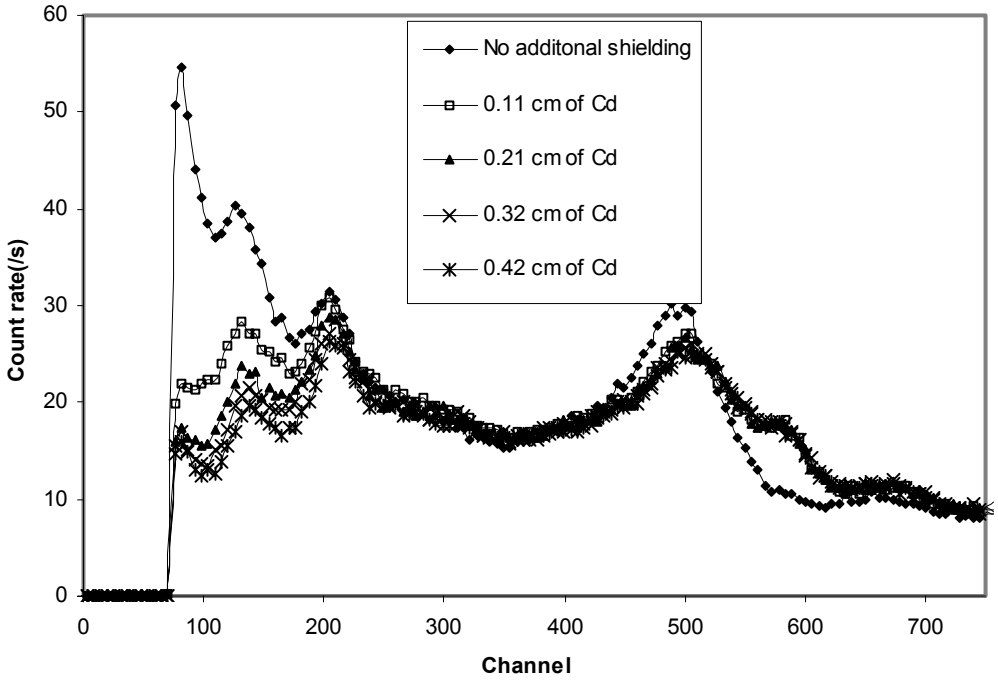

Figure 5.10 Boron peak and low energy region in the photon spectrum before and after the addition of the additional cadmium to the front surface of the detector.

5.4.3 Gold foil experiment

A second set of experiments was performed to examine the intensity of the neutron flux in the polyethylene layer in the detector shield in various directions. The method was neutron activation of gold foils[14]. A radioactive nucleus ^{198}Au is produced after a neutron is captured in a ^{197}Au nucleus. The half-life of ^{198}Au is 2.695 days, and its activity can be measured by counting the photons accompanying its decay. The primary limitation of this method is that only slow neutrons and resonance neutrons can be detected because of the small capture cross section for fast neutrons. To separate the contributions from thermal neutrons and resonance neutrons, the cadmium difference method can be applied: two identical gold foils, one covered with cadmium and another not, are irradiated in the same neutron field. Both thermal neutrons and resonance neutrons activate the foil with no cadmium cover, whereas the foil covered with cadmium only records the contribution of resonance neutrons since thermal neutrons are stopped in cadmium. The count difference between the two foils gives the sole contribution from thermal neutrons.

The neutron shield is constructed with one-inch thick boronated polyethylene sheets. In this experiment, gold foils were affixed to surfaces of 0 to 5 inches from the outer surface the polyethylene shield on five sides of the shield (front, top, left, right, and back sides). After irradiation, the 416 keV photons emitted from gold foils were detected using an HPGe detector and a counting time of 200

seconds (live time). Both cadmium covered and uncovered foil activation were performed in boronated polyethylene in front of the detector, and only cadmium uncovered foil activation was done on the other four sides. The results are presented in Figure 5.11. The anisotropy of the neutron flux around the detector is evident. The neutron field on the front of the detector is much more intense than that from other directions. This is reasonable since the neutrons from the high-flux regions such as the leg phantom and the floor under the heavy water/graphite assembly are more likely to be scattered toward the front side of the polyethylene shield than toward any of the other sides. The curve from the cadmium-covered gold foils shows that the fast neutron flux is high. The relative contribution of thermal neutrons on the front of the detector was estimated using the cadmium difference method. Thermal neutrons dominate the cadmium neutron capture at the outermost surface of the polyethylene shield in front of the detector; however, their relative contribution drops with increasing thickness of the boronated polyethylene shield. At the outermost surface, the count from thermal neutrons accounts for 62% of the total 416 keV photon count. After one inch of boronated polyethylene, their contribution drops to about 17% of the total count. The function of boronated polyethylene in moderating and stopping fast neutrons is also apparent, but the effectiveness is much weaker than that for thermal neutrons. The results in Figure 5.11 suggest that attention should focus on the front side of the detector when constructing the neutron shield, and the shield could be very thick in order to significantly attenuate fast neutrons. The final thickness will be determined in section 5.6.1.

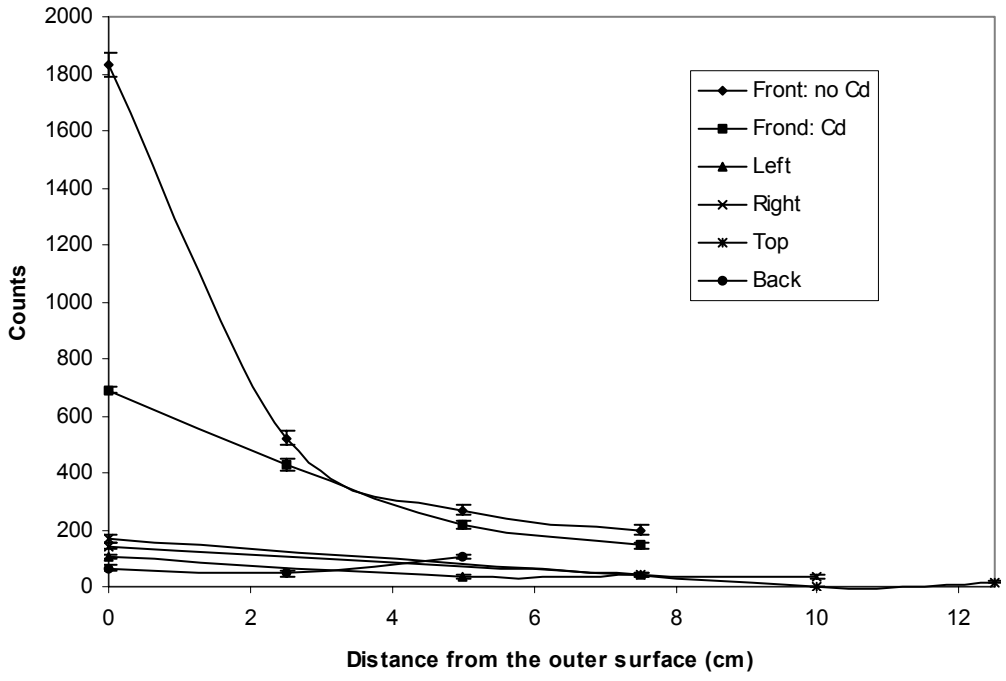

Figure 5.11 416 keV photon counts measured from gold foils irradiated with neutrons at various locations in the Rico-Rad shield.

5.5 Examination of the alignment

The precision of the alignment of the components of the telescope was examined, both on the side of the synovium phantom, and at the location of the detector. In the first method, the synovium phantom was moved ± 1 cm in each of three orthogonal directions. When the alignment is correct, the 478 keV photon count rate goes down as the phantom moves off its original position in all possible directions. Using the synovium phantom containing 10,000 ppm boron, the boron photon count rate was found to be the highest at the original position, and the count rate dropped very sharply whenever the phantom moved off this position, confirming the accurate alignment of the phantom and collimator aperture relative to the detector.

It is also necessary to evaluate the alignment of the detector relative to the aperture and synovium phantom. Photons originating from different regions in the viewing field of the detector have different probabilities of arriving at the detector. If the system is properly aligned, the viewing region of the detector should be centered on the symmetric center of the boron-containing synovium phantom. Thus, the 478 keV photons produced at the center of the phantom have the largest probability of being detected, and those emitted at the edge of the sample have the least probability. Similarly, if the alignment is perfect, the center of the front surface of the detector receives the greatest number of the 478 keV photons from the synovium, per unit area, and the edges of the surface will receive fewer or no boron photons.

An experiment was developed to roughly test the uniformity of 478 keV photons and neutrons on the front surface of the detector. A 2.5 cm × 2.5 cm square of cadmium, 0.6 cm thick, was attached to various locations on the front surface of the detector. This thickness is enough to absorb almost all thermal neutrons incident upon it. The mass attenuation coefficient of cadmium to 478 keV photons is 0.10 cm^2/g, and therefore 40% of the 478 keV photons will be lost during penetrating through this cadmium patch. Since the distribution of 478 keV photons on the detector surface is not uniform, the reduction in the boron photon count rate is dependent on the location of the cadmium patch. The greater the reduction, the greater the photon contribution at that location. For neutrons, it was shown in section 5.4.2 that a thin layer of cadmium (0.11 cm) could significantly change the shape of the detected boron peak by adding a 559 keV peak due to the $^{113}Cd(n,\gamma)$ reaction. If the neutron distribution on the surface is fairly uniform, after the attachment of the cadmium patch the detected spectrum will not show this additional peak since the area of the patch is only 6.25 cm^2, 8% of the total area of the front surface. On the other hand, if neutrons are incident upon one region of the detector more than others, the 559 keV peak will be seen when this piece of cadmium is located there. Nine positions on the detector surface were tested in this experiment, and the positions and the respective boron photon count loss are illustrated in Figure 5.12. The non-uniformity of the boron photon distribution is appreciable. More photons are incident upon the

lower part of the detector, suggesting that the height of the detector is ~2 cm high. As expected, the 559 keV peak does not appear after the attachment of the cadmium patch at any of the nine positions. Therefore, it is concluded that there is not a particular region of the detector that sees a much higher neutron intensity than other locations.

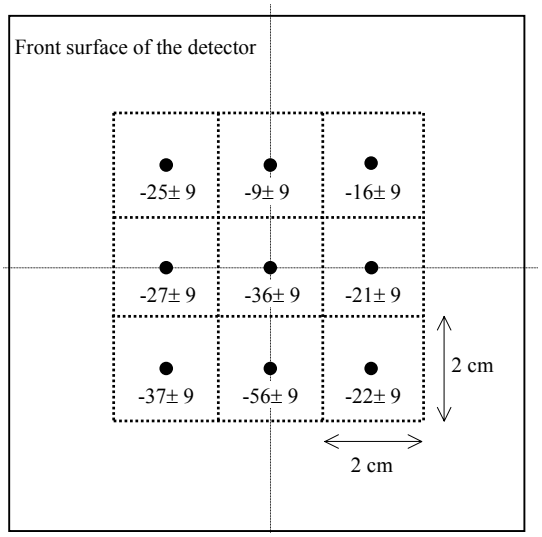

Figure 5.12 Illustrations of the nine positions for attachment of the Cd patch on the detector surface, and the corresponding boron photon loss after the attachment.

5.6 Further background reduction

5.6.1 Boronated polyethylene

It has been verified that neutrons incident on the front side of the detector contribute most of the background boron peak. In addition to those passing through the aperture in the shield, there could be neutrons penetrating through the front part of the detector shield. It was worthwhile to examine whether the addition of more neutron shielding material in front of the detector would further decrease the background count. Additional layers of boronated polyethylene, 10 cm or 20 cm thick, was tested, and the detected photon spectra are presented in Figure 5.13. The extra polyethylene is helpful in reducing the background count rate of the boron peak. The boron peak count rate drops from 292/s to 209/s with 10 cm of more polyethylene (a 28% reduction) and to 192/s with 20 cm of more polyethylene (a 34% reduction). More polyethylene (25 cm) was also tried, but no further improvement could be achieved.

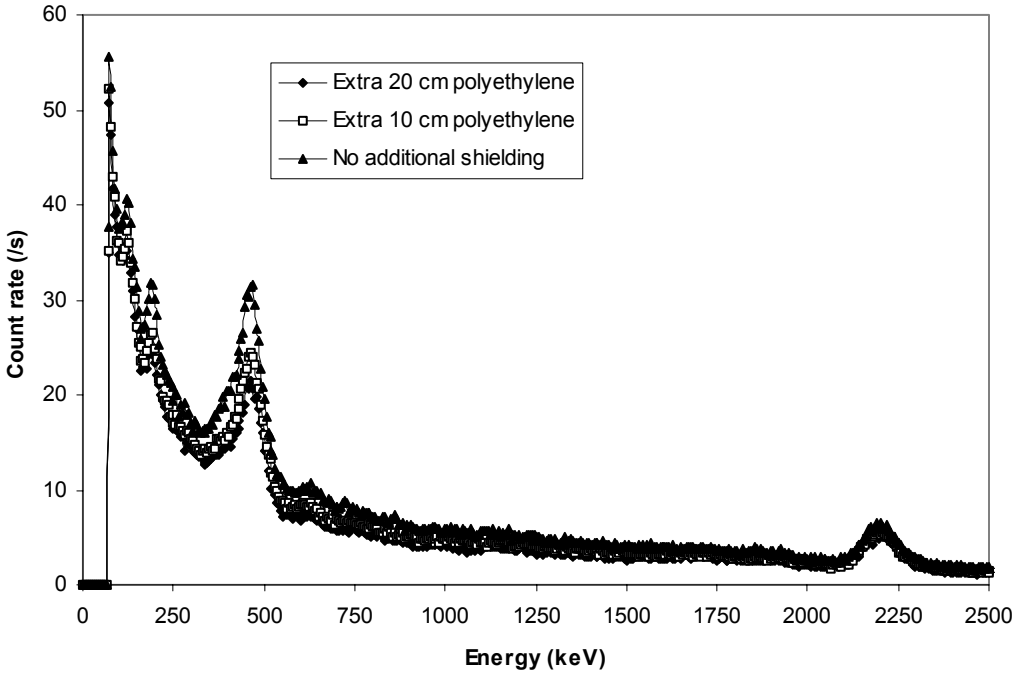

Figure 5.13 Photon spectra before and after the addition of additional boronated polyethylene in front of the detector.

5.6.2 Lithiated polyethylene

A thin layer of neutron absorber with a high thermal neutron absorption cross section reduces the number of thermal neutrons bombarding the detector without losing a significant number of boron photons. Cadmium was tested in the previous experiments, and the background boron peak in the measured photon spectrum was clearly reshaped. The thermal neutron capture cross section of cadmium is very high, and so the advantage of using cadmium is that this absorber layer can be very thin. Therefore, the loss of boron photons is not significant. However, there are also disadvantages. The absorption cross section of cadmium goes down very quickly as the neutron energy goes up, and therefore it is only effective in absorbing neutrons of very low energies. More importantly, the boron peak will be deformed and broadened because of the 559 keV photons emitted following neutron capture events in cadmium. A better choice is lithiated polyethylene. The effectiveness of lithiated polyethylene was demonstrated in simulations in Chapter 4. The 478 keV photons will not be significantly attenuated since this material mainly contains light elements. Another merit of lithium is that no photon will be emitted following the $^{6}Li(n,\alpha)^{3}H$ reaction.

Natural lithium contains 7.4% of ^{6}Li and 92.6% of ^{7}Li. In polyethylene used in this experiment, ^{6}Li was enriched to 93%. The weight ratio of ^{6}Li in this polyethylene is 12.8%, and the macroscopic cross section for thermal neutrons is 7.0 cm^{-1}. In Figure 5.14, the photon spectra, recorded after 6 mm or 12 mm of lithiated polyethylene was attached to the front surface of the detector, are compared with the original case with no lithiated polyethylene. The spectra demonstrate the effectiveness of the lithiated polyethylene in reducing the background under the boron peak. The boron peak count rate drops from 185/s to 148/s with 6 mm of polyethylene (a 20% reduction) and to 139/s with 12 mm of polyethylene (a 25% reduction). Compared to Figure 5.11 where cadmium is used, a significant difference is that the low energy contribution in the photon spectrum is not appreciably attenuated. This is because the photon attenuation coefficient of the light elements in lithiated polyethylene is much smaller than that of cadmium.

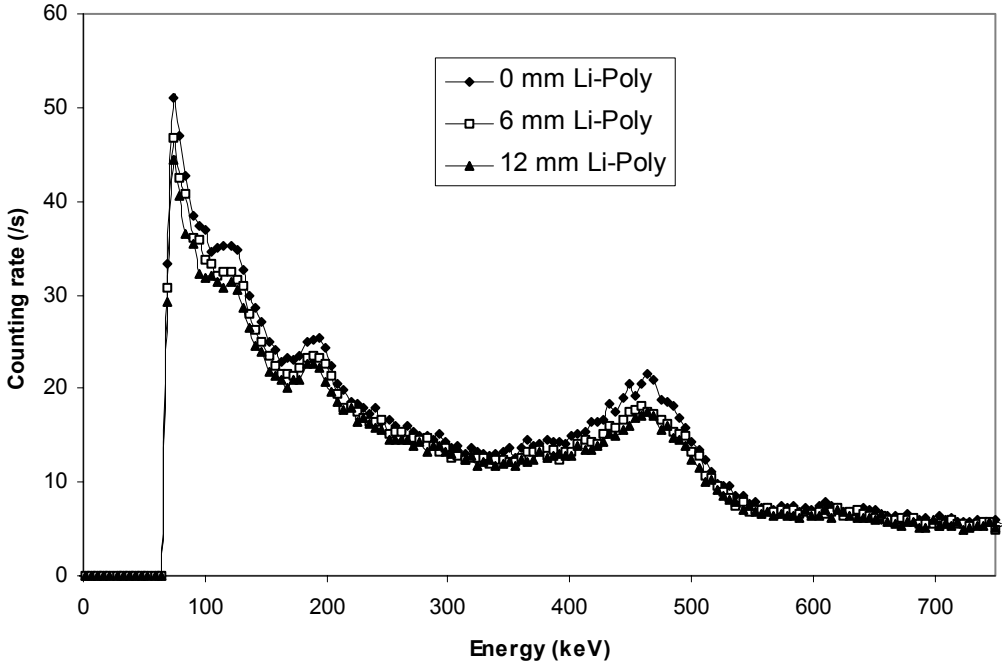

Figure 5.14 Photon spectra before and after the addition of a thin piece of lithiated polyethylene on the frond surface of the detector.

The final photon spectrum is shown in Figure 5.15, together with the spectrum in Figure 5.4. With the addition of more boronated polyethylene and a thin layer of lithiated polyethylene, the count rate of the background boron peak is decreased by about 50%. This is a significant improvement. However, without changing the size of the aperture in the collimator and/or sacrificing the count of boron photons, further

reductions in background will be very difficult. Another method to improve the signal to noise ratio is to increase the boron photon count, which will be discussed in Chapter 7.

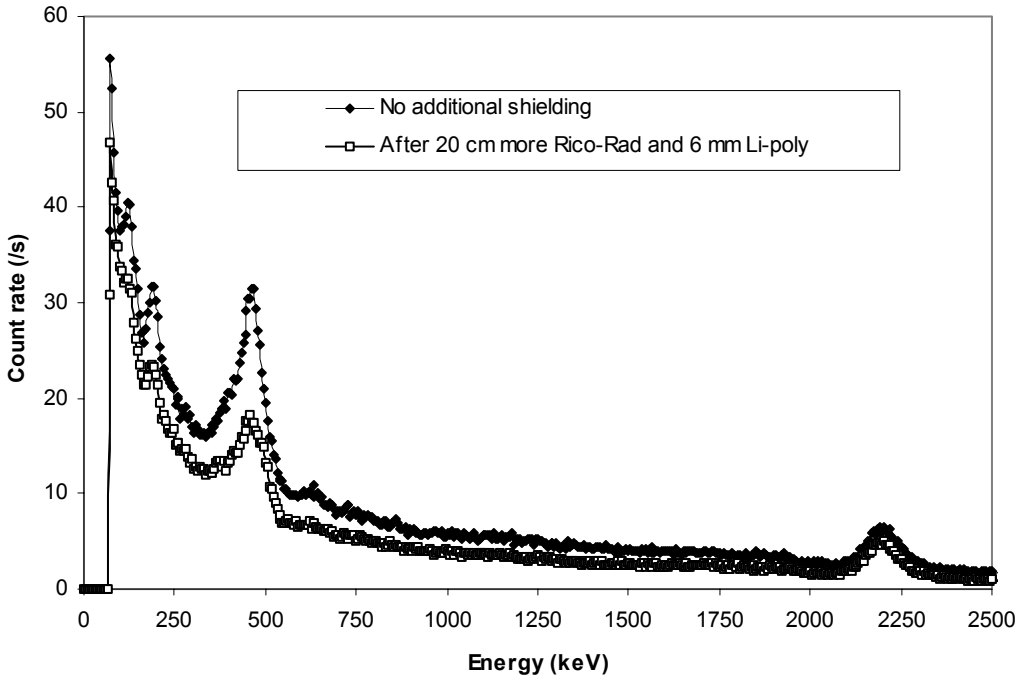

Figure 5.15 Photon spectra under the initial and the final shielding conditions.

5.7 Conclusions

Background reduction is a challenging task in developing the telescope system. The background count rate was reduced by several orders of magnitude with collimation and sufficient detector shielding.

Locating the photon detector inside the radiation vault is feasible, although a considerable amount of shielding material has been used. Fifteen centimeters of lead and twenty centimeters of boronated polyethylene are basically enough to suppress the background count to a negligible level on all sides of the detector except for the front side.

A background peak appears at the position of the boron peak in the photon spectrum measured with the NaI detector. Neutrons are mainly responsible for the formation of this peak, and the apertures in the collimator and the detector shield are the primary channels for the incoming neutrons. After the thickness of boronated polyethylene in front of the detector was doubled and a thin layer of lithium polyethylene was attached to the front surface of the detector, the count rate of the background boron peak was halved.

Further reductions in background are expected to be difficult without sacrificing the count rate of boron photons from the synovium.

Even with the existence of a background boron peak, boron photons from the synovium are readily detectable. More details on the detection of the boron photons from the synovium will be covered in Chapter 7 which describes experimental characterization of the telescope system.

Chapter 6 Background analysis of the boron peak

Neutron induced photon peaks were observed in the detected photon spectrum (133.6 keV and 203 keV peaks in Figure 5.16), even after the detector shielding had been optimized. This indicates the presence of a significant neutron field inside the NaI photon detector. The asymmetry of the background boron peak reveals that photons of at least two different energies are involved in the formation of this peak. It was verified experimentally in Chapter 5 that the primary source for this background peak is the photons emitted following neutron interactions inside the NaI(Tl) detector. In this chapter, the interaction processes of neutrons within NaI detectors are described first. Next, the potential photon contributors for this background peak are discussed, and the separate photon counts from these contributors are estimated with experiments, analytical deductions and Monte Carlo simulations. This estimation is for the original shielding condition (15 cm of lead and 20 cm of Rico-Rad), before the inclusion of additional 20 cm of Rico-Rad in front of the detector and a piece of 6 mm thick lithiated polyethylene adjacent to the front side of the detector (section 5.6). The reason is that Monte Carlo simulations were used in this process (section 6.5), and it was found that it was very hard to obtain reliable estimates of neutron-induced photon flux in the NaI crystal since the neutron flux at the detector location was much lower under the final shielding condition than under the original shielding condition. The results obtained for the initial shielding condition are still relevant to those for the final shielding condition, but the magnitudes of contributions will be different.

6.1 Neutrons interactions inside NaI detectors

The response of NaI crystals to neutron irradiation is complicated, and is strongly dependent on the neutron energy spectrum and the size/shape of NaI crystals[22-30]. Several types of neutron interactions, such as (n,n), (n,n′), (n,γ), (n,p), (n,α), and (n,2n), may take place inside NaI detectors[14]. Within the energy range of the BNCS neutron beam (< 6 MeV) at LABA, the dominant interactions are elastic scattering, inelastic scattering, and thermal neutron absorption[31]. Reactions with the emission of heavy charged particles (proton and alpha) are less important. For example, for ^{23}Na, the energy thresholds of (n,p) and (n,α) reactions are 3.76 MeV and 4.04 MeV, respectively. The influence of the three dominant processes ((n, n), (n, n′), and (n, γ)) is a function of their individual cross sections. For interactions of different particle types in NaI(Tl) crystals, scintillation efficiency must also be examined.

Among the three major interaction types, elastic scattering is the only one having an appreciable cross section across the entire energy range of the source neutrons[31]. The average neutron elastic scattering cross section is about five barns for both ^{23}Na and ^{127}I nuclei, hence the average macroscopic cross section is $\rho \cdot N_A \cdot (\sigma_{Na}+\sigma_I)/A$ = 3.67 (g/cm^3) × 6.02×10^{23}(/mol)× (2×5×10^{-24} cm^2) /150(g/mol) = 0.15 cm^{-1}. The

mean free path of neutrons in NaI crystals due to elastic scattering is 1/0.15= 6.7 cm. Therefore, for an incident neutron, multiple scattering may occur inside a crystal of 10.2 cm in diameter and 10.2 cm in length. The maximum energy transferred to a recoil nucleus in one elastic collision is $4A/(A+1)^2$ of the incident neutron energy, E_n, which is $0.16E_n$ or $0.03E_n$ for ^{23}Na or ^{127}I, respectively. To calculate the amplitude of the output signals arising from the energy deposited by heavy recoil nuclei in NaI crystals, the scintillation efficiency has to be taken into consideration. The light output response of NaI(Tl), which is stopping power dependent, is very different for photons (electrons) and heavy charged particles. The quenching factor, Q_f, is defined to measure the scintillation efficiency of heavy charged recoil nuclei relative to that of photons/electrons. The values of Q_f are 0.08 and 0.25 for ^{127}I and ^{23}Na, respectively[25,32]. In other words, one MeV kinetic energy deposited through ^{23}Na will generate a pulse with the same height as that for a 250 keV electron. For a 6 MeV neutron, the maximum energy transferred to a ^{23}Na or ^{127}I nucleus in one elastic scattering is 0.96 or 0.18 MeV, respectively, and, correspondingly, the output pulse appears at $0.96 \times 0.25 = 240$ keV for ^{23}Na and $0.18 \times 0.08 = 14.4$ keV for ^{127}I in the photon spectrum. Therefore, the neutron pulses generated through elastic scattering mainly accumulate at the low energy end of the photon spectrum, and the only effect on boron photon detection is from multiple scattering of fast neutrons on ^{23}Na. To produce a signal in the boron peak region via ^{23}Na nuclei, a neutron has to experience two elastic scattering events with the maximum energy transfer. (The pulse height will be equal to that for a 440 keV photon.) This possibility is expected to be very small, after considering the fraction of neutrons with energy above 6 MeV, the probability of maximum energy transfer events, and the mean free path of fast neutrons in NaI. Therefore, the count contribution via elastic scattering to the boron peak is expected to be negligible.

The kinetic energy of the incident neutrons can also be transferred to ^{23}Na or ^{127}I nuclei through inelastic scattering. The threshold for inelastic scattering is 440 keV for ^{23}Na or 57.6 keV for ^{127}I [31,33]. The inelastic scattering cross section of ^{23}Na and ^{127}I is smaller than that of elastic scattering in the energy range of zero to 6 MeV [31]. Therefore, the count contribution via inelastic scattering to the boron peak can also be neglected.

The energy deposited through recoil nuclei does not induce specific peaks in the photon spectrum, and hence these heavy nuclei cannot be the source of the background boron peak in the measured photon spectrum. The formation of the background peak is attributed to the photons released following neutron inelastic scattering and thermal neutron capture.

The photon pulses arising from neutron interactions with NaI crystals fall into two categories: prompt pulses that occur at the time of the interaction and delayed pulses that appear some time after the interaction[14]. Prompt photons come from both inelastic scattering(photon emission occurs when the excited ^{23}Na and ^{127}I nuclei decay to their ground states) and neutron absorption leading to $^{24}Na^*$ and $^{128}I^*$

nuclei which de-excite to the ground states via photon emission. Delayed photons are released during the decay of ^{24}Na and ^{128}I nuclei. ^{24}Na and ^{128}I are both beta-decaying isotopes, with half-lives of 25 minutes and 15 hours, respectively[33]. The intensity of the delayed photons is a function of time, because the number of ^{24}Na and ^{128}I nuclei in the NaI crystal increases during neutron exposure until saturation activity is reached.

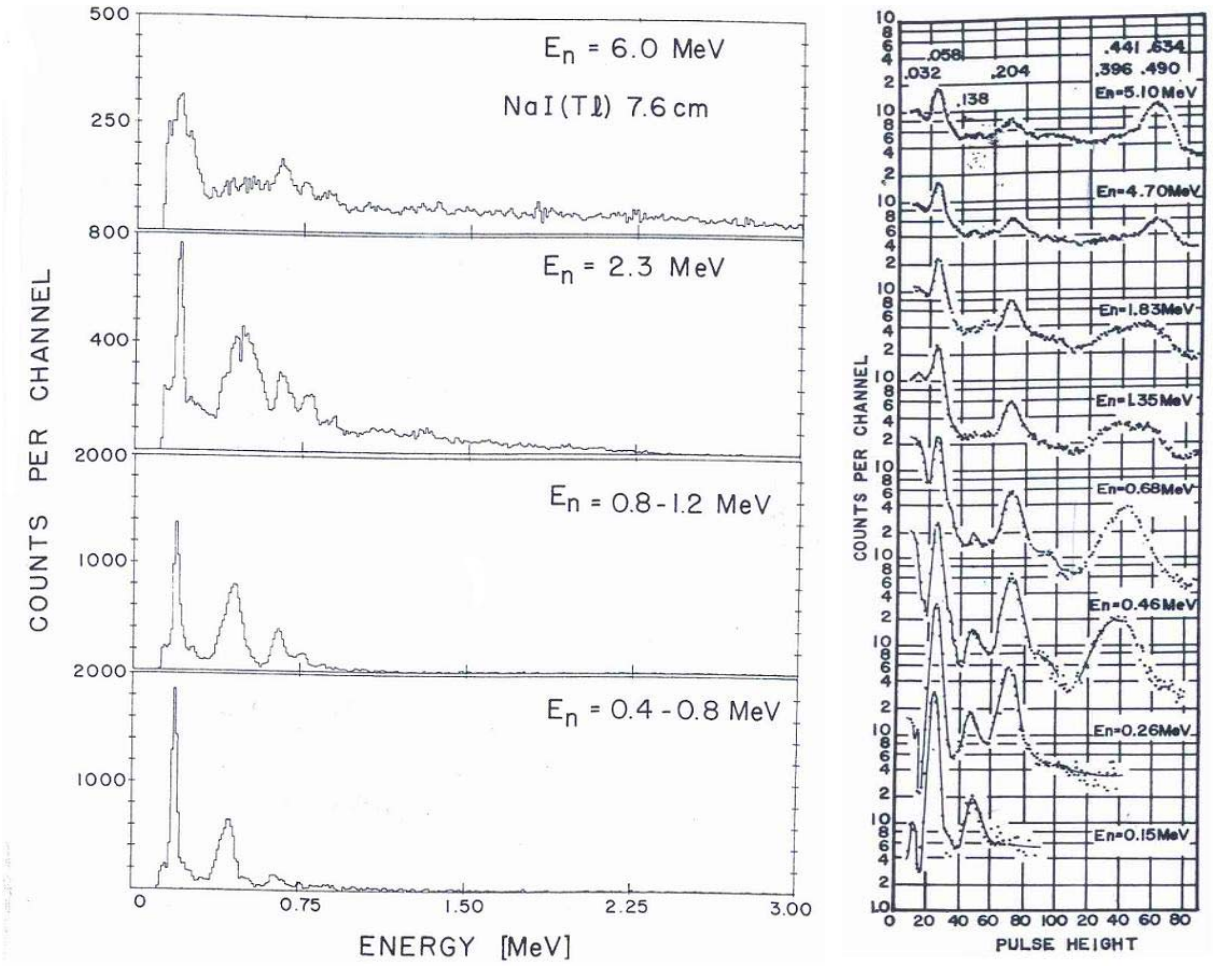

(a) (b)

Figure 6.1 Pulse height distribution arising from neutron interaction with 7.6 cm diameter × 7.6 cm long NaI(Tl) detectors (a) from Hausser et al.[22] and (b) from Inada [23].

The most intense photons originating from neutron interactions with ^{127}I include 57 keV and 202 keV photons from the ^{127}I(n,n′γ) reaction, and 30 keV and 137 keV photons from the ^{127}I(n,γ)^{128}I reaction [26,28.29]. The photon energy threshold of the multi-channel analyzer is set to be around 80 keV; therefore, the 30 keV and 57 keV photon peaks do not appear. However, the 137 keV and 202 keV peaks are very clear in the measured photon spectrum in Figure 5.4. The 137 keV and 202 keV peaks do not affect the

detection of the boron photons from the synovium, but the appearance of these two peaks confirms the existence of a neutron field in the detector. We are more interested in those photons related to the formation of the background boron peak. Figure 6.1(a) and Figure 6.1(b), taken from the research work of Hausser[22] and Inada[23], present the photon spectra measured with NaI detectors under irradiation by neutrons of various energies. In both figures, a broad peak appears at ~450 keV, which unfortunately overlaps with the boron peak. Hausser speculated that this peak contains a strong component of 440 keV photons following neutron inelastic scattering on ^{23}Na.

In addition to interactions with the NaI crystal, neutrons can be absorbed and scattered in the aluminum can sealing the NaI crystal and the photo multiplier tube. A 472.6 keV photon is emitted through the ^{27}Al(n,α)^{24}Na reaction. However, this contribution is negligible since its cross section is much smaller than the absorption cross section of ^{127}I. The shell of the photomultiplier tube (PMT) is made of borosilicate glass containing ^{10}B. The boron photons released from the PM tube can interfere with the detection of boron photons from the synovium. This contribution will be evaluated in section 6.5.

6.2 Photon contributions to the background boron peak

For the gamma ray telescope at Petten, the 511 keV annihilation peak is the only noticeable feature that could affect the detection of boron photons with the exception of the Compton plateau. However, for the telescope system at LABA, the situation is more complicated due to the relatively poor energy resolutions of the NaI photon detector. One experiment was specifically designed to examine the contribution from 511 keV photons to the boron peak. In this experiment, a positron emitter, ^{22}Na, was used as the 511 keV photon source, and there was 0 ppm boron in the synovium phantom. The experiment was performed in three steps. First, an energy spectrum was taken under normal irradiation conditions (an accelerator beam current of 100 μA), in which case the background boron peak was observed. Next, with the accelerator off, a second spectrum was taken with the ^{22}Na source, placed in air, in front of the aperture. A sharp 511 keV peak was observed this time. Care was taken to position the ^{22}Na source at a distance from the detector that rendered the count rate in the peak channel similar to that in the peak channel in the previous step. In the third step, maintaining the same distance between the ^{22}Na source and the detector, the accelerator beam was turned on, and a third spectrum was taken. A new peak appeared in this spectrum, which was the combination of the two peaks in the previous two steps. The three spectra are presented together in Figure 6.2. The peak channels in the three spectra are all different, and the peak channel in the third spectrum is between those in first and second spectra. This result implies the existence of other photons in addition to 511 keV photons that act in forming this background boron peak.

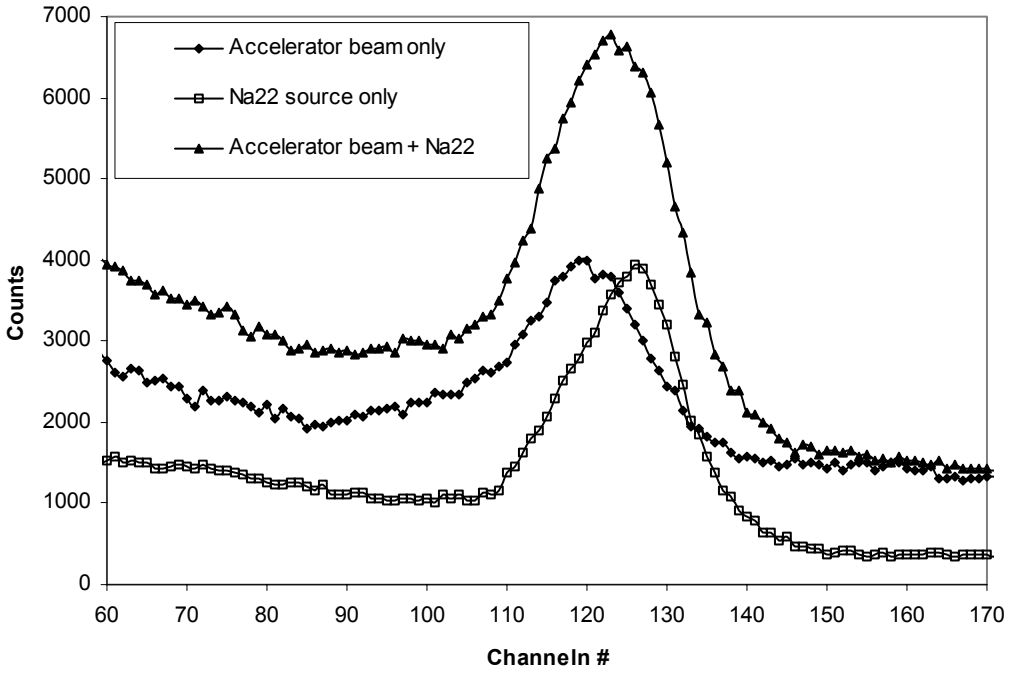

Figure 6.2 Illustration of a different peak channel of the background "boron" peak from that of the 511 keV annihilation peak.

The FWHM of the NaI detector used in the telescope was estimated to be 41.7 keV at 478 keV. Because of the Doppler effect, the actual energy of the emitted boron photons falls into an energy bin of 470 to 485 keV instead of a single 478 keV line. With the help of *Matlab*, the FWHM of this broadened peak is estimated to be about 44 keV. However, the measured FWHM of the background boron peak is 70 keV, which indicates again that this background peak is not simply formed by 478 keV boron photons alone.

In Figure 5.4, the background peak extends from 360 keV to 560 keV. Here, we use FWTM (full width at tenth-maximum) to represent the width of a photon peak. For photon peaks with a Gaussian shape, FWTM is 1.8 times larger than FWHM. Therefore, FWTM can be estimated using the relation for FWHM calculation (section 5.1.2), and the value is 65 keV at 360 keV and 81 keV at 560 keV, respectively. Therefore, this background peak is primarily formed with photons in the energy range of 400 keV to 520 keV. There are several photons that are generated in this energy range[21,31,33], which can be organized into two categories: photons emitted outside the NaI detector and photons induced by neutrons inside the NaI detector. The first category includes:

- 478 keV photons from boronated polyethylene, and
- 511 keV annihilation photons created outside the detector.

The following belong to the second category:

- 478 keV photons from ^{10}B contained in the PM tube,
- 511 keV annihilation photons created inside the detector,
- 443 keV photons from neutron capture in ^{127}I,
- 472 keV photons from neutron capture in ^{23}Na,
- 440 keV photons from inelastic neutron scattering on ^{23}Na, and
- 418 keV photons from inelastic neutron scattering on ^{127}I.

In the following sections, the separate count contributions from the photons listed above are explored. The analysis is conducted for the detector shield (15 cm of lead and 20 cm of Rico-Rad on all sides of the detector) before the additional boronated polyethylene and lithium polyethylene were added (see section 5.6), and the overall count rate of the background peak is 280 counts/s.

6.3 Direct Photon contribution

The count of 478 keV boron photons and 511 keV annihilation photons generated outside the NaI detector is an unavoidable source of background in the boron peak. Boronated polyethylene (Rico-Rad) is used widely as the neutron moderation and shielding material in the telescope system. The total number of 478 keV photons produced in all of the boronated polyethylene in the radiation vault is very large, but the number of photons that can be actually detected is limited since the detector is surrounded with 15 cm of lead. Except for the aperture, in practice, only those boron photons emitted by boronated polyethylene surrounding the aperture and then entering the aperture in the direction of the detector have the possibility of being detected. The situation for 511 keV photons is a little more complicated. In addition to the shielding material around the aperture, the detected 511 keV photons can also be from any place in the viewing region of the detector as well as from the lead shield surrounding the detector.

A 5 cm thick lead brick was positioned directly in front of the NaI detector, behind the shield, to investigate the combined contribution from boron photons and annihilation photons. This thickness of lead is enough to stop essentially all 478 keV and 511 keV photons. The result was a reduction in the background peak count of about 1/4, or 70 counts/s. However, lead also attenuates neutrons, especially thermal neutrons. For instance, for 1 eV neutrons, the probability of successfully passing through 5 cm of lead is about 40%. Thus, this piece of lead changes the fluence as well as the energy spectrum of neutrons irradiating the detector. Therefore, only a part of the reduction in count (70 counts/s) can be attributed to attenuation of 478 keV and 511 keV photons. Compared to the total 280 counts /s, the photon contribution is less significant than the contribution of neutron-based interactions.

There could be a way to roughly determine the sole photon contribution. Instead of trying to stop all 478 keV and 511 keV photons, several thin lead sheets would be chosen. For example, three lead sheets

with a thickness of 1 mm would be attached to the front surface of the detector. Respectively, 18 %, 33% and 45% of the 478 keV photons would be attenuated after penetrating one, two and three pieces of these lead sheets. On the other hand, these thin lead sheets are almost transparent to neutrons. If the decrease of the boron peak count could be measured with enough reliability as the thickness of lead increases, an estimation of the photon contribution could be obtained from the curve of the background peak count versus the thickness of lead. This approach was not evaluated experimentally.

6.4 Photon count from (n,γ) reactions inside the NaI crystal

6.4.1 443 keV photons from neutron capture in iodine

There are at least two approaches for roughly estimating the count rate of 443 keV photons from neutron capture in ^{127}I. We can either utilize the property of the capture product ^{128}I, or make use of other photon peaks visible in the photon spectrum. The details of the two approach are described as follows.

6.4.1.1 Estimation of 443 keV photon count rate with ^{128}I

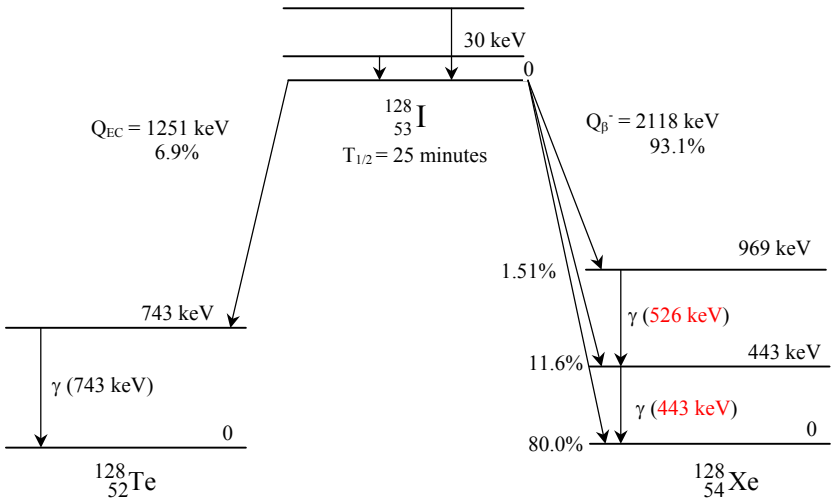

Figure 6.3 Decay scheme of ^{128}I.

Iodine 128 is a beta-emitting isotope with a half-life of 25 minutes and decays as follows[31,33]:

$$^{128}\mathrm{I} \rightarrow {}^{128}\mathrm{Xe} + \mathrm{e}^- + \bar{\nu} + 2.119\ \mathrm{MeV} \quad (93.1\%) \quad \text{or}$$

$$^{128}\mathrm{I} + \mathrm{e}^- \rightarrow {}^{128}\mathrm{Te} + \nu + 1.252\ \mathrm{MeV} \quad (6.9\%)\ .$$

The decay scheme of ^{128}I is illustrated in Figure 6.3. Electrons are released in 93.1% of ^{128}I decays through three channels to three different energy levels of ^{128}Xe. The maximum energy of the electrons is

2.119 MeV. A NaI crystal can also function as a good electron sensor. The energy of these electrons is absorbed locally inside the crystal because the range of these electrons is very short in solid materials. Therefore, the detection efficiency of these electrons is almost 100%. Since the scintillation efficiency of NaI crystals is the same for electrons and photons, the detected beta particles appear from 0 to 2.119 MeV in the photon spectrum. The heavy nuclei (^{128}Xe and ^{128}Te) carry only a very small fraction of energy released in beta decays, and their energy deposition in NaI crystal can be ignored.

The 443 keV photon does not correspond to the energy difference of two energy levels of ^{128}I; in fact, it is released when a ^{128}Xe nucleus de-excites from its first excited state to its ground state. The emission intensity of the 443 keV photon is about 0.13 per ^{128}I decay. Since the half-life of ^{128}I is 25 minutes, this 443 keV photon belongs to the category of delayed photons. The ^{128}I nuclei are produced via neutron absorption in ^{127}I, and are consumed through beta decay. Their number changes with neutron irradiation until a dynamic equilibrium is reached. The production rate of ^{128}I inside the NaI crystal equals $\Phi \cdot \Sigma \cdot V$, where Φ is the average thermal neutron flux in the crystal, Σ is the thermal neutron absorption cross section of ^{127}I, and V is the volume of the crystal. The decay rate of ^{128}I is $\lambda \cdot N$, where λ is the decay constant of ^{128}I, and N is the total number of ^{128}I nuclei in the crystal. The expression for N is

$$N = \frac{\Sigma \cdot \Phi \cdot V}{\lambda}(1 - e^{-\lambda t}) \ .$$

At equilibrium, the production rate is equal to the decay rate, i.e., $\Phi \cdot \Sigma \cdot V = \lambda \cdot N$. Since the half-life of ^{128}I is 25 minutes, the equilibrium will be reached in about 1 hour (2-3 times $T_{1/2}$). The background contribution of ^{128}I to the boron peak comes from two components: β particles and 443 keV photons. Since the decay rate of ^{128}I changes with time, the background count rate from ^{128}I is also time dependent. At the time when the irradiation starts, the count rate from ^{128}I is zero; at 1 minute, 5 minutes, 10 minutes, and 20 minutes, the background count rate from ^{128}I is 0.03, 0.13, 0.24, and 0.43 of the saturation activity, respectively.

The influence from ^{128}I can be evaluated by its saturated decay rate, and the approach to estimate the saturated decay rate is the following: first, the NaI detector is irradiated with the accelerator neutron beam for one hour or so to saturate the concentration of ^{128}I in the crystal; then the irradiation is stopped, and the multi-channel analyzer is started to record the spectrum, which should be in the shape of a continuous beta spectrum with a maximum energy of 2.119 MeV. Figure 6.4 shows the spectra recorded after the detector was bombarded 10 to 60 minutes. The beam current was set to be 20 μA, and the collection time was 5 minutes. The shape of a beta spectrum is very clear in Figure 6.4, but the 443 keV photon peak is

not easily recognizable. The trend of saturation becomes more and more apparent over time, and all the spectra converge at the maximum energy of 2.1 MeV, as expected.

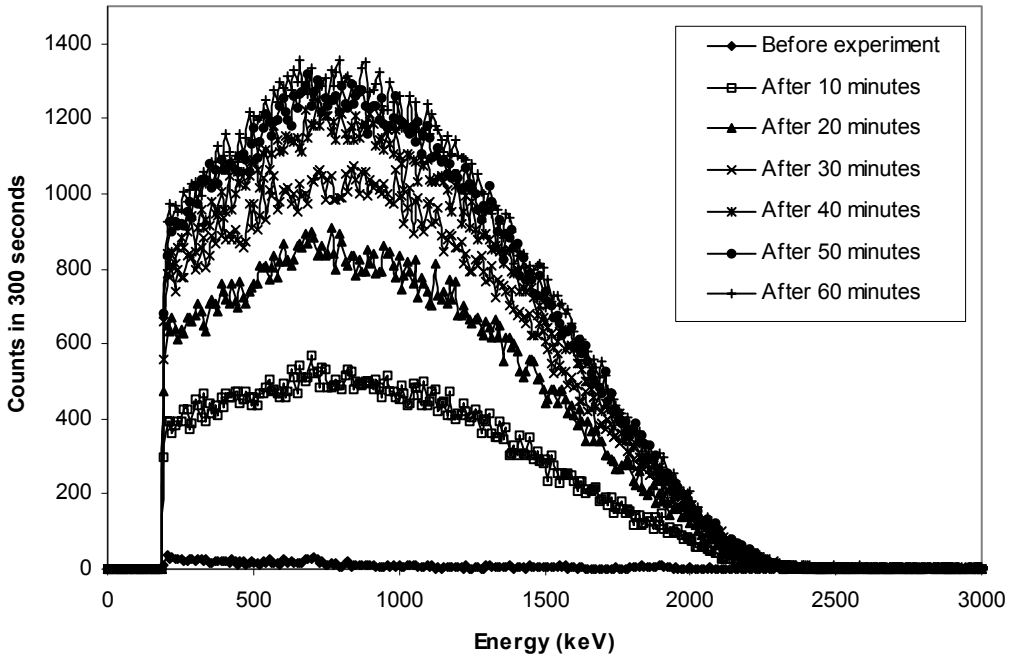

Figure 6.4 Energy spectra by the NaI detector after 10 to 60 minutes of neutron bombardment.

The saturated count rate of beta particles C_1 can be estimated as the total count per second in the spectrum (the count from 443 keV photons is neglected), which is proportional to the production rate of ^{128}I, C_2 ($C_2 = C_1/0.931$). The emission rate of 443 keV photons equals the production rate of ^{128}I C_2 times the absolute intensity (normalized to per absorption) of 443 keV photons (13%). Another factor to be considered is the full energy detection efficiency η_1 of the 10.2 cm × 10.2 cm crystal to 443 keV photons, which was obtained via Monte Carlo simulations. In simulations, the 10.2 cm × 10.2 cm NaI crystal was modeled, and then 443 keV photons were sampled uniformly inside the volume of the crystal. The full energy detection efficiency was the normalized number of 443 keV photons that deposit all their energy inside the crystal. Then, the estimated detection rate of 443 keV photons is $C_1/0.931\times 0.13\times\eta_1$.

The count rate C_1 estimated from the spectrum taken after 60 minutes of irradiation is about 600/s (at 100 μA of the beam current). The efficiency η_1 is 0.523, so the estimated saturated count rate of 443 keV photons is $600/0.931\times0.13\times0.523 = 44$ counts/s. After 10 minutes (close to the BNCS treatment time) of

neutron irradiation, the count rate of 443 keV photons is about 44×0.24 = 11 counts/s at 100 μA, or 110 counts/s at 1mA.

6.4.1.2 Estimation of 443 keV photon count rate with the 137 keV peak

Another method for estimating the production rate of ^{128}I relies on the photon peak formed by 137 keV photons. The 137 keV photon is the most intensive photon emission following neutron absorption in ^{127}I (0.0843 per iodine neutron capture[21]). A 137 keV peak is easily recognizable in the photon spectrum, and so the count rate of 137 keV photons can be directly determined from the spectrum. The full energy detection efficiency of the specific NaI crystal to 137 keV photons is estimated to be 0.94 via MCNP simulations. The peak count rate of 137 keV photons is about 40 counts per second, hence the production rate of ^{128}I is (40/0.94)/0.0843 = 505 /s. This number is about 16% lower than the estimation using the method described in the preceding section (600 /s). The difference could be partially attributed to the uncertainties in the estimates and partially attributed to the fact that in the previous approach other possible contributions such as the count of 443 keV photons are also included in the total count rate of 600 counts/s. With this newly estimated ^{128}I count rate, the count rate of 443 keV photons will be 505/0.931×0.13×0.523×0.24 = 9 counts/s after 10 minutes of neutron irradiation with a beam current of 100 μA.

6.4.2 472 keV photons from neutron capture in sodium

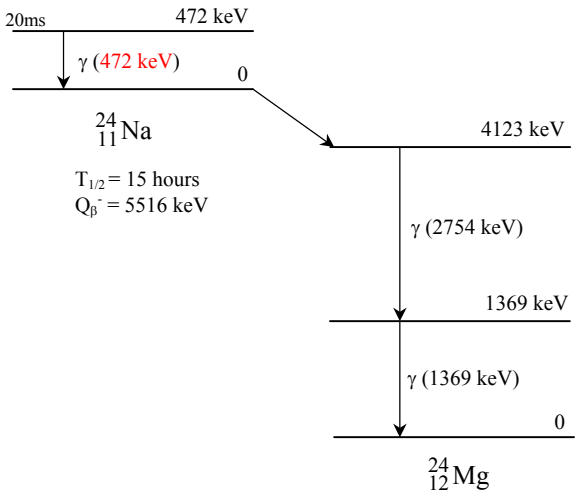

Figure 6.5 Decay scheme of ^{24}Na.

^{24}Na produced via neutron capture events in ^{23}Na is a beta-emitting isotope ($^{24}\text{Na} \rightarrow {}^{24}\text{Mg} + e^- + \bar{\nu}$) with a half-life of 15 hours[31,33]. The decay scheme of ^{24}Na is shown in Figure 6.5. The Q value of ^{24}Na beta decay is 5.516 MeV; however, because the decay product ^{24}Mg is initially at its second excited state (energy level: 4.123 MeV), the maximum energy of the beta particles emitted from ^{24}Na is 1.391 MeV. Two photons (2.754 MeV and 1.369 MeV) are released when the excited ^{24}Na nucleus returns to its ground state. Different from the 443 keV photon following iodine neutron capture, the 472 keV photon is not from the decay product, but is released promptly when the excited ^{24}Na nucleus jumps from its first excited state to its ground state (the half-life of the 472 keV energy level is 20.2 ms, and is called a meta state). Therefore, the intensity of 443 keV photons is not time dependent.

It is not plausible to estimate the count rate of 472 keV photons using the same methods for 443 keV photons. The half-life of ^{24}Na is too long for building up a saturation level in the NaI crystal in a reasonable time. Moreover, there is not another photon peak from sodium clearly visible in the measured photon spectrum. A way to estimate the count rate of 473 keV photons is to utilize the 137 keV peak from iodine neutron capture again. The emission intensity of 137 keV photons is 8.43% per iodine neutron capture, and that of 472 keV photons is 59.83% per sodium neutron capture. In the 10.2 cm × 10.2 cm NaI crystal, the detection efficiency of the two energies is 0.94 and 0.50, respectively, based on the assumption of a uniform production. The 472 keV photon production cross section of ^{23}Na is 0.4 barn, and the thermal neutron capture cross section of ^{127}I is 6.2 barns. Therefore, the count ratio of 472 keV photons to 443 keV photons can be approximated as

$$\frac{\sigma(472\text{ keV}) \cdot (\text{detection efficiency of 472 keV photons})}{\sigma(\gamma) \cdot (\text{intensity of 137 keV photons}) \cdot (\text{detection efficiency of 137 keV photons})}$$

$$= \frac{0.4}{6.2 \times 0.0843} \times \frac{0.5}{0.94} = 0.4$$

The count rate of 137 keV photons is about 40 /s, therefore, the estimated count rate of 472 keV photons is about 0.4× 40 counts/s ~ 16 counts/s.

There arises another problem here. In analyzing the contribution of 443 keV photons from iodine previously (section 6.4.1), it was assumed that after the neutron beam is turned off the detected spectrum is formed by beta particles from ^{128}I. Since ^{24}Na is also a beta-decaying isotope, we have to determine whether the spectrum above includes a significant contribution from beta particles emitted from ^{24}Na. The rate of change of ^{128}I or ^{24}Na nuclei equals its production rate minus its decay rate, i.e.,

$$\frac{dN}{dt} = \Sigma \cdot \Phi \cdot V - \lambda \cdot N .$$

The solution of the differential equation is

$$N = \frac{\Sigma \cdot \Phi \cdot V}{\lambda}(1 - e^{-\lambda t}) \ .$$

The emission rate of beta particles equals the beta decay rate of ^{128}I or ^{24}Na, i.e., $(\lambda N)\cdot$(branching ratio of beta emission). Therefore, the ratio of the beta count rate of ^{24}Na to that of ^{128}I is

$$\frac{(\lambda N)_{Na}}{(\lambda N)_I \times 0.931} = \frac{\sigma_{Na}}{\sigma_I}\frac{1 - e^{-\lambda_{Na} \cdot t}}{1 - e^{-\lambda_I \cdot t}}\frac{1}{0.931}$$

Substitute $\sigma_{Na}/\sigma_I \sim 1/13$, $\lambda_{Na} = \ln 2/T_{1/2} = \ln 2/15 = 0.0462/h$, $\lambda_I = \ln 2/0.417 = 1.662/h$, and $t = 1$ hour into the expression above, and the ratio becomes:

$$\frac{1}{13} \times \frac{1 - e^{-0.0462 \times 1}}{1 - e^{-1.662 \times 1}}\ \frac{1}{0.931} = \frac{1}{13} \times \frac{0.045}{0.810} \times \frac{1}{0.931} = 0.005 \ .$$

So the contribution from ^{24}Na is very small and can be ignored.

In principle, the beta contribution from ^{24}Na could also be estimated experimentally. Several hours after the accelerator beam is turned off, almost all ^{128}I nuclei have decayed. (For example, after 5 hours, only 0.001 of ^{128}I nuclei remains). Therefore, the detected pulses inside the crystal will be from the decay products of ^{24}Na, which include beta particles with a maximum energy of 1.39 MeV and two separate gamma rays with energies of 2754 keV and 1369 keV. However, this approach is impractical to implement because the beam current has to be large and the irradiation time has to be long to achieve an appreciable count rate of the ^{24}Na decay products.

6.5 Photon counts from other neutron reactions inside the detector

In addition to (n,γ) reactions, neutron-induced photons appear in the boron peak via three other types of reactions: (n, n′γ), pair production, and ^{10}B(n,α) in the PMT. These reactions are described first, and their individual count contribution to the boron peak will be estimated in section 6.5.4.

6.5.1 (n,n′γ) photons

The two most intense photon emissions from neutron inelastic scattering are 440 keV photons from sodium and 418 keV photons from iodine[31,33]. A 440 keV photon is emitted when a sodium nucleus de-excites from its first excited state to the ground state, and this is the only possible photon energy between 400 to 500 keV that an excited ^{23}Na nucleus can emit. The 418 keV photon is released from the fourth energy level of iodine to its ground state. For iodine, there is another possibility of emitting a 430 keV photon. However, since the ^{127}I nuclei have to be excited to an energy level of 2.976 MeV, the possibility is very small in the energy range of the BNCS neutron beam.

6.5.2 511 keV annihilation photons

In addition to being generated outside the detector, 511 keV annihilation photons can also be created inside the NaI crystal following pair production of neutron-induced photons with energies greater than 1.022 MeV. This contribution is important since (n,γ) reactions in both ^{23}Na and ^{127}I generate photons with energies above the threshold of pair production. On average, ~2 photons with energy above 1.022 MeV are released per sodium neutron absorption, and the number for iodine is ~0.2. Since the thermal neutron absorption cross section of iodine is one order of magnitude higher than that of sodium, the numbers of high energy photons emitted from sodium and iodine neutron captures are comparable.

6.5.3 478 keV photons from ^{10}B contained in PM tube

The encapsulation shell of the PM tube associated with the photon detector is made of borosilicate glass containing ^{10}B. Borosilicate glass is composed of SiO_2 (80.2%), Al_2O_3 (2.3%), B_2O_3 (13.4%), and Na_2O (4.1%)[34]. (Some minor impurities are neglected.) The weight fraction of ^{10}B is 0.0083, or 8,300 ppm. This boron concentration is high, and is within the range of the synovial boron concentration. Since the PMT tube neighbors the NaI crystal, boron photons emitted from borosilicate glass have a much higher detection probability than those from the synovium. However, after shielding, the neutron flux in borosilicate glass is several orders of magnitude lower than that in the synovium, and hence only a small number of ^{10}B(n,α) reactions occur in it. Here, a very rough estimation is conducted by comparing the production of 472 keV photons through sodium neutron capture with the boron photon emission rate in borosilicate glass. The dimensions of the PMT tube are 10 cm in length, 5 cm in diameter, and 0.05 cm in thickness. Therefore, the total volume of borosilicate glass is 9.7 cm^3. The density of borosilicate glass is 2.22 g/cm^3, hence the total mass of ^{10}B is 9.7×2.22×0.0083 = 0.18 g. The ratio of the emission of boron photons to that of 472 keV photons is

$$\frac{\sigma(^{10}\mathrm{B(n,\alpha)})\cdot \mathrm{N}(^{10}\mathrm{B})\cdot \Phi\,(\mathrm{PMT})\times 0.93}{\sigma(472\mathrm{keV\ photon})\cdot \mathrm{N}(^{23}\mathrm{Na})\cdot \Phi(\mathrm{NaI})} = \frac{3840\mathrm{b}\times 0.18/10\times \Phi\,(\mathrm{PMT})\times 0.93}{0.4\mathrm{b}\times(3.67\mathrm{g/cm^3}\times\pi\times 5^2\times 10\mathrm{cm^3})/150\times\Phi(\mathrm{NaI})}$$

$$= \frac{3840\mathrm{b}\times 0.18/10\times \Phi\,(\mathrm{PMT})\times 0.93}{0.4\mathrm{b}\times(3.67\mathrm{g/cm^3}\times\pi\times 5^2\times 10\mathrm{cm^3})/150\times\Phi(\mathrm{NaI})}$$

$$= 8\times\frac{\Phi\,(\mathrm{PMT})}{\Phi(\mathrm{NaI})}.$$

The average neutron flux in borosilicate glass is expected to be appreciably lower than that in the NaI crystal since after arriving at the front surface of the detector neutrons are attenuated inside the NaI crystal before reaching the PMT, and the detection probability of boron photons is also smaller than that of 472 keV photons since the 472 keV photons are released inside the NaI crystal and the 478 keV

photons outside it. Consequently, the count rate of boron photons from the PMT could be comparable to that of 472 keV photons, but cannot be the primary source of the background boron peak.

6.5.4 Monte Carlo estimation

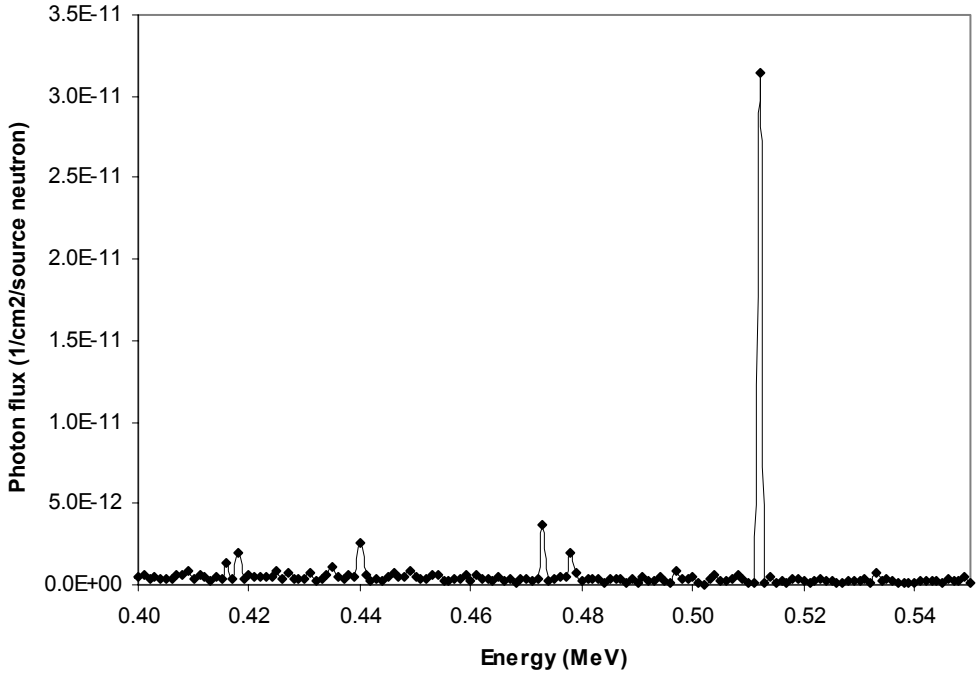

Figure 6.6 Neutron induced photon flux in the NaI crystal.

There is not a simple analytical or experimental way to estimate the separate photon counts from the sources describe above. Therefore, Monte Carlo simulations, based on the transport model shown in Figure 5.3, were performed. Because of computational inefficiency, the simulation was divided into two consecutive steps. In the first step, only neutrons were transported and the outcome of this step was a surface source file that recorded the information of all neutrons striking the front surface of the NaI crystal; in the second step, all neutrons in the surface source file were started on the crystal surface, and photons produced in the NaI crystal, the PMT and surrounding shielding materials were tracked and tallied. The F8 tally (pulse height tally) might have been used; however, it was impractical since when generating the neutron surface source, variance reduction methods had to be applied to improve the counting efficiency. The chosen tally was F4, which was used for estimating the average photon flux in the NaI crystal. Figure 6.6 presents the tallied photon flux spectrum, in which the 418 keV, 440 keV, 472

keV, 478 keV and 511 keV peaks are all recognizable. In particular, the 511 keV peak is very prominent. Different from that mentioned in section 6.3, this 511 keV peak is formed by annihilation photons emitted inside the NaI crystal. As expected, the 443 keV photon peak from $^{127}I(n,\gamma)$ is not observed, since MCNP only tracks prompt gamma rays.

An issue involved in count estimation is to determine the flux-to-count conversion factor, which is required to convert the photon fluxes tallied in MCNP simulations to corresponding photon counts. The count rate of 472 keV photons has been estimated in section 6.4.1.2 to be around 16 counts per second at 100μA, and this 472 keV peak also appears in Figure 6.6. This conversion factor can be obtained based on the 472 keV photons, and explicitly it is expressed as the ratio of the count rate of the 472 keV photon peak to its simulated flux. The individual count of 418 keV, 440 keV, 478 keV or 511 keV photons is estimated as (flux of a specific photon energy × flux-to-count conversion factor × detection efficiency of this specific energy/ detection efficiency of 472 keV).

The neutron fluxes are 2.0×10^{-12}/cm^2/source neutron for 418 keV photons, 2.6×10^{-12}/cm^2/source neutron for 440 keV photons, 3.6×10^{-12}/cm^2/source neutron for 472 keV photons, 1.9×10^{-12}/cm^2/source neutron for 478 keV photons, and 3.1×10^{-11}/cm^2/source neutron for 511 keV photons. The detection efficiencies of these photons in the NaI crystal are 0.544, 0.523, 0.494, 0.489, and 0.463 for 418 keV, 440 keV, 472 keV, 478 keV and 511 keV photons, respectively. The flux-to-count conversion factor is (16/s)/(3.6×10^{-12}/cm^2/source neutron) = 4.44×10^{12} (cm^2·source neutron) /s. Therefore, the count rates of these photons are 10 counts/s for 418 keV photons, 12 counts/s for 440 keV photons, 8 counts/s for 478 keV photons, and 129 counts/s for 511 keV photons. Consequently, the total count rate of prompt photons (418 keV, 440 keV, 472 keV, 478 keV, and 511 keV) is 185 counts/s. After the contribution from delayed photons (443 keV) is added, the total count rate of neutron-induced photons in the NaI detector is around 200 counts/s.

This estimated count rate is a little lower than the actual count rate since after including the count (< 70 counts/s) from direct photon contribution (boron photons and annihilation photons generated outside the detector, section 6.3), the estimated count rate of the background boron peak is still lower than that measured in experiments (280 counts/s). This is not a surprise after realizing the statistical uncertainties and approximations involved in this entire process. On the other hand, for the purpose of giving a rough picture of the compositions of the background peak, the estimation is already good enough. In Figure 5.4, the background peak covers an energy interval of 200 keV (360 keV to 560 keV); however, the peak channel is not at the central energy (460 keV), but shifted to ~480 keV. This is certainly because of the important contribution from 511 keV photons. Compared to 511 keV photons, the intensities of the

photons at the low energy part of the background peak are much weaker, which explains the long tail at the left side of the peak.

6.6 Conclusions

The fast neutrons mixed in the BNCS neutron beam make the neutron-induced photon signals unavoidable. One disadvantage of using a NaI detector is that by chance photons of several energies are emitted inside the NaI crystal. Several photons, which can be prompt or delayed, are too close to 478 keV to be fully separated from the boron peak. In addition, because of the poor energy resolution of NaI detectors, more photon peaks such as the 418 keV peak are involved in the formation of the background peak.

The count of 511 keV annihilation photons is still the most influential contribution to the background peak. The majority of these annihilation photons are generated inside the NaI crystal. In spite of the high boron concentration in borosilicate glass, the production of boron photons in it is significantly reduced with the help of detector shielding. As a result, the boron photon contribution from the photomultiplier tube is very limited. The presence of ^{128}I inside the NaI crystal causes additional uncertainty in detecting the boron photons from the synovium. The intensity of 443 keV photons and beta particles (E_{max}= 2.1 MeV) vary with time before saturation activity equilibrium is reached. However, the impact can be small, since the treatment time in BNCS is expected to be short and hence the decay rate of ^{128}I low.

Chapter 7 Experimental characterization of the telescope system

In the previous two chapters, installation of the telescope system was discussed, and special attention was paid to analysis and reduction of the background under the boron peak. Although a background boron peak still exists after collimation and shielding, the feasibility of detecting the boron photons from the synovium was confirmed. In this chapter, experimental characterization of the performance of the telescope system is presented. The count rate of boron photons under various boron concentrations and different configurations of the synovium phantom is investigated via both simulation and experiment. Comparisons between experimental results and simulation results are made, and the conclusions and predictions from Monte Carlo simulations are validated.

7.1 Boron photon detection

The arrangement illustrated in Figure 5.3 is used in experiments to characterize the performance of the telescope system. The anthropomorphic phantom is composed of two water-filled uncovered plastic boxes, representing the torso and one leg. The B_4C containing synovium phantoms were positioned at the appropriate location in the leg box, as described in section 5.1.5. Graphite blocks were positioned on the top, bottom and back sides of the leg box to reflect escaping neutrons back to the leg box to increase the neutron flux in the synovium phantom. It is anticipated that these reflectors will be used during patient irradiations.

The torso box was always filled with water in experiments. However, it was verified experimentally that boron photon detection was not affected by water in the torso box. No change in the boron photon count or the rest of the photon spectrum was observed, whether or not the box was filled with water, and whether or not the box was shielded with lead sheets and/or Rico-Rad. This finding is consistent with results of simulations. The torso box is out of the viewing region of the photon detector, and hence no neutrons and photons from this box can directly arrive at the detector via the aperture in the detector shield. In addition, since the synovium is relatively far away from the torso box, the increase of neutron flux in the synovium caused by neutrons scattered from the torso box can also be neglected. On the other hand, the water-filling condition in the leg box affects the measured photon spectrum significantly. Water is a good moderator of neutrons, and hence the neutron flux and spectrum in the synovium phantom is related to the water level in the leg box, as is the production of boron photons. Moreover, water can attenuate boron photons. The linear attenuation coefficient of water is about 0.1/cm for 478 keV photons. If the thickness of water is 5 cm between the synovium phantom and the detector, the attenuation of boron photons in water is $(1-e^{-5\times0.1})= 0.4$, or 40%.

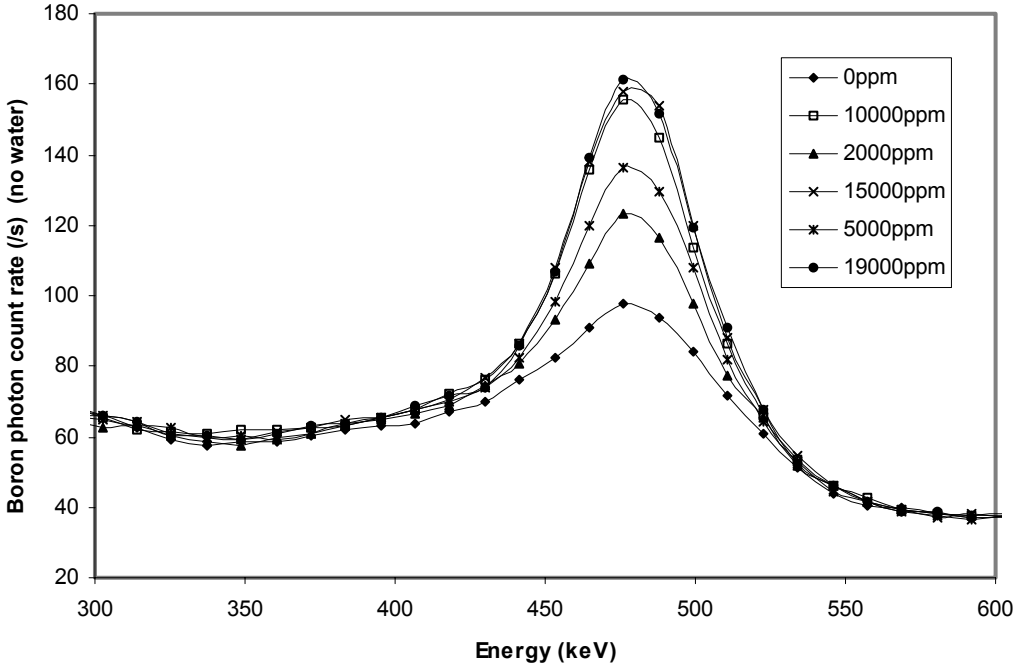

(a)

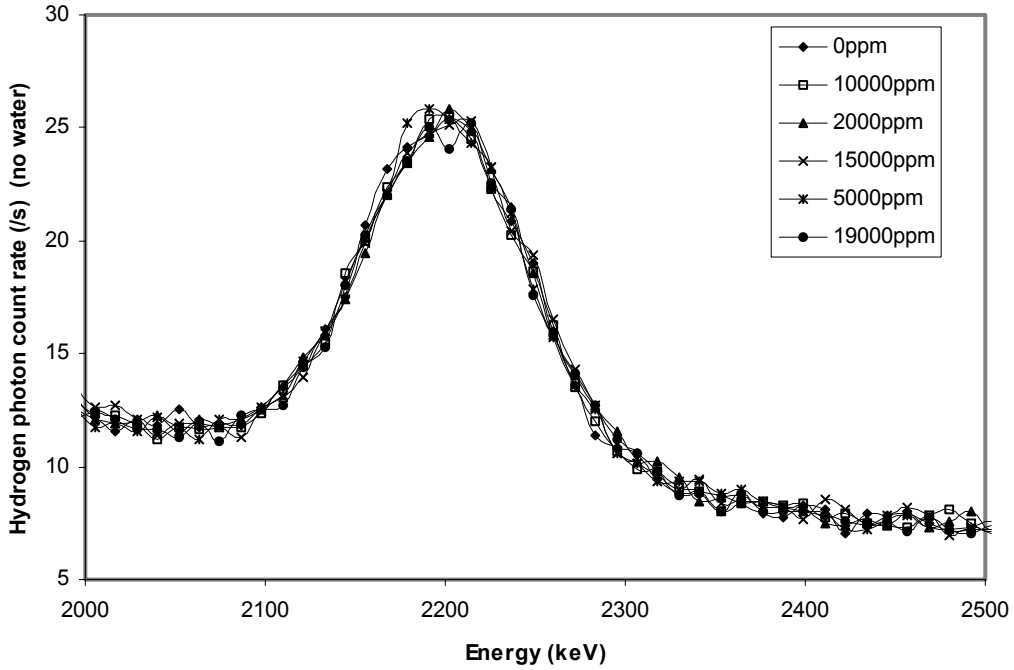

(b)

Figure 7.1 (a) Boron peak and (b) hydrogen peak under various synovial boron concentrations (no water in the leg box).

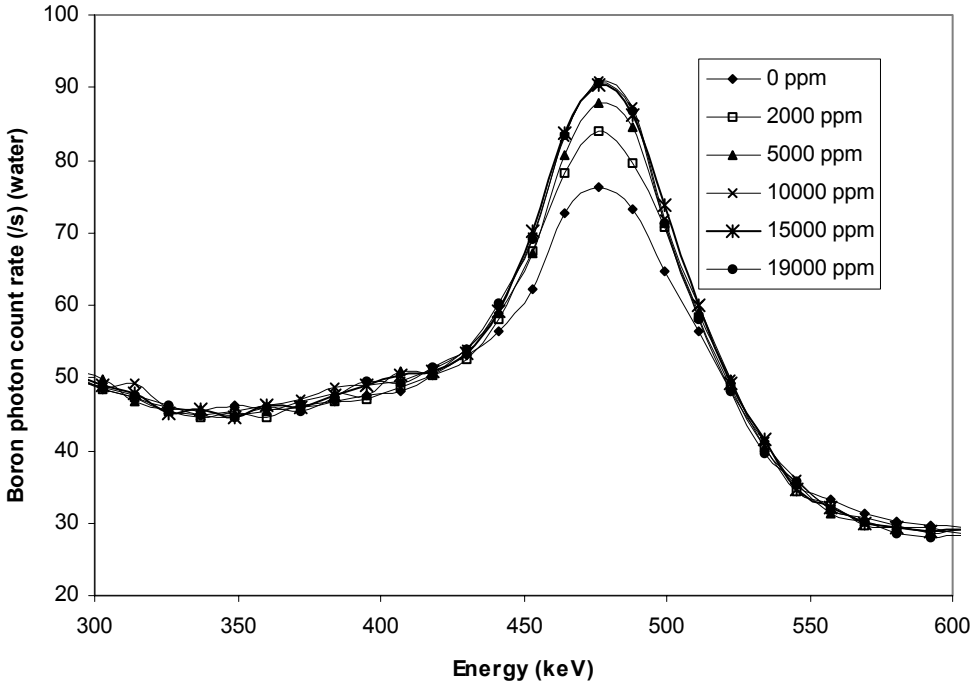

(a)

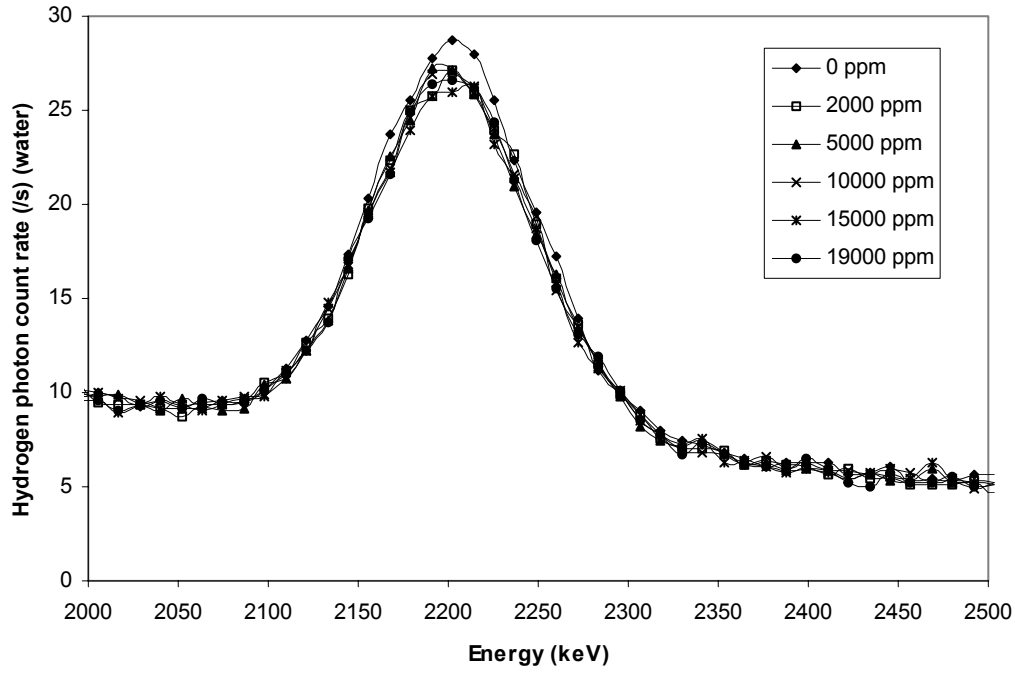

(b)

Figure 7.2 (a) Boron peak and (b) hydrogen peak under various synovial boron concentrations (water in the leg box).

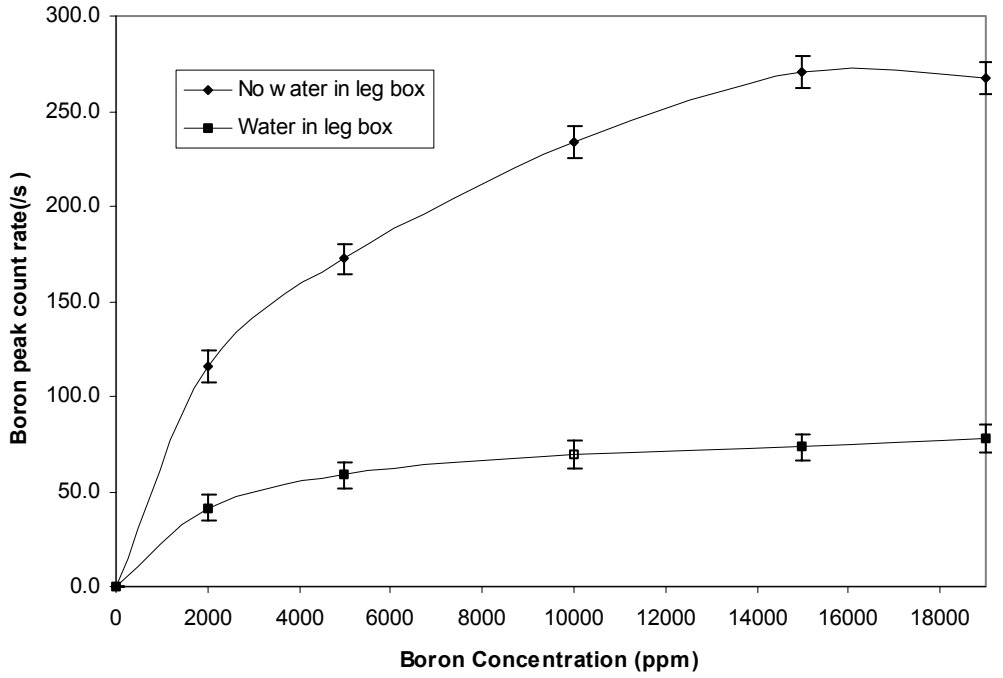

(a)

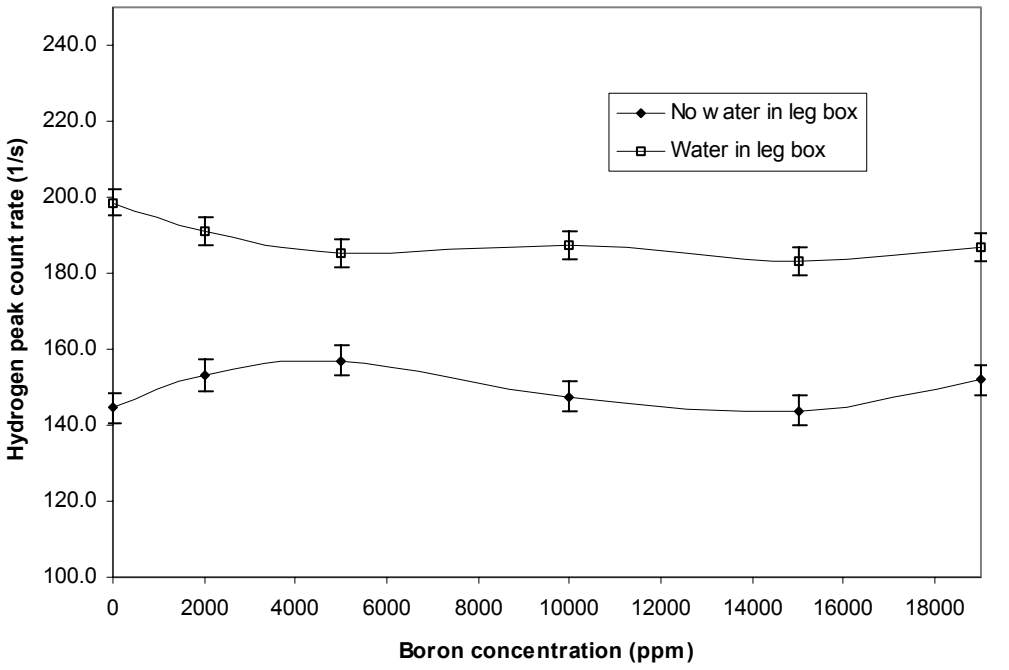

(b)

Figure 7.3 Count rate of (a) boron photons emitted from the synovium and (b) hydrogen counts under various synovial boron concentrations.

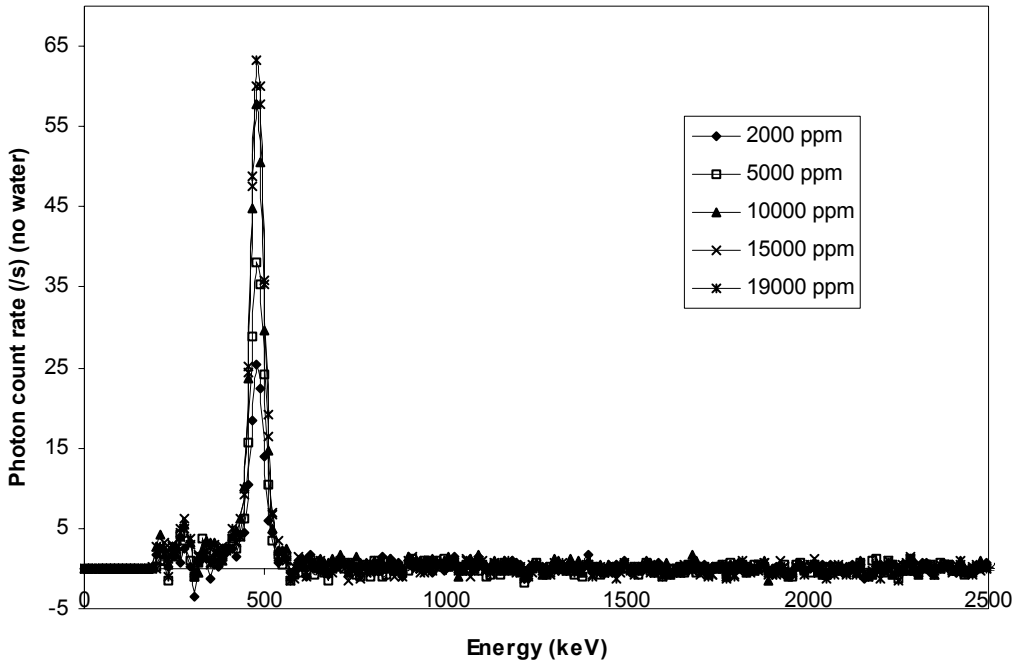

(a)

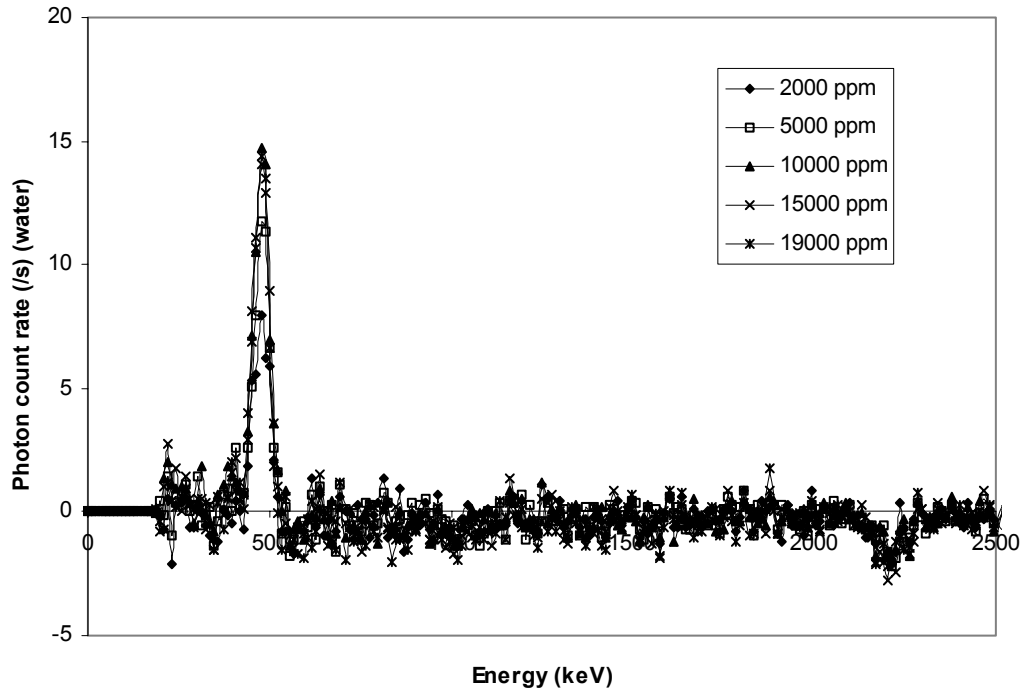

(b)

Figure 7.4 Stripped photon energy spectra for (a) water in the leg box and (b) no-water in the leg box under various boron concentrations in the synovium phantom.

Two cases were experimentally compared: either the leg box is fully filled with water, or it is completely empty. The first case reflects the real situation; the second case is unrealistic, and was investigated for better understanding of the influence of soft tissue on the neutron flux and spectrum in the synovium and attenuation of boron photons from the synovium in the joint. Synovium phantoms containing various boron concentrations were tested for both cases. The radius of the aperture in the collimator, *r*, was 2 cm, corresponding to a *R* of 2.5 cm. This aperture ensured that most of the synovium phantom (4 cm in both width and length) was visible to the NaI(Tl) detector. The experimental results are presented in Figures 7.1 to 7.4. The measured boron peak and hydrogen peak for the two cases appear in Figure 7.1 and Figure 7.2. The increase in boron photon count as the synovial boron concentration goes up is clearly visible for both cases. Since for each case the only parameter varied in the above experiments is the synovial boron concentration, the increased portion of the boron peak count is attributed to the increase of boron photon production in the synovium. No variation in the shape or count of the hydrogen peak under various boron concentrations was observed.

Figure 7.3 plots the detected boron and hydrogen count rates as a function of the synovial boron concentration. The boron photon count rate increases quickly with increasing synovial boron concentration at low boron concentrations, and count saturation is apparent after the boron concentration is over 10,000 ppm. From Figure 7.3 (a), fewer boron photons from the synovium are detected if the leg box is filled with water. For example, at 10,000 ppm, the boron photon count rate for the no-water case is 234±8 counts/s, but is only 69±7 counts/s for the water case. Such a big difference cannot be fully attributed to boron photon attenuation in water between the synovium phantom and the detector. Actually, fewer $^{10}B(n, \alpha)$ reactions occur in the synovium when the leg box is full of water because of neutron flux suppression in water. This finding is very specific for this phantom configuration, and more discussions will be provided in the next section. From Figure 7.3 (b), the hydrogen photon count rate shows no significant dependence on the synovial boron concentration. Within the range of statistical error, the count rate curves are essentially flat. Unlike the situation with boron photons, more hydrogen photons are detected for the water case. The explanation is that there is more hydrogen in the viewing region of the detector when the leg box is filled with water. On the other hand, even when the leg box is empty, the count rate of hydrogen photons is still appreciable. This implies the existence of other hydrogen photon emitters, and the most probable candidate is the boronated polyethylene in the collimator and detector shield surrounding the aperture.

The stripped photon spectra, derived by subtracting the background spectrum at zero ppm from the spectra at 2,000, 5,000, 10,000, 15,000, and 19,000 ppm, are presented in Figure 7.4. Generally, the only apparent feature in the stripped spectra is the boron photon peak. One exception is the hydrogen peak. In Figure 7.4(b), for the case with water in the leg box, a small negative hydrogen peak appears at the right

end of the spectrum. The explanation is as follows: the absorption of thermal neutrons in the boron-containing synovium phantom affects the production of hydrogen photons in water surrounding the phantom. At higher synovial boron concentration, more neutrons are absorbed in the phantom; therefore, the thermal neutron flux in water surrounding the phantom is weaker and fewer $^{1}H(n,\gamma)^{2}H$ reactions occur. This also explains why a negative hydrogen peak does not appear in Figure 7.4(a) for the case with the leg box empty: if there is no water in the leg box, there is no hydrogen photon production there.

The feasibility of detecting the boron photons above the background is revealed in the experimental results. However, compared with the count rate of boron photons expected in simulations presented in Chapter 4, the measured boron photon count rate in experiments is much lower. In section 4.3, a boron photon count rate of over 1,500 counts/s at a beam current of 100 μA and 10,000 ppm synovial boron concentration was predicted. However, the measured count rate is only about 70 counts/s. This difference in count rate is related to several reasons. First, the geometrical configuration of the synovium phantom in experiments (4 cm × 4 cm surface) is very different from that in simulations (a cylindrical shell of 6 cm in length, 6 cm in diameter and 0.15 cm in thickness). It was discovered via Monte Carlo simulations that fewer boron photons are emitted from the synovium phantoms with a 4 cm × 4 cm surface configuration than from the cylindrical shell synovium phantoms. Second, the viewing region of the detector in simulations described in Chapter 4 is different from that in experiments: *R* was 4.3 cm in simulations, but only 2.5 cm in experiments. Third, the position of the photon detector is 260 cm from the synovium phantom in experiments, compared to that of 200 cm in simulations. A more detailed comparison of the simulation and experimental results is presented in the next section. The simulation model was modified to more accurately reflect the experimental configuration, and Monte Carlo simulations were re-run with the goal of predicting new approaches to increasing the count rate of 478 keV photons from the synovium.

7.2 Comparison between simulation and experimental results

Monte Carlo simulations were conducted to compare the boron photon count predicted via simulations to that measured in experiments. The F8 tally (pulse height tally) in MCNP[18] was employed to accumulate the photon count under the 478 keV peak. As pointed out previously, the F8 tally is an analog tally in nature, and except for source biasing, the application of variance reduction methods will cause incorrect results. However, the count efficiency of boron photons is $\sim 10^{-9}$/(source neutron) for the telescope system, which means on average one billion neutrons have to be transported to collect one boron photon. In an analog Monte Carlo simulation, to obtain a statistically reliable result, $\sim 10^{11}$ neutrons or more must be tracked. However, the total computational time required for running 10^{11} neutrons or more is definitely unacceptable (estimated to be over 100,000 hours based on current run time on a PC

with a 800 MHz Pentium III CPU). One way to approach this problem is to sacrifice the accuracy of the results for saving time. Accordingly the neutron/photon coupled transport problem was separated into two independent parts. In the first part, only neutrons were tracked, and the number of $^{10}B(n,\alpha)$ reactions in the synovium (normalized to per source neutron) was tallied. In the second part, boron photons were emitted uniformly and isotropically in the synovium, and the number of boron photons that deposit all the energy in the 10.2 cm × 10.2 cm NaI crystal was obtained with the F8 tally. The count efficiency in the first part was $\sim 10^{-3}$ /(source neutron), and that in the second part was $\sim 10^{-6}$ /photon. The computational time required for each part was only 1 to 2 hours. The overall count probability of 478 keV photons from the synovium is the product of the results in the two parts, in units of per source neutron. The estimated boron photon count rate is the count probability times the neutron yield of the Be(d,n) source. The approximation here is the assumption that boron photons are generated uniformly inside the synovium, which is in general not true.

7.2.1 Number of $^{10}B(n,\alpha)$ reactions in the synovium phantom

The dependence of the number of boron neutron capture reactions on the configuration of the synovium phantom was investigated. It had been verified in simulations and in experiments that the neutron self-shielding effect inside the synovium is significant. A non-linear relationship between the number of $^{10}B(n,\alpha)$ reactions and the synovial boron concentration has been noted, especially at high boron concentrations. It has been shown (Chapter 5) that the number of $^{10}B(n,\alpha)$ reactions depends on the spatial distribution of the boron compound, i.e., the configuration of the synovium phantom. Monte Carlo simulations were performed to compare the following four different configurations of the synovium phantom: a 4 cm × 4 cm surface with a thickness of < 1mm (used in experiments), a cylindrical shell with the dimensions of 6 cm in length, 6 cm in diameter, and 0.15 cm in thickness (used in simulations in Chapters 3 and 4), a solid cylinder 1 cm in diameter, and a solid cylinder 2 cm in diameter. The latter two configurations were tested in experiments at the beginning of the experimental stage; however, no appreciable boron photon count from the synovium could be detected.

Figure 7.5 shows the normalized number of boron neutron capture reactions for the four configurations of the synovium phantom. The water and no-water cases are both calculated for each configuration. Among the four configurations, the cylindrical shell model promises the greatest number of $^{10}B(n,\alpha)$ reactions, i.e., the greatest number of boron photons. The 4 cm × 4 cm surface model takes the second place. The fewest number of reactions occur for the two solid cylinder models. For example, at 10,000 ppm, for the water case, the number of reactions is 2.28×10^{-3} (cylindrical shell), 0.66×10^{-3}(4 cm × 4 cm surface), 0.22×10^{-3}(2 cm diameter cylinder), and 0.12×10^{-3}(1 cm diameter cylinder), respectively.

These numbers show how different the neutron self-shielding effect could be for different boron distributions: for the same amount of boron compound, the number of reactions for a solid cylinder model could be less than one tenth of that for a cylindrical shell model. If we sort the surface area of the four configurations, the same order as that for the reaction number is obtained: 226.2 cm^2 (cylindrical shell), 32 cm^2 (4 cm × 4 cm surface), 7.1 cm^2 (2 cm diameter cylinder), and 3.3 cm^2 (1 cm diameter cylinder).

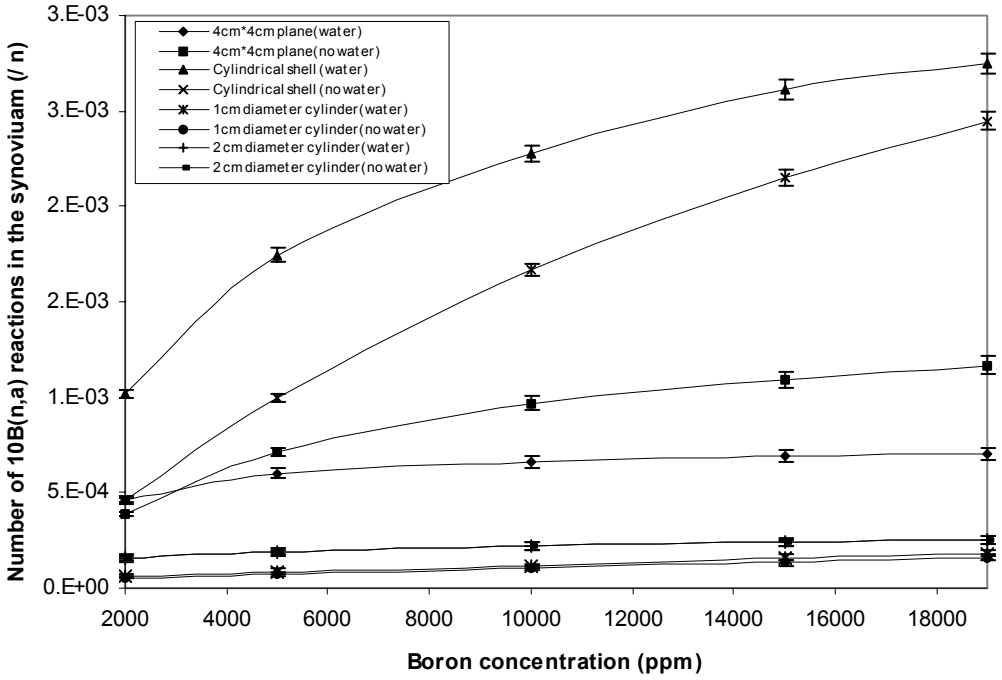

Figure 7.5 Number of $^{10}B(n,\alpha)$ reactions in the synovium for four different configurations of the synovium phantom.

There is an apparent singularity for the 4 cm × 4 cm surface configuration. For all other three configurations, more reactions happen for the water case than for the no-water case. However, for the surface configuration, more capture reactions occur in the no-water case (except at 2,000 ppm). The explanation is as follows. In the surface configuration, compared to the width and length, the thickness of the phantom is very small (0.026 cm). Therefore, whether or not the leg box is filled with water, almost all neutrons enter into the phantom from its front or back surfaces, and the number entering from the narrow side surfaces is negligible. The situation for the other three configurations is different. When the leg box is empty, there is no neutron scattering in the box. The neutrons absorbed in the synovium phantom mainly come from the beam direction. After the box is filled with water, neutrons are moderated and scattered. Neutrons can enter the phantom from other directions in addition to the beam direction

since the surface area in other directions is comparable to that in the beam direction, as illustrated in Figure 7.6. Therefore, the total number of neutron captures inside the phantom is increased.

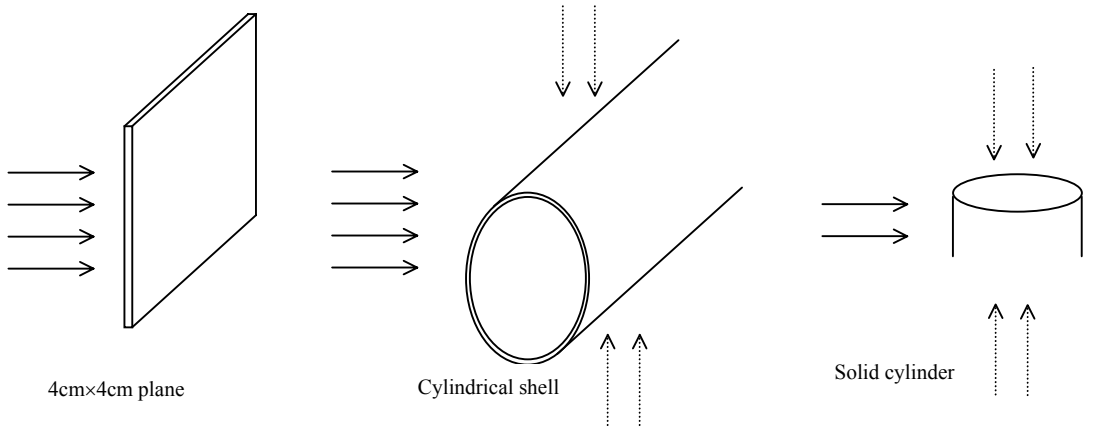

Figure 7.6 Schematic illustration of the peculiarity of the plane configuration.

Compared to the simulation results presented in Chapter 3, the number of $^{10}B(n,\alpha)$ reactions in the synovium is much smaller here, even though the same phantom configuration of cylindrical shell is applied. For example, at 10,000 ppm, the number of $^{10}B(n,\alpha)$ reactions is 6.76×10^{-3} /source neutron, based on the configuration in Figure 3.6; however, for the water case in Figure 7.5, the number is only 2.28×10^{-3} /source neutron, only one third of the number above. This discrepancy may be attributed to the difference of the leg model in the two configurations or the arrangement of reflectors (in the experimental configuration in Chapter 5, the length of the back reflector is cut to be one half of that in Figure 3.4). However, it is demonstrated in simulations that the primary reason is attributed to the change of the size of the D_2O moderator. In Figure 3.6, the length of D_2O is 12 centimeters, and the radius is 10cm; however, in Figure 5.3, the length of D_2O is extended to 16cm and the radius of is shrunk to 4.5 cm. The length increase of D_2O drops the thermal neutron flux in the synovium significantly.

7.2.2 Boron photon contribution probability

The boron photon contribution probability is estimated for two configurations of the synovium phantom: the 4cm×4cm surface model and the cylindrical shell model. Five different sizes of collimator aperture (r =1.75 cm, 2.0 cm, 2.5 cm, 3.0 cm and 3.5 cm) are chosen, and the corresponding radius of the detector viewing region R is 2.2 cm, 2.5 cm, 3.1 cm, 3.8 cm, and 4.4 cm. The water and no-water cases are compared.

The contribution probabilities of the boron photons from the synovium phantom for the two phantom configurations are shown in Figure 7.7. The difference in contribution probability between the water and

no-water cases is obviously because of the photon attenuation in water. For each case (with or without water in the leg box), the contribution probability for the 4 cm × 4 cm surface model is always larger than that for the cylindrical shell model in this range of r (r < 3.5 cm). For the 4 cm × 4 cm surface model, an apparent sign of saturation in probability is observed when r is larger than 2.0 cm (R is larger than 2.5 cm, correspondingly), which is obviously reasonable. When r is greater than 2 cm, the major part of the synovium phantom is already visible to the detector (the detector can see all of the phantom if R >2.8 cm.), and therefore the increase in boron photon count will be slow when r is increased further more. For the cylindrical shell model, the count saturation starts when r is greater than 3 cm. When r = 1.75 cm, the contribution probability for the cylindrical shell model is much smaller than that for the surface model; however, when r = 3.5 cm, the difference in probability is very small.

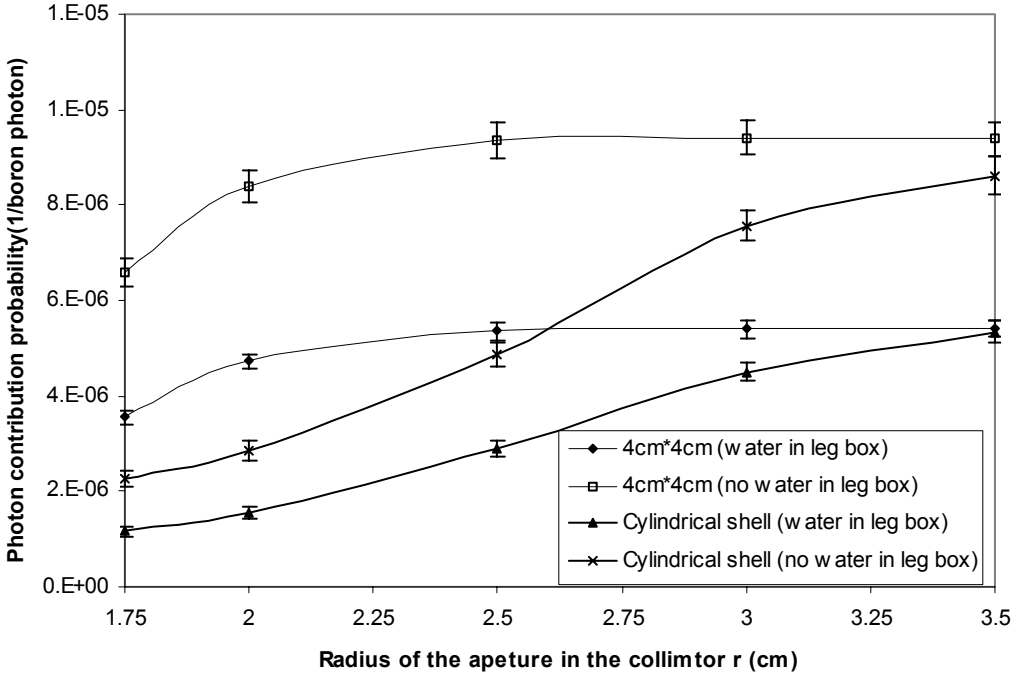

Figure 7.7 Photon contribution probability as a function of the radius of the aperture in the collimator for the plane and cylindrical shell synovium phantom configurations.

For each phantom configuration, the two probability curves for the two water-filling conditions are not parallel, as illustrated in Figure 7.7. The reason is that the average attenuation length in water for boron photons from the synovium is a not constant for different sizes of the aperture in the collimator. Instead, the average attenuation length increases as r increases. Therefore, the attenuation factor exp[−μ·(average attenuation length in water)], which is also the ratio of the probabilities for the two cases (water and no-water), continues to drop as r increases. This analysis is consistent with the appearance of the two

probability curves for the cylindrical shell configuration in Figure 7.7. For the surface configuration, the two probability curves are close to parallel, which is because the average attenuation length is close to a constant after the radius of the aperture is larger than 2 cm.

7.2.3 Estimation of the boron photon rate from the synovium

The normalized boron photon count equals the product of the $^{10}B(n,\alpha)$ reaction number/source neutron in the synovium discussed in 7.2.1, the photon contribution probability from the synovium discussed in section 7.2.2, and the branching ratio of the boron photon emission following the $^{10}B(n,\alpha)$ reaction (0.93).

The count rate of boron photons detected by the NaI detector is the product of the normalized boron photon count/source neutron, the neutron production yield, and the accelerator beam current (mA). The neutron yield for the Be(d,n) reaction at the deuteron energy of 1.5 MeV is 1.67×10^{13}/mA·minute, and the beam current is 100 μA.

Table 7.1 Simulated boron photon counts for the 4cm × 4cm plane synovium configuration (/s)

ppm	Water					No-water				
	r (cm)					r (cm)				
	1.75	2.0	2.5	3.0	3.5	1.75	2.0	2.5	3.0	3.5
2000	43±3	57±3	64±4	65±4	65±4	66±4	84±5	94±5	95±5	94±5
5000	55±3	73±4	83±5	84±5	84±5	121±7	154±8	172±8	173±8	173±8
10000	61±4	81±5	92±5	92±5	92±5	165±10	210±12	234±13	236±13	235±13
15000	64±4	85±5	96±6	97±6	97±6	186±11	238±13	265±15	267±15	266±15
19000	64±4	86±5	97±6	98±6	98±6	199±12	254±14	283±16	285±16	284±16

Table 7.2 Simulated boron photon counts for the cylindrical shell synovium configuration (/s)

ppm	Water					No-water				
	r (cm)					r (cm)				
	1.75	2.0	2.5	3.0	3.5	1.75	2.0	2.5	3.0	3.5
2000	31±3	41±3	77±4	119±6	142±6	27±2	34±2	59±3	91±4	103±5
5000	53±5	70±5	131±8	204±10	242±11	59±5	74±5	126±7	196±9	223±11
10000	69±6	92±7	171±10	265±13	315±14	98±8	123±9	211±12	327±16	373±19
15000	79±7	105±8	196±11	305±14	361±16	126±10	159±11	271±16	420±20	479±24
19000	83±7	111±8	207±12	321±15	380±17	143±11	181±13	309±18	479±23	546±27

The estimated boron photon count rate for the two phantom configurations (surface and cylindrical shell) is provided in Table 7.1 and Table 7.2, respectively. For each phantom configuration, the water and no-water cases are compared for five sizes of the aperture in the collimator. Very instructive information on understanding the performance of the telescope system is supplied in Table 7.1 and Table 7.2. For r = 2 cm, the boron photon count rate for a cylindrical shell synovium phantom is only a little higher than that for a surface synovium phantom at a synovial boron concentration of above 5,000 ppm. However, the

absolute count rate is still low (92±7 counts/s at 10,000 ppm). For r = 3.5cm (R= 4.4 cm), when the entire cylindrical shell phantom is visible to the NaI(Tl) detector, the situation is different for the two phantom configurations. The boron photon count rates for the surface phantoms are only very slightly increased compared to those for r = 2 cm, and this increase comes from the increase of the boron photon contribution probability at the edges and corners of the phantoms. On the other hand, the boron photon count rates for the cylindrical shell phantoms are more than tripled under all boron concentrations. The boron count rate reaches 3150 counts/mA·s, which is expected to be enough for rapid dose determination during joint irradiation.

The measured boron photon count rate in experiments is compared to that predicted in simulations (r = 2 cm) in Figure 7.8. In spite of the approximation made when pursuing the photon contribution probability (a uniform boron photon production in the synovium, section 7.2.2), the simulation results match the experimental data very well. Monte Carlo simulations accurately predicted the tendency of the boron photon count as the boron concentration increases. Moreover, the absolute discrepancy between experimental and simulation results is very small (only 10% to 20% for most data points), which confirms the reliability of the Monte Carlo method in developing the telescope system.

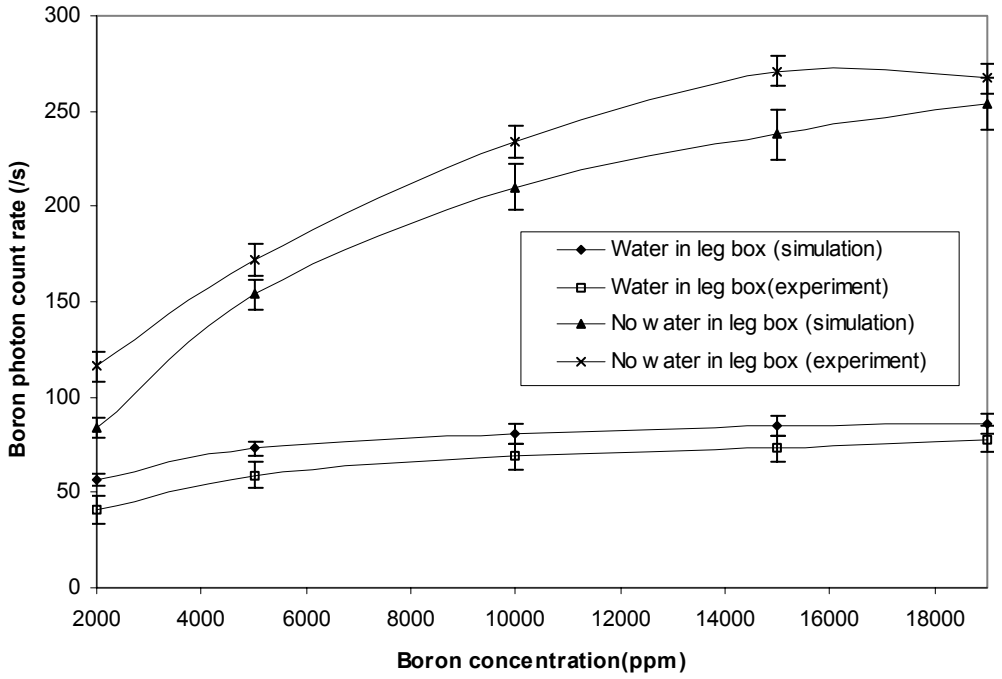

Figure 7.8 Comparison of experimental results with simulation results for the synovium phantom with a configuration of 4 cm × 4 cm surface.

7.3 Further improvement by rearranging the back and side reflectors

The effectiveness of the side and back reflectors surrounding the knee joint in increasing the number of $^{10}B(n,\alpha)$ reactions in the synovium was demonstrated in simulations (Figure 4.13). The arrangement of the reflectors in experiments is a little different from that in simulations. As illustrated in Figure 5.3, in the experimental setup, the length of the back reflector is only one-half of that in simulations because there was not sufficient space between the leg phantom and the collimator to position the left half of the back reflector.

Investigations were conducted to examine the potential improvement in boron photon detection by rearranging the reflectors. In experiments, the lengths of the reflectors were increased, and the positions of the reflectors were slightly moved in various directions. However, no increase or decrease in the boron photon count rate could be recognized. This indicates that it is likely not possible to further increase the thermal neutron flux in the synovium by rearrangement of the reflectors.

7.4 Dead time issue

In the previous experiments, the beam current was set to 0.1 mA. The dead time of the MCA system was less than 10%. In future BNCS clinical trials, the beam current is expected to be at the level of 1 mA. Therefore, the total count rate of boron photons plus background will be one order of magnitude higher. The present MCA system will not work properly at such a count rate. However, the count rate at one mA beam current is expected to be around 30 k/s, and a faster ADC (analog to digital converter) will be able to easily handle this rate. Since only one feature (the boron peak) in the spectrum is needed, an 8-bit ADC (total 256 channels) is sufficient. Moreover, the MCA can be replaced with a SCA (Single Channel Analyzer)[14] if the dead time is still too high.

7.5 Development of a general telescope system for BNCS

This ultimate goal of this thesis work is to design a telescope system for BNCS based on an accelerator neutron beam. The investigation is conducted under a particular neutron production reaction ($^{9}Be(d,n)$ at a deuteron energy of 1.5 MeV) and a particular therapy room (the radiation vault at LABA). However, the work has been toward developing a general telescope for BNCS, i.e., a telescope system that is also applicable to other candidate neutron production reactions and other configurations of the therapy room. This idea has been supported by the following discoveries.

The influence of the concrete ceiling, floor, and walls of the radiation vault at LABA on neutron and photon background distribution in the radiation vault has been investigated via Monte Carlo simulations (Chapter 3). The simulation results with and without the presence of the concrete surroundings are

compared. The comparison indicates that these concrete surroundings do pose important effects on background distribution in the radiation room: the magnitudes of particle fluxes are different (one order of magnitude for neutron flux at locations far from the neutron target); however, the most important conclusion regarding the regions where the photon detector should be located is consistent since the locations where the largest and lowest neutron and photon fluxes occur are not changed. In particular, after collimation and detector shielding, the influence from the infrastructure of the therapy room on the neutron and photon fluxes at the detector location will be significantly reduced. Therefore, it is expected that the important conclusions drawn for the LABA radiation vault will be valid for a variety of configurations of the therapy room.

As for the nuclear reaction for neutron production, in fact, another reaction ^{9}Be(p,n) at a proton energy of 4 MeV was initially used as the neutron production reaction in Monte Carlo simulations. The results and conclusions for ^{9}Be(d,n) and ^{9}Be(p,n) reactions are very similar: similar boron neutron capture rate in the synovium, same conclusion about the optimum detector position, same magnitude of background neutron and photon fluxes at the location of the photon detector before and after collimation and shielding. Thus, the telescope developed for the ^{9}Be(d,n) reaction is also useful for other nuclear reactions.

Based on the above discussion, although the development of a telescope system was conducted under a particular neutron production reaction and a particular radiation room, the conclusions are expected to be valuable for a wide range of nuclear reactions and therapy rooms.

7.6 Conclusions

In spite of the appearance of a background peak at the location of the boron peak, boron photons from the synovium can be easily detected above background. The boron photon production in the synovium and the number of boron photons detected are strongly dependent on the configuration of the synovium phantom.

There are two ways to increase the signal to noise ratio: increase the boron photon count rate or reduce the background count rate. It was mentioned in Chapter 5 that further background reduction is very difficult since the remaining background counts mainly originate from neutrons and photons entering the detector via the aperture in the collimator and detector shield. In this chapter, the significant influence of the spatial distribution of boron compound in boron photon production was investigated: for the same amount of compound, the larger the area over which the compound is distributed, the larger the number of boron neutron captures.

MCNP simulation is very useful and reliable. The prediction of a non-linear relationship between the synovial boron concentration and the count rate of detected 478 keV boron photons was verified in

experiments. Even the absolute boron photon count rate obtained in simulations is very close to that measured directly in experiments. Consequently, the Monte Carlo method can be used as a predicting tool in developing the telescope system.

Chapter 8 Reconstruction of synovial boron dose

In Chapters 5 and 7, the feasibility of the detection of the boron photons from the synovium was experimentally confirmed. Although the background boron peak still exists in the measured photon spectrum, the contribution from the boron photons originating from the synovium is easily extractable and quantifiable.

In this chapter, the investigation is directed to the next step of the project: finding an online approach for synovial boron dose determination.

8.1 Basic problem

The goal of the telescope system is to determine the boron dose in the synovium. However, the information directly obtainable from the telescope system is the detected boron photon count from the synovium. Therefore, the relationship between the synovial boron dose and the number of synovial boron photons detected by the NaI detector must be determined. If the synovial boron dose and the number of detected boron photons are denoted as D and B, respectively, the above statement is equal to pursuing a mathematic function between D and B, i.e., $D = g(B)$. The ideal case is that for a given B, D will be directly calculated from function g.

In most practical cases, B itself is not enough to determine the boron dose D. There are other factors affecting the detection of the boron photons from the synovium in addition to the boron photon emission rate from the synovium. Additional information may have to be supplied to account for the influence of these associated factors. The possible boron dose reconstruction approaches will be proposed in this chapter, and the additional information that has to be supplied will also be analyzed.

The averaged absorbed boron dose D in the synovium can be estimated as

$$\frac{\text{Energy deposited in the synovium by heavy charged particles}(^7\text{Li and } \alpha)}{\text{Mass of the synovium}}$$

$$= \frac{(\text{Total number of boron neutron captures in the synovium N}) \cdot (\text{Average energy released in each capture})}{\text{Mass of the synovium}}.$$

The average kinetic energy deposited in each capture is known as 94%×2.310 MeV+6%×2.792 MeV = 2.339 MeV, and the mass of the synovium is also a constant during neutron irradiation. Therefore, the boron dose D is proportional to the total number of 478 keV photons emitted from the synovium N. Since D will be known if N is determined, the reconstruction problem is the same as a search for a function between B and N, i.e. $B = f(N)$ or $N = f^{-1}(B)$. Actually, it is more convenient to explore the mathematical expression of f instead of g because B and N are more closely correlated. The function f is dependent on

the total amount of ^{10}B in the synovium and its spatial distribution within the synovium; however, it is also related to the anatomical structure of the joint, the neutron spatial distribution, and other factors.

At Petten, the Netherlands, a telescope system was built for online determination of *boron concentration* in brain tumors[13]. However, at MIT LABA, knowledge of *accumulated synovial boron dose* is the goal. Although, *B*, the boron peak count, is required in the reconstruction process for both cases, differences in the reconstruction approaches arise from the different ultimate goals. In reconstruction of the synovial boron concentration at Petten, B/H (the ratio of the boron peak count to the hydrogen peak count) was used. The boron concentration in the synovium is a physical quantity determined by the amount and properties of the boron compound, and also by the biological and physiological mechanisms of the human body. Since *B* and *H* are both proportional to the neutron flux, their ratio B/H is neutron flux independent. On the other hand, if the synovial boron dose is required (as for BNCS), *B* is a better choice than B/H since the synovial boron dose is also related to the neutron flux as *B* is.

8.2 Non-uniformity of [B] and Φ in the synovium

The spatial extension of the synovium causes non-uniformity in boron photon production as well as photon contribution probability to the photon detector among the various parts of the synovium. The non-uniformity existent in the synovium and its potential influence on the dose reconstruction will be analyzed, before the analytical expression of the function *f* is deduced.

First, the boron concentration, [B], may not be uniform in the synovium. Although the appropriate boron compound for BNCS is still under investigation, preliminary results from in-vitro animal experiments did not support a uniform boron distribution throughout the entire synovium.

Second, as illustrated with a two dimensional illustration of a knee joint in Figure 8.1, thermal neutron flux, Φ, may vary significantly at different locations in the synovium. In this figure, the dark regions represent the inflamed synovium. Suppose a thermal neutron beam bombards the knee joint on its left side. Then the neutron flux decreases continuously from the left side of the joint (beam inlet) to the right side of the joint because of the neutron attenuation in the synovium. Since the synovial boron concentration is fairly high (several thousands of ppm), the thermal neutron flux suppression in the synovium is severe. Thus the average thermal neutron flux at the left side of the synovium is much higher than that at the right side. In actual BNCS clinical treatments, bilateral irradiation would be performed. Therefore, there would not be significant differences in neutron flux between left and right sides of the joint. However, the difference in flux between the center and the edges of the joint will still be significant.

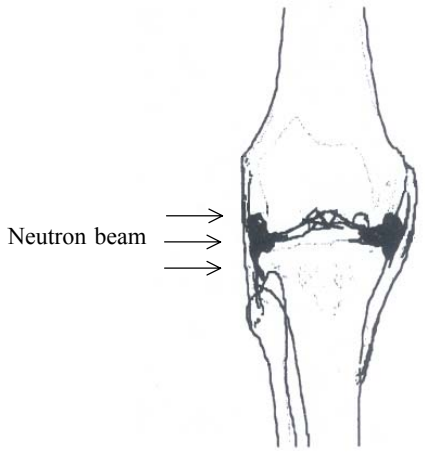

Figure 8.1 Illustration of the non-uniformity of thermal neutron flux in the joint.

Boron photon production in the synovium is proportional to $[B]\cdot\Phi$, the product of the boron concentration and the neutron flux. Since the thermal neutron flux Φ varies considerably, the photon production will be quite different at the various positions in the synovium, no matter whether the boron compound is distributed uniformly or not.

In addition to photon production, non-uniformity also occurs in photon detection. The detection probability for a photon emitted from somewhere in the synovium is related to three aspects. The first one is the initial position and direction of this photon. Only the boron photons generated somewhere within the viewing region of the detector have the chance of being detected by the NaI detector. As explained previously, the photon arrival probability is not the same throughout the viewing region of the detector: photons produced at the center of the viewing region have higher probability of reaching the detector; however, for those emitted at the edge of the viewing region, the probability of arriving at the detector is almost zero. Since the mean free path of 478 keV photons is comparable to the size of the knee joint, boron photon detection is also affected by the photon attenuation in the knee joint. If the photon detector is located on the right hand of the knee joint in Figure 8.1, boron photons released at the leftmost end of the synovium have to pass through the whole joint before reaching the detector. In contrast, boron photons generated at the rightmost end of the synovium basically experience no attenuation on their way to the detector. The location dependency of the photon attenuation has to be taken into account. The third aspect is the intrinsic detection probability of the photon detector, which is purely a property of the photon detector.

In a brief summary, the number of detected boron photons B is not only determined by the total number of the boron photons emitted from the synovium, N, it is also dependent on where these photons are generated. The boron photon production in the synovium is determined by the spatial distributions of the thermal neutron flux and the boron compound. For the purpose of boron dose determination, what is required is the product of [B] and Φ, not the separate values of [B] and Φ. To determine N and [B]·Φ, the anatomic structure of the joint is necessary for considering the photon attenuation in the joint.

8.3 Boron dose determination

Because of the non-uniformity of [B]·Φ in the synovium, the boron dose could vary significantly in different parts of the synovium. Therefore, it is not practical to treat the whole synovium as a single entity when reconstructing the boron dose. The way to solve the problem is to divide the synovium into a certain number of small volumes called voxels. The criterion of the synovium division is that [B]·Φ should be uniform throughout the voxel. If the span of a voxel is much smaller than the mean free path of 478 keV photons in soft tissue, the gravity center of this voxel can represent the whole voxel in calculating the photon contribution probability to the detector.

8.3.1 One measurement approach

Suppose the synovium is divided into M voxels, as illustrated in Figure 8.2.

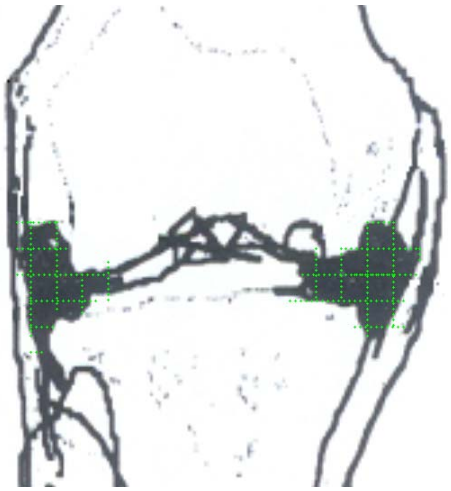

Figure 8.2 Illustration of the division of the synovium into small voxels.

The total boron photon count, B, equals the sum of the individual counts from all M voxels:

$$B = \sum_{i=1}^{M} N_i \cdot P_i = \sum_{i=1}^{M} \left(\frac{N_i}{\sum_{i=1}^{M} N_i} \cdot P_i \cdot \sum_{i=1}^{M} N_i\right) = \left(\sum_{i=1}^{M} N_i\right) \cdot \sum_{i=1}^{M} \left(\frac{N_i}{\sum_{i=1}^{M} N_i} \cdot P_i\right) = N \cdot \sum_{i=1}^{M} \left(\frac{N_i}{N} \cdot P_i\right),$$

where N_i is the number of 478 keV photons emitted in voxel i, and P_i is the detection probability of boron photons in voxel i, which is defined as the probability for a 478 keV photon generated in voxel i being collected under the boron peak in the photon spectrum measured by the NaI detector. Obviously, the product of N_i and P_i is the number of detected boron photons from voxel i.

Since N_i is proportional to $[B]\cdot\Phi$, then

$$B = N \cdot \sum_{i=1}^{M} \left(\frac{[B]_i \Phi_i}{\sum_{i=1}^{M} [B]_i \Phi_i} \cdot P_i\right) \quad \text{or} \quad N = B / \left[\sum_{i=1}^{M} \left(\frac{[B]_i \Phi_i}{\sum_{i=1}^{M} [B]_i \Phi_i} \cdot P_i\right)\right],$$

where $N = \sum_{i=1}^{M} N_i$, is the total number of boron photons emitted in the synovium. Now, we have already found the expression of the function *f* between *B* and *N*, which is simply a coefficient $\sum_{i=1}^{M} \left(\frac{[B]_i \Phi_i}{\sum_{i=1}^{M} [B]_i \Phi_i} \cdot P_i\right)$

Now the problem becomes finding the two factors $\frac{[B]_i \Phi_i}{\sum_{i=1}^{M} [B]_i \Phi_i}$ and P_i for each voxel, and altogether there are 2*M* factors. Since the first factor is associated with photon production, it is called *photon production factor* here; correspondingly, the detection probability P_i is also called *photon detection factor*. After the 2*M* factors are obtained, the total number of boron photons *N* could be estimated as

$$N = B / \left[\sum_{i=1}^{M} \left(\frac{[B]_i \Phi_i}{\sum_{i=1}^{M} [B]_i \Phi_i} \cdot P_i\right)\right].$$

Since $\frac{N_i}{N} = \frac{[B]_i \Phi_i}{\sum_{i=1}^{M} [B]_i \Phi_i}$, the number of boron photons emitted in each voxel N_i equals

$$N_i = \frac{[B]_i \Phi_i}{\sum_{i=1}^{M} [B]_i \Phi_i} \cdot N = \frac{[B]_i \Phi_i}{\sum_{i=1}^{M} ([B]_i \Phi_i P_i)} \cdot B \ .$$

Therefore, in theory, not only is the overall average boron dose in the whole synovium available, the boron dose in each voxel is also obtainable.

8.3.2 Estimation of dose reconstruction factors

8.3.2.1 Photon detection factor P_i

Estimation of the P_i factor for a voxel is very straightforward. As pointed out previously, P_i depends on the solid angle toward the detector, photon attenuation in the joint, and the intrinsic detection efficiency of the specific detector. More explicitly, P_i can be described in a relation

$$P_i = \Omega_{Gi} \cdot T_i \cdot \varepsilon_{Di} \ .$$

In this equation,

Ω_{Gi} is the fraction of the 478 keV photons emitted in voxel i in the direction of the detector, which equals the ratio of the projection area of voxel i on the detector surface to $4\pi L_i^2$, with L_i being the distance between the centers of the voxel and the front surface of the detector;

T_i is the photon transmission factor in the joint, which is expressed as $\exp[-\int \mu(x) \cdot dx]$, where $\mu(x)$ is the linear attenuation coefficient of 478 keV photons in the joint;

$\Omega_{Gi} T_i$ defines the faction of the 478 keV photons emitted in voxel i that will arrive at the front surface of the detector;

ε_{Di} is the intrinsic detection efficiency of the NaI detector for 478 keV photons.

If the anatomical structure of the joint is available, Ω_{Gi} and T_i can be easily calculated. ε_{Di} is a known property of the detector. Then, P_i can be calculated without difficulty. More conveniently, Monte Carlo simulations can also be conducted to estimate P_i for each voxel. 478 keV photons can be started either uniformly in a voxel or only at the center of it if the size of the voxel is small enough, with an isotropic angular distribution. The F8 tally in MCNP can be applied to count the number of photons under the boron peak, and finally P_i is calculated as the ratio of the number of photons counted from voxel i to the total number of source photons emitted from voxel i.

8.3.2.2 Photon production factor $\frac{[B]_i \Phi_i}{\sum_{i=1}^{M} [B]_i \Phi_i}$

Compared to the simplicity of the P_i factor, it is much more difficult to estimate the factor $\frac{[B]_i \Phi_i}{\sum_{i=1}^{M} [B]_i \Phi_i}$.

The problem arises from the requirement of knowing $[B]_i \cdot \Phi_i$ in each voxel. If not enough information about $[B]_i$ is available, generally we have no way of knowing this photon production factor.

It has been pointed out previously that there is not enough evidence to guarantee a uniform boron distribution in the synovium. On the other hand, even if the assumption of a uniform boron distribution is valid, this problem is still complicated. If $[B]$ could be assumed to be roughly the same in all voxels, the expression of the photon production factor is simplified to $\Phi_i / \sum_{i=1}^{M} \Phi_i$. At first glance, since [B] does not appear any more, it could be easier to get the solution of the photon production factor. However, this is not necessarily true because the thermal neutron flux is boron concentration dependent.

At Petten, a uniform boron concentration in the brain tissue was assumed, and then Monte Carlo simulations were conducted to estimate the thermal neutron flux distribution in the head (brain, skull, and skin). In BNCT, the boron concentration in the target tissue is at the level of tens of ppm, and the thermal neutron flux suppression inside the target tissue is not significant. Thus, the distribution of thermal neutron flux in the target tissue is not expected to vary substantially with regional variations in boron concentration within the tissue. In contrast, in BNCS, the boron concentration is much higher (several thousands of ppm), and thus regional variations in boron concentration will lead to substantial spatial heterogeneity in neutron flux. Therefore, to determine the photon production factor, it is necessary to know the actual boron concentration in all regions in the synovium to determine the neutron flux distribution. In the above expression of the photon production factor, thermal neutron flux Φ_i emerges in a ratio. Therefore, the *relative* neutron flux is sufficient to calculate the production factor, and the absolute neutron flux is not required. As a result, the Monte Carlo method can be a very helpful tool.

The situation becomes more complicated if the assumption of an approximately uniform boron concentration is no longer valid. A rough boron distribution in the synovium has to be supplied before the relative thermal neutron flux in each voxel can be estimated. In fact, this could be the most difficult and uncertain part of the dose reconstruction process. For BNCS, information about the distribution of the boron compound will be obtained first via in-vivo animals studies. Compounds chosen for therapeutic use with humans would be then tested in rheumatoid arthritis patients undergoing total knee replacement

surgery. The compound would be injected intra-articularly prior to surgery. Samples of synovium would be obtained at the time of surgery and the boron concentration in each sample would be measured. Correlating measured boron concentration with location of the original synovial samples will generate a crude estimate of boron concentration throughout the synovium.

It is not surprising that additional information is needed in determining the boron dose using the one measurement approach. Only one quantity (the boron peak count *B*) is obtained from the telescope; however, there are many unknowns associated with the photon production and detection in the expression of the function *f*. Since only one unknown can be solved with one equation, additional information has to be supplied to make the other unknowns in this equation knowable or estimable. To determine the function *f*, only the relative photon production in each voxel ($[B]_i \Phi_i / \sum_{i=1}^{M} [B]_i \Phi_i$) is necessary. This implies the only unknown left is the intensity of the neutron beam. Therefore, we can interpret that the function of the telescope in the one measurement approach is to monitor the neutron beam intensity or the beam current. The additional information such as the anatomical structure of the joint and the boron compound distribution enable us to decide how many boron photons are emitted in each voxel per unit accelerator beam current and how many of these photons are finally detected. After the beam current/intensity is determined with the telescope, the number of the boron photons emitted in each voxel is known.

An example showing the procedure for synovial boron dose determination using the one measurement approach was performed with Monte Carlo simulations, which was based on the 4 cm × 4 cm surface phantoms utilized in previous simulations and experiments. The surface phantom was equally divided into 16 1 cm × 1 cm voxels, as shown in Figure 8.3. The boron concentration in the synovium phantom is 10,000 ppm, and is uniform everywhere inside the phantom. However, since the thermal neutron flux is not uniform, the boron photon production is different in these voxels. MCNP was used to estimate the number of boron photons produced in each voxel and the photon detection factor P_i for each voxel. The results are listed in Table 8.1. In this example, the radius *R* of the detector viewing region is 2.5 cm. Consequently, the four corners of the synovium phantom are out of the viewing region (*R* has to be over 2.8 cm in order to cover the entire phantom in the viewing field of the detector). This explains why in Table 8.1 the P_i values for the four corner voxels (5, 8, 11, and 14) are much smaller than those for other voxels. On the other hand, more $^{10}B(n,\alpha)$ reactions occur in the corner voxels than in their neighbors and in the inner voxels (voxels 1, 2, 3, and 4). This can be understood by examining the neutron flux suppression in the phantom: the neutron flux at the center of the phantom is the lowest and that at the four

corners is the highest. In Table 8.1, the number of boron capture reactions is the fewest in the four central voxels, as expected. Using the data in Table 8.1, the simulated total count rate of boron photons by the 4 inch × 4 inch NaI crystal is $(\sum N_i' P_i)$ = 89/s, where N_i' is the simulated number of boron photons emitted from voxel i at 100 μA of accelerator beam current. The measured count rate in experiments is *B* = 69/s. Then the actual number of boron capture reactions in voxel i is estimated as $N_i = N_i' \times B/(\sum N_i' P_i)$, which is available in Table 8.2.

5	16	15	14
6	1	4	13
7	2	3	12
8	9	10	11

Figure 8.3 Division of the 4 cm × 4 cm synovium plane phantom into 16 1cm × 1 cm voxels.

Table 8.1 Simulated number of boron photons emitted from the voxels and the photon detection factors

Voxel No.	Number of photons N_i' (1/neutron)	P_i	Voxel No.	Number of photons N_i' (1/neutron)	P_i	Voxel No.	Number of Photons N_i' (1/neutron)	P_i	Voxel No.	Number of Photons N_i' (1/neutron)	P_i
1	3.15×10^{-5}	6.35×10^{-6}	5	4.91×10^{-5}	3.46×10^{-6}	9	3.84×10^{-5}	5.55×10^{-6}	13	4.54×10^{-5}	6.20×10^{-6}
2	3.31×10^{-5}	5.94×10^{-6}	6	3.86×10^{-5}	5.79×10^{-6}	10	4.23×10^{-5}	5.82×10^{-6}	14	4.81×10^{-5}	3.54×10^{-6}
3	3.63×10^{-5}	6.22×10^{-6}	7	4.06×10^{-5}	5.78×10^{-6}	11	5.09×10^{-5}	3.34×10^{-6}	15	3.74×10^{-5}	5.89×10^{-6}
4	3.38×10^{-5}	6.29×10^{-6}	8	4.55×10^{-5}	3.16×10^{-6}	12	4.18×10^{-5}	6.21×10^{-6}	16	4.72×10^{-5}	5.88×10^{-6}

Table 8.2 Reconstructed number of boron photons emitted from the voxels at a 100 μA beam current

Voxel No.	N_i(/s)	Voxel No.	N_i(/s)	Voxel No.	N_i(/s)	Voxel No.	N_i(/s)
1	6.79×10^5	5	10.6×10^5	9	8.27×10^5	13	9.79×10^5
2	7.14×10^5	6	8.32×10^5	10	9.10×10^5	14	10.36×10^5
3	7.82×10^5	7	8.75×10^5	11	10.97×10^5	15	8.04×10^5
4	7.27×10^5	8	9.81×10^5	12	9.00×10^5	16	10.17×10^5

8.3.3 Multiple measurement approach

The advantage of the above approach is that only one measurement (one *B*) is needed to perform the reconstruction, and the disadvantage is that additional information has to be supplied to determine the coefficients in the reconstruction function *f*. In particular, it could be very difficult or impossible to obtain the reliable spatial distribution of the boron compound in the synovium. It is imaginable that if multiple detections can be achievable either through simultaneous measurements with multiple detectors at various

locations or through consecutive measurements with one detector rotating and/or translating to various locations, the requirement for knowing [B]·Φ prior to boron dose reconstruction could be eliminated.

In studying the boron compound accumulation in rabbit knees, synovial samples from four regions (anterior, posterior, lateral, and medial) in the knee joint are collected and analyzed. If it is feasible to divide the synovium into four segments (or more) as in rabbit knee studies, and if four (or more) detections can be made at appropriate locations, the following equations hold:

$$B_1 = N_1 \cdot P_{11} + N_2 \cdot P_{12} + N_3 \cdot P_{13} + N_4 \cdot P_{14}$$

$$B_2 = N_1 \cdot P_{21} + N_2 \cdot P_{22} + N_3 \cdot P_{23} + N_4 \cdot P_{24}$$

$$B_3 = N_1 \cdot P_{31} + N_2 \cdot P_{32} + N_3 \cdot P_{33} + N_4 \cdot P_{34}$$

$$B_4 = N_1 \cdot P_{41} + N_2 \cdot P_{42} + N_3 \cdot P_{43} + N_4 \cdot P_{44}$$

with B_i symbolizing the number of detected boron photons at the *i-th* detector location, N_j the number of boron photons emitted from segment *j*, and P_{ij} the detection probability for a boron photon in segment *j* when the detector is positioned at location *i*. For convenience, the above equations are rearranged into the format of matrix and vectors:

$$\begin{bmatrix} P_{11} & P_{12} & P_{13} & P_{14} \\ P_{21} & P_{22} & P_{23} & P_{24} \\ P_{31} & P_{32} & P_{33} & P_{34} \\ P_{41} & P_{42} & P_{43} & P_{44} \end{bmatrix} \begin{bmatrix} N_1 \\ N_2 \\ N_3 \\ N_4 \end{bmatrix} = \begin{bmatrix} B_1 \\ B_2 \\ B_3 \\ B_4 \end{bmatrix}.$$

The reconstruction process then becomes a problem of figuring out a way to solve the $[N_1 \ N_2 \ N_3 \ N_4]^T$ vector. Each element P_{ij} in the coefficient matrix is independent of the thermal neutron flux and the boron distribution in the synovium. The shape and size of the synovium segments can be arbitrary and irregular (no longer rectangular as that in the one measurement approach), and thus estimation of P_{ij} with the Monte Carlo method is more convenient. If the number of measurements is sufficient (larger than or equal to the number of segments), the *N* vector can be obtained with various methods for solving linear equations.

This approach shows the possibility of determining the synovial boron dose without the need for any information about the boron compound distribution. If multiple detectors are available, the B_i s are collected simultaneously under the same beam conditions. The disadvantage is that multiple detector shields have to be built to accommodate these detectors. If only one detector is used, since a slight rotation of the detector causes a considerable shift of the viewing region of the detector on the synovium, it may not be necessary to move the detector shield during the consecutive measurements. In addition, it is still possible to give a quick boron dose response because the boron photon count rate is quite high. In the previous chapter, the boron photon count rate was estimated to be around 250 counts/s for the synovium phantom with a cylindrical shell structure at a beam current of 100 μA beam current and a

synovial boron concentration of 10,000 ppm. If the beam current in BNCS clinical trials is 1 mA, the boron photon count rate reaches 2500 counts/s. Therefore, the required collection time for each measurement could be as short as several seconds.

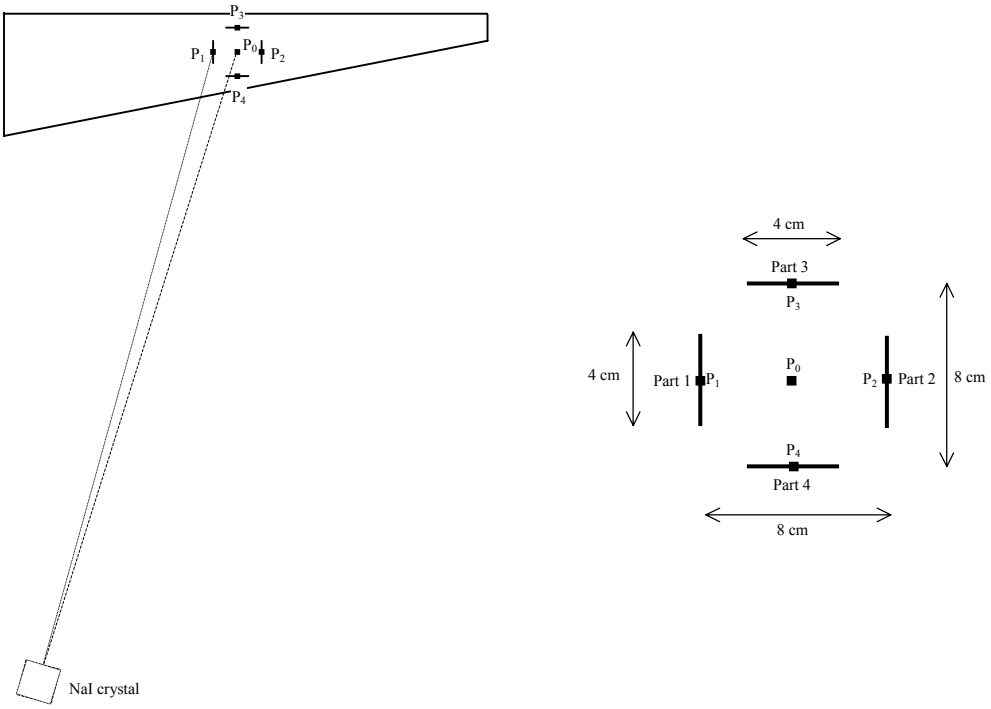

(a) (b)

Figure 8.4 (a) Schematic illustration of the configuration used for obtaining multiple measurements of *B*. The synovium is composed of 4 segments, with centers at P_1, P_2, P_3, and P_4. The collimator, detector shield, and the BNCS beam configuration were all included in the simulation model, but not shown here. The location of the detector and the detector shield are fixed, and the detector can be rotated to change its viewing field toward the synovium. Two positions of the detector are shown, with the detector viewing P_0, and P_1, respectively. However, since the rotation angle of the detector between the two positions is only 0.8°, the difference in the two positions is not discernable. (b) An enlargement of the synovium model showing dimensions.

Another example illustrating the multiple measurement approach was performed via Monte Carlo simulations. The synovium is separated four segments, as illustrated in Figure 8.4. The dimensions of each segment are 4 cm in length, 4 cm in width, and 1 mm in thickness. The boron concentration is 10,000 ppm throughout the synovium. The goal is to determine the vector N, the number of boron photons emitted from each segment of the synovium. In simulations, the location of the detector was fixed, and only its direction was changed. Five measurements were made, each with the symmetrical axis of the detector passing through one of the five points P_0, P_1, P_2, P_3, and P_4, respectively. Because of the

large distance from the detector to the synovium (260 cm), a very slight rotation of the detector is sufficient to change the direction of the detector. For example, the rotation angle is less than 1° in moving from the direction with the detector normal pointing to P_0 to the direction with the detector normal pointing to any point P_1, P_2, P_3, or P_4. During detector rotation, the collimator was rotated correspondingly, but the detector shield remained at its original location.

The simulated detection probability matrix, $P_{i\times j}$, is

$$P = \begin{bmatrix} 0 & 0 & 2.81\times10^{-6} & 6.06\times10^{-6} \\ 5.83\times10^{-6} & 0 & 0.87\times10^{-6} & 0 \\ 0 & 6.78\times10^{-6} & 0 & 2.43\times10^{-6} \\ 0 & 0 & 3.49\times10^{-6} & 4.10\times10^{-6} \\ 0 & 0 & 1.74\times10^{-6} & 8.47\times10^{-6} \end{bmatrix},$$

where P_{ij} is the detection probability for a photon emitted in part *j* of the synovium when the detector is at position *i*.

The vector, B, containing the detected boron photon count rates in the five measurements at 100 μA beam current, is

$$B = \begin{bmatrix} 122.0 \\ 98.8 \\ 85.0 \\ 142.6 \\ 87.9 \end{bmatrix},$$

in units of counts/s. Thus, the vector N can be obtained by solving P·N = B, and the result is

$$N = \begin{bmatrix} 1.13\times10^{7} \\ 1.16\times10^{7} \\ 3.78\times10^{7} \\ 2.61\times10^{6} \end{bmatrix},$$

in units of /s. Although the four segments of the synovium have the same spatial dimensions and the same boron concentration, the number of boron photons emitted from them is significantly different. This difference illustrates the non-uniformity of neutron flux in the knee joint. This example demonstrates the possibility of boron dose determination with multiple measurements. During this process, the positions of the detector shield and the detector can be both fixed (since the rotation angle of the detector is expected to be so small, this rotation is not necessary), and only the aperture in the collimator needs to be relocated so that the detector can see different synovium segments in different measurements.

8.4 Additional issues

8.4.1 Boron photons from fast neutrons captured by boron

Fast neutrons can also be captured by ^{10}B nuclei in the synovium, although compared to thermal neutrons, the absorption cross section of ^{10}B to fast neutrons is very small. The total kinetic energy deposited through a fast neutron capture is the energy released in the $^{10}B(n, \alpha)$ reaction (2.339 MeV on average) plus the kinetic energy of the incident neutron. In the reconstruction approaches described above, boron photons emitted from fast neutron captures are also counted in simulations and in experiments; however, in calculating the total energy deposited, the kinetic energy conveyed by fast neutrons is omitted.

It is indicated through Monte Carlo simulations that in the synovium 98% of the $^{10}B(n, \alpha)$ reactions occur through thermal neutron captures (< 1 eV), and the contribution from neutrons with energy above 100 eV is negligible. Therefore, the error in boron dose introduced by disregarding the kinetic energy of fast neutrons can be ignored.

8.4.2 Influence from boron deposited in normal tissue

In the reconstruction approaches described above, only the boron compound deposited in the synovium was considered. However, the boron compound injected into the synovial fluid can also accumulate in normal tissues, and the boron-containing normal tissues can also contribute 478 keV photons to the NaI detector. The appropriate boron compound in BNCS is still under investigation, and therefore the ultimate situation of boron compound aggregation in other tissues in addition to the synovium is still unclear.

The photon detector itself cannot discern the origins of the detected boron photons. If a clinically useful compound shows significant uptake in healthy tissue in the joint, that tissue can be voxelized in addition to the synovium. The way to handle these normal tissue voxels is the same as that for the synovium voxels: these voxels are also included in the reconstruction process. The P_i factors for these voxels are calculated or estimated with the Monte Carlo method, and the knowledge of the boron distribution in normal tissues would also be necessary.

8.5 Error analysis

Another issue involved in boron dose determination is the error associated with the reconstructed boron dose. The error arises in the detection step when the boron photons from the synovium are collected by the NaI detector, and also in the reconstruction step when the boron dose in the synovium is finally obtained from the number of detected boron photons using the reconstruction algorithm. The statistical error of the detected boron count B could be controlled to a low level (for example, less than 1%) since the count rate of boron photons can be very high (several thousands/second at a 10,000 ppm synovial

boron concentration and 1 mA beam current). The primary error associated with the estimate of the boron dose is more likely from the reconstruction step.

For the one measurement approach, the dominant error could be attributed to the accuracy of the knowledge of boron compound distribution in the knee joint. There are other potential error sources for the one measurement approach. For instance, during BNCS clinical treatment, the boron concentration could change with time. Accordingly, the thermal neutron flux changes as well. As a consequence, the photon production factors ($[B]_i \Phi_i / \sum_{i=1}^{M} [B]_i \Phi_i$) have to be updated as neutron irradiation progresses. The migration and uptake of a boron compound is a biochemical and physiological process, is compound specific, and is independent of neutron irradiation. It could be very difficult to obtain information regarding the dynamic variation of the boron distribution in the synovium and surrounding tissues. The reliability of the reconstructed boron dose could be significantly affected by the uncertainly of the photon production factors.

On the other hand, for the multiple measurement approach, no advance knowledge of boron compound distribution is necessary, and the error in the determined boron dose will primarily come from the error in the detection probability matrix P. If the knowledge of the location and the shape of the synovium in the knee joint is not accurate, the obtained matrix elements P_{ij} will also not be accurate.

Analysis of the uncertainty associated with the estimated boron dose due to error in matrix P was performed for the case illustrated in Figure 8.4. Specifically, the influence from the inaccuracy of the location of the synovium was examined. Synovium segments could be moved 2.5 cm left or right (segments 1 and 2) or 2.5 cm up and down (segments 3 and 4) from their original location described in Figure 8.4. The deviation of a synovium segment off its original position will cause the change of the values of its corresponding elements in the matrix P. For example, when part 1 is moved 2.5 mm left, the first column of the matrix P should be changed from $[0 \;\; 5.83\times10^{-6} \;\; 0 \;\; 0 \;\; 0]^T$ to $[0 \;\; 5.79\times10^{-6} \;\; 0 \; 0 \; 0]^T$, and when part 3 is moved 2.5 mm up, the third column of the matrix P should be changed from $[2.81\times10^{-6} \;\; 0.87\times10^{-6} \;\; 0 \;\; 3.49\times10^{-6} \;\; 1.74\times10^{-6}]^T$ to $[2.65\times10^{-6} \;\; 0.91\times10^{-6} \;\; 0 \;\; 3.39\times10^{-6} \;\; 1.60\times10^{-6}]^T$. If the space deviation of the synovium segments is not considered when determining the number of boron photons emitted from them, i.e., if the original matrix P generated for synovium segments at their original locations is used in solving the linear equations $P \cdot N = B$ to obtain N, errors in N will be introduced. For example, when segment 3 is moved 2.5 mm up, the actual B and N vectors are $B = [121.6 \;\; 102.0 \;\; 85.0 \;\; 146.0 \;\; 85.9]^T$ and $N = [1.13\times10^7 \;\; 1.16\times10^7 \;\; 3.99\times10^7 \;\; 2.61\times10^6]^T$. The obtained N vector from solving $P \cdot N = B$ using the old matrix P is $N' = [1.16\times10^7 \;\; 1.18\times10^7 \;\; 3.93\times10^7 \;\; 2.03\times10^6]^T$, in which the estimates for the segments 1, 2, and 3 are quite close to the actual values, however for segment 4 the estimate is

22% lower than the actual value. This example indicates that an appreciable location deviation of the synovium could cause a significant error in the reconstructed results.

8.6 Conclusions

Two issues arise from the spatial extension of the synovium. First, the production rate of boron photons ($\propto[B]\cdot\Phi$) at different locations in the synovium may be quite different. Since the neutron flux suppression in the synovium is significant, even if the boron concentration in the synovium is uniform, the boron photon production is still non-uniform. Second, since the size of the synovium is comparable to the mean free path of boron photons, the attenuation of these photons in the joint is related to the location where there are created.

In summary, the reconstruction of the boron dose in the synovium is complicated. The number of boron photons emitted from the synovium, the photon attenuation in the joint, and the structure of the telescope system all affect the 478 keV photon count rate in the NaI detector. At Petten, during boron concentration reconstruction, the boron concentration is assumed to be uniform in the target tissue, and the thermal neutron flux is assumed to be the same under various boron concentrations. This simplified picture is not valid for BNCS.

Chapter 9 Conclusions and future work

9.1 Conclusions

This thesis verified the feasibility of a gamma ray telescope system for online synovial boron dose determination in BNCS via both simulations and experiments.

The number of $^{10}B(n,\alpha)$ reactions in the synovium increases non-linearly with increase in synovial boron concentration. The saturation of boron photon production at high synovial boron concentrations demonstrates the significant suppression of thermal neutron flux in the synovium.

Prior to collimation and detector shielding, the signal from boron photons originating from the synovium was completely buried in the background photon count. The background count rate has been reduced by several orders of magnitude with the aid of appropriately designed collimator and detector shields. The remaining background particles primarily enter the detector from its front side. Because of the aperture in front of the detector, the background contribution from neutrons and photons can be not completely eliminated.

Even after shielding, the use of HPGe detectors is still not appropriate since the neutron flux at the detector location is still high. The usability of NaI detectors was confirmed. Simulation results indicated that the count rate of 478 keV boron photons from the synovium is much higher than that of 511 keV annihilation photons, and also the count rate of 511 keV photons is basically not affected by variations in synovial boron concentration. The 511 keV photon count can be simply subtracted from the total photon count under the boron peak.

A background peak appears at the energy region of 478 keV photons in the measured photon spectrum by a 10.2 cm × 10.2 cm NaI detector. Neutrons are mainly responsible for the formation of this peak. The contribution from 511 keV photons is still significant, but these photons are mainly created inside the NaI crystal.

In spite of the appearance of a background peak at the location of the boron peak, the contribution of boron photons from the synovium is easily extractable and quantifiable above background from the detected photon spectrum. Consistent with the predictions of Monte Carlo simulations, the count rate of boron photons from the synovium is saturated at high boron concentrations. The number of boron photons emitted from the synovium as well as the number of boron photons ultimately detected is strongly dependent on the spatial distribution of the boron compound. From the experience learned from comparison of various configurations of the synovium phantom, for the same amount of boron compound, the larger the area over which the compound is distributed, the larger the number of boron neutron capture events. For actual clinical treatments, the boron photon count rate is expected to be sufficient for prompt and reliable determination of the synovial boron dose.

Since boron photon production ($\propto[B]\cdot\Phi$) is not uniform in the synovium, it is not suitable to consider the synovium as an entire unit when determining the synovial boron dose. Instead, the division of the synovium into voxels or segments is necessary. In addition to the measured count rate of boron photons from the synovium, additional information has to be provided for calculation of *photon detection factors* and/or *photon production factors* for each voxel or segment.

9.2 Recommendations for future work

There are some aspects that can be explored to improve the performance of the system in the future.

In previous experiments, a 10.2 cm × 10.2 cm NaI crystal was used. Optimization of the size of NaI crystal could be valuable. The response of NaI crystal to incident particles is strongly dependent on the size of the crystal. 478 keV photons and neutrons have different mean free paths in NaI crystal, and a maximum signal to noise could be achieved with an optimized size of the crystal.

For the collimator, only the thicknesses of shielding materials were carefully selected, and optimization of the height and the width of the collimator was not performed. The thickness and the height of the collimator are more than sufficient in the current system. A more compact collimator will be more convenient, especially if rotation of the collimator is necessary.

Simplified synovium phantoms were used in the development of the telescope system so far. More realistic phantoms of the synovium can be constructed to further demonstrate the feasibility of the telescope.

At MIT LABA, BNCS is still under investigation, and future work on the telescope system will also be affected by the ultimate choice of boron compound as well as by the physical configuration of the therapy room.

References

1. E.D. Harris, Jr., "Rheumatoid arthritis. The clinical spectrum," edited by W.N. Kelley, E.D.Harris, S.Ruddy, and C.B.Sledge, in *Textbook of Rheumatology* (Saunders, Philadelphia, 1981).

2. P.E.Lipsky, "Rheumatoid arthritis," in *Harrison's Principles of Internal Medicine*, edited by J.D.Wilson et al.12th ed. (McGraw-Hill, New York, 1991), pp. 1437-1443.

3. M.Davis and M.Chinol, "Radiopharmaceuticals for radiation synovectomy: evaluation of two yttrium-90 particulate agents," J. Nucl. Med., **30**: 1047-1055 (1989).

4. J.C.Yanch, S.Shortkroff, R.E.Shefer, S.Johnson, E.Binello, D.Gierga, A.G.Jones, G.Young, C.Vivieros,A.Davison and C.Sledge, "Boron neutron capture synovectomy: Treatment of rheumatoid arthritis based on the $^{10}B(n,\alpha)^{7}Li$ nuclear reaction," Med. Phys., **26**: 364-375 (1999).

5. E.Binello, "Efficacy of Boron neutron capture synovectomy in an anminal model," Ph.D. thesis, Massachusetts Institute of Technology, 1999.

6. D.P.Gierga, " Neutron delivery for boron neutron capture synovectomy," Ph.D. thesis, Department of Nuclear Engineering, Massachusetts Institute of Technology, Cambridge, MA, 2001.

7. R.E.Shefer, R.E.Klinkowstein, J.C.Yanch, and W.B.Howard, "Tandem electrostatic accelerator for BNCT," Proceedings of the First International Workshop on Accelerator-Based Neutron Sources for Boron Neutron Capture Therapy, 1994.

8. D.P.Gierga, J.C.Yanch, and R.E.Shefer, "Development and construction of a neutron beam line for accelerator-based boron neutron capture synovectomy," Med. Phys., **27**: 203-214 (2000).

9. G.L.Locher, "Biological effects and therapeutic possibilities of neutrons," Am. J. Roent., **36**: 1-13 (1936).

10. J.A.Coderre, " The radiation biology of boron neutron capture therapy," Rad. Res., **151**: 1-18 (1999).

11. W.F.A.R. Verbakel, "Validation of the scanning γ-ray telescope for in vivo dosimetry and boron measurement during BNCT," Phys. Med. Biol., **46**: 3269-3285 (2001).

12. W.F.A.R. Verbakel and F.Stecher-Rasmussen, "A γ-ray telescope for on-line measurements of low boron concentrations in a head phantom for BNCT," Nucl. Instr. and Meth. in Phys. Res. A, **394**: 163-172 (1997).

13. W.F.A.R. Verbakel and F.Stecher-Rasmussen, "On-line reconstruction of low boron concentrations by in vivo γ-ray spectroscopy for BNCT," Phys. Med. Biol., **46**: 687-701 (2001).

14. G.F.Knooll, *Radiation Detection and Measurement* (John Wiley & Sons, New York, 1999).

15. I.Lux and L.Koblinger, *Monte Carlo Particle Transport Methods: Neutrons and Photon Calculations* (CRC Press, Boca Raton, 1991).

16. L.L.Carter and E.D.Cashwell, *Particle-Transport Simulation with the Monte Carlo Method*, Published by Technical Information Center, Office of Public Affairs, U.S. Energy Research and Development Administration, 1975.

17. Website of ORTEC: http://www.ortec-online.com.

18. J.F.Briesmeister, "MCNP-A general Monte Carlo N-particle transport code, Version 4B," Los Alamos National Laboratory Report, LA-12625-M (1997).

19. J. Guzek, Ph.D. thesis, University of Witwatersrand, South Africa, 1998.

20. M.Lambeth, "Development of a computerized anthropomorphic phantom for determination of organ doses for diagnostic radiology," B.S. Thesis, Massachusetts Institute of Technology.

21. Website of Lawrence Berkeley National Laboratory: http://ie.lbl.gov .

22. O.Hausser, M.A.Lone, T.K.Alexander, S.A. Kushneriuk, and J.Gascon, "The prompt response of bismuth germinate and NaI(Tl) scintillation detectors to fast neutrons," Nucl. Instr. And Meth., **213**:301-309 (1983).

23. T.Inada, "Detection of fast neutrons with NaI(Tl) crystal," J. Nucl. Sci. Technol., **5**:287-291(1968).

24. J.J. Van Ruyven, Z. Sujkowski, W.H.A. Hesselink, and H.Verheul, "The response of large NaI(Tl) detectors to fast neutrons," Nucl. Instr. And Meth., **216**:141-148 (1983).

25. L. Miramonti, "Study of the nuclear recoil response of a NaI(Tl) scintillator detector with a ^{252}Cf neutron source," Radiation Physics and Chemistry, **64**:337-342(2002).

26. J.I. Rhode, "Neutron irradiation of a NaI(Tl) crystal," Am. J. Phys., **55**:653-657(1987).

27. L.C.Thompson, " Neutron effects in a 2″×2″ NaI(Tl) scintillation spectrometer," Nucl. Instr. And Meth., **25**:331-337 (1964).

28.F.E.Cecil, K.Killian, and M.Rymes, "Evaluation of NaI(Tl) scintillator as a fast neutron monitor," IEEE Transaction on Nuclear Science, **NS-26**:1487-1489 (1979).

29 S.J.Du Toit and L.M.Bollinger, "Lifetimes of energy levels in Al^{28}, Mn^{56}, Cu^{64}, Rh^{104}, and I^{128} excited by slow neutron capture," Physical Review, **123**: 629-636 (1961).

30 R.P.Gardner, E.Sayyed, Y.Zheng, S.Hayden, and C.W.Mayo, "NaI detector neutron activation spectra for PGNAA applications," Applied radiation and isotopes, 53: 483-497 (2000).

31. Website of Nuclear Data Evaluation Laboratory, Korea: http://atom.kaeri.re.kr .

32. E.Gaillard, Ph.D. thesis, University d'Orsay,1994.

33. Website of Brookhaven National Laboratory: http://www2.bnl.gov/ton/ .

34. Website of Alcan Packaging: http://www.alcanpackaging.com/ .